NON-PERTURBATIVE STUDIES OF STRONGLY INTERACTING MATTER AT FINITE TEMPERATURE AND DENSITY

A thesis submitted to
Tata Institute of Fundamental Research, Mumbai, India
for the degree of
Doctor of Philosophy
in
Physics

By
Debasish Banerjee
Department of Theoretical Physics
Tata Institute of Fundamental Research
Mumbai - 400 005, India

July 2011

Declaration

This thesis is a presentation of my original research work. Wherever contributions of others are involved, every effort is made to indicate this clearly, with due reference to the literature, and acknowledgement of collaborative research and discussions.

The work was done under the guidance of Professor Rajiv V. Gavai, at the Tata Institute of Fundamental Research, Mumbai.

(Debasish Banerjee)

In my capacity as the supervisor of the candidate's thesis, I certify that the above statements are true to the best of my knowledge.

(Rajiv V. Gavai)

Acknowledgments

First and foremost, I would like to thank my advisor Rajiv V. Gavai for all his guidance and support. Without the additional guidance of Saumen Datta, this thesis would not have been complete. My gratitude to Sourendu Gupta and Nilmani Mathur for teaching me and guiding me in many respects. It is also a pleasure to acknowledge Rajeev Bhalerao, Mustansir Barma, Shailesh Chandrasekharan, Kedar Damle, Avinash Dhar, Amol Dighe, Gautam Mandal, Pushan Majumdar and Shiraz Minwalla for the physics I have learnt from them. Special thanks to Arnab Sen for all the physics and non-physics discussions I have had with him over the years. For making the time spent in the office really fun and for numerous physics discussions, I am grateful to all my DTP colleagues, many of whom are elsewhere at present. Thanks are also due to the DTP office staff: Ajay Salve, Girish Ogale, Mohan Shinde, Rajan Pawar and Raju Bathija and the computer systems administrators: Ajay Salve and Kapil Ghadiali for being extremely helpful at all times. Thanks are also due to the ILGTI (Indian Lattice Gauge Theory Initiative) for making available the computing resources of CRAY and two clusters - HIVE and BROOD, on which most of the computations reported in the thesis were done. I am also greateful to Nikhil Karthik, M. Padmanath and Sayantan Sharma for the discussions I have had with them regarding some of the works in this thesis. A lot of quality time was spent with Swastik Bhattacharya, Urmila and Subha Majumdar, Shamayita Ray, Kabir Ramola, and Shamasish Sengupta and I am grateful to all of them. Finally, I would like to thank my parents for always being extremely supportive at all times.

Collaborators

This thesis is based on the work done in collaboration with Shailesh Chandrasekharan, Saumen Datta, Rajiv Gavai, Sourendu Gupta, Sayantan Sharma and Pushan Majumdar. In particular, Chapter 2 was done in collaboration with Rajiv V. Gavai and Sourendu Gupta (2011), Chapter 3 with Saumen Datta, Pushan Majumdar and Rajiv Gavai (2011), Chapter 4 with Sayantan Sharma and Rajiv Gavai (2008) and Chapter 5 with Shailesh Chandrasekharan (2010).

To My Parents

Contents

Synopsis

Introduction

Quantum Chromodynamics (QCD) is widely believed to be the underlying physical theory of strong interactions with quarks and gluons as its elementary degrees of freedom. The theory is asymptotically free [1]. The strength of interaction between the quarks and gluons decreases with increasing momentum transfer. However, a single isolated quark or gluon has never been observed despite numerous experimental efforts [2]. Experimentally observed hadrons are bound states of quarks and gluons. Unlike the case of the hydrogen atom, where the binding energy is only about 10^{-8} times the mass of the bound state, most of the mass of any hadron arises from the strong interactions between quarks and gluons. The binding energy accounts for nearly 99% of the proton's total mass. Perturbation theory therefore seems inapplicable, and non-perturbative methods are needed to study this theory. Lattice QCD is the only reliable non-perturbative formulation of QCD that allows a systematic and precise study at all energy scales. Lattice QCD has been successful in the ab-initio calculation of the masses of all the light hadrons. It is being increasingly used to make predictions [3] about decay constants, running coupling, heavier hadrons, excited states, resonances and flavour physics. It seems therefore a good idea to test QCD in new conditions such as extreme temperatures and density.

Quantum field theory (QFT) at finite temperature and density is studied using the grand-canonical partition function:

$$\mathcal{Z} = \mathrm{Tr} e^{-\beta(H-\mu N)} \tag{1}$$

where H is the Hamiltonian of the theory, β is the inverse temperature and μ is the chemical potential conjugate to some conserved charge N. Since the lattice formulation of a QFT is made on a discrete space-time lattice with spacing a [4], the spatial volume of the lattice is $V = (N_s a)^3$ and the temperature is $T = 1/N_t a = 1/\beta$, where

N_s and N_t are the number of sites in the spatial and temporal directions respectively. Quark fields are defined on the sites, while the gauge fields are defined as SU(3) matrix valued fields on the links joining the sites.

Describing the fermions on the lattice is complicated by the fermion doubling problem, because of which one gets 16 flavours of fermions in the continuum for a single Dirac field on the lattice. This is a direct consequence of the no-go theorem by Nielsen-Ninomiya [5]. There are different ways of get rid of the problem, each with its own advantages and disadvantages. Staggered fermions are extensively used to study the chiral transition in QCD. This formulation of fermions preserves an exact U(1) $\times$ U(1) chiral symmetry of the full theory, and an order parameter can be defined to characterize the chiral transition.

The lattice thermodynamics of QCD predict that quarks and gluons get deconfined to form Quark-Gluon plasma (QGP) at high temperatures [6]. QGP may have existed in the early universe few μ-seconds after the Big Bang, which eventually made the transition into the hadronic phase as the temperature went down. There is a global effort to re-create similar extreme conditions using heavy ion collisions in laboratories around the world [7] to understand the physics of this transition. It is therefore important to study the properties of this matter theoretically in as much detail as possible in order to assist the experimental studies.

In this thesis, we will present our work on the following problems to gain some insight into the nature and properties of the medium created in heavy-ion collision experiments. In order to investigate the chiral symmetry properties of the medium, we have used the spatial correlation functions of mesons in different quantum number channels. We find that at temperatures above 1.33 T_c (where T_c is the cross-over temperature) chiral symmetry gets restored [8]. In the second problem, we have computed the thermalization time of heavy quarks in a gluon plasma. This quantity has been inferred for the charm quark from these experiments. Experimentally, it seems that both the light and the heavy quarks thermalize at the same rate whereas the weak coupling methods show the thermalization rate of a heavy quark is suppressed relative that of a light quark by the heavy quark mass. Therefore, it is important to check if a non-perturbative evaluation yields results comparable with experiments. Our results are closer to the estimates supported by experiments than those of the weak coupling methods [9]. In the third and fourth chapters, we will focus on QCD matter at finite density.

Strongly interacting matter at finite densities may be produced in the low energy runs in RHIC and in the experiments at the proposed FAIR (Facilities for Anti-proton and Ion Research). QCD with 2+1 flavours, at low temperatures and high

densities is expected to have different phases, such as the colour superconducting phase. Increasing the temperature at large densities, it is again expected to go the QGP phase. Studies using simpler models at low temperatures suggest that these phases are separated from the hadronic phase by a first order phase transition [10]. Thus, there exists a line of first order transitions, beginning from the $T = 0$ axis which ends in a second order critical point in the (T, μ) plane [11], and continues to the $\mu = 0$ axis as a crossover. The experiments will aim at a precise determination of the critical point and will also study signals of other possible phases at larger densities. The existence of the critical point has been the subject of recent lattice investigations [12]. These studies mostly use the staggered fermion formulation. However, the spin and the flavour degrees of freedom get mixed in this formulation at finite lattice spacings. This is a disadvantage, since the location and the existence of the critical point depends on the number of fermion flavours. It is therefore desirable to use fermions which have unambiguous flavour identification on the lattice as well as exact chiral symmetry. The overlap fermion operator [13] satisfies these properties, although at the expense of being non-local making the corresponding calculations expensive. Due to this non-locality, the inclusion of chemical potential is non-trivial. A proposal for this was formulated in [14]. We will investigate the thermodynamics of the free fermion theory at finite chemical potential with this method and show that it has the correct continuum limit for the thermodynamic quantities . It was also seen that this formulation at finite μ does not respect chiral symmetry [15]. Simulations of QCD at finite density are also affected by the sign problem. This arises because, the determinant of the Dirac operator which is a part of the probability measure becomes complex at finite μ hindering the use of Monte-Carlo simulations. Reformulating the theory in terms of other degrees of freedom can remove the sign problem. In the last chapter, we study such a procedure for the non-linear O(2)-sigma model at finite μ. The phase diagram of this theory is then investigated using the worm algorithm [16].

Screening Correlators

Correlation functions are useful probes to study the nature of the medium. At zero temperatures they are routinely used to calculate the masses of particles in various quantum number channels. At finite temperatures, the Debye mass of the quantum electrodynamics (QED) plasma can be obtained from the spatial correlation functions of the electric field. We can also study the symmetries broken or restored in a medium by studying the spatial correlation functions of different particles in the same quantum number channel(s). To understand the chiral symmetry restoration patterns in 2-

flavour QCD, screening correlators of all the eight possible local mesons were studied. At $T = 0$, they correspond to the Goldstone-pion (PS), the scalar (S; or the a_0 meson) and three components each of the vector (V) and the axial-vector (AV) mesons. At finite temperature, the symmetries of the slice (x, y, t) orthogonal to the direction of propagation is no longer cubic and the group theoretic classification of the mesons are different. It turns out [17] that the PS/S , $V_x + V_y(Vs)$, $AV_x + AV_y(AVs)$, V_t, AV_t all lie in the same representation but do not mix under the symmetries of the (x, y, t) slice. Hence, correlators in each of these quantum number channels need to be studied separately. $V_x - V_y$ and $AV_x - AV_y$ lie in another representation; but were found to be identically zero for all-z in previous studies [18] as well as in our study.

We have investigated these correlation functions as a function of temperature from 0.89-1.92 T_c, spanning both the hadronic and the QGP phase, on a lattice with a cut-off $a = 1/(6T)$. In the theory with finite quark mass, T_c is the cross-over temperature. If the chiral symmetry is restored, a degeneracy is expected in the correlation functions in a given quantum number channel.

Screening masses are extracted from the long distance behaviour of the correlation functions. For the staggered fermions, there is a contribution to the correlation function from a parity partner of the lightest natural parity meson in a given quantum number channel. The correlation functions are parameterized as:

$$C(z) = A_1(\ \mathrm{e}^{-\mu_1 z} + \mathrm{e}^{-\mu_1 (N_z - z)}\ ) + (-1)^z A_2(\ \mathrm{e}^{-\mu_2 z} + \mathrm{e}^{-\mu_2 (N_z - z)}\ ) \qquad (2)$$

where μ_1 and μ_2 are the screening masses of the lightest natural parity meson appropriate to the operator used and its opposite parity partner. These screening masses are determined by minimizing the correlated-χ^2.

In fig 1 we plot the lowest screening mass in each channel as a function of T/T_c. Above T_c, we plotted only the S/PS and Vt/AVt channels. The lowest Vs/AVs masses are slightly larger, but consistent with Vt/AVt at the 2-σ level. μ_{PS}/T increases monotonically with T whereas μ_S/T dips near T_c. Note also that μ_{Vt}/T may approach its ideal gas value from above, becoming consistent with the limit already at around T_c. However μ_S/T remains about 20% below this limit even at the highest temperature we explored. The PS and S screening masses become identical only after 1.33 T_c. We expect this late restoration of chiral symmetry in the PS/S channels is due to the finiteness of the pion mass. Even though at high temperatures $\mu \propto T$; above T_c, they could in general be a function of m_π/T. Qualitatively, chiral symmetry gets restored at temperatures where this function goes to unity. Similar patterns are also observed in the correlation function directly. The PS/S correlation functions exhibit

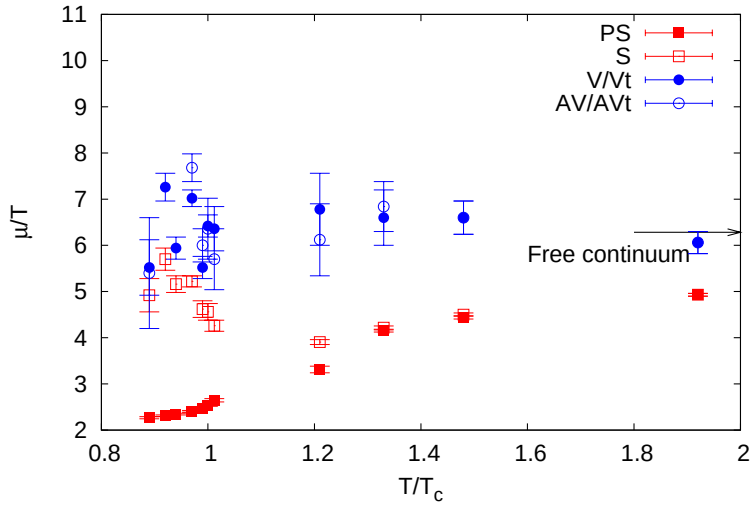

Figure 1: Screening masses of various mesons as a function of T/T_c

degeneracy after 1.33 T_c. Between T_c and 1.33 T_c, in the V_s and V_t channels, there is a degeneracy in the long distance part of the correlation functions, but they differ at short distances. The long distance part shows degeneracy only above 1.33 T_c.

To test the robustness of the observations, the continuum limit was investigated using these results, and those obtained from an earlier computation at a lattice spacing $a = 1/(4T)$ [18]. At 1.5 and 2 T_c, we checked whether the values of the screening masses are consistent with a $1/N_t^2$ correction from the free field limit. This was true for the V/AV channel, but not in the PS/S channel. It is possible that the weak-coupling results emerge at even smaller lattice spacings.

Diffusion Coefficient of the Gluon plasma

The transport coefficients of the medium created by heavy-ion collisions are inferred from the measurements of the produced particle spectra and the symmetry of their flow. It appears that the heavy charm quarks thermalize as fast as the light quarks [19]. This is quite in contrast to that expected from weak coupling methods, which estimate the thermalization rate of heavy quarks to be suppressed by a factor of $\sim T/M$ with respect to that of the light quarks, where T is the temperature of the medium and M is the mass of the heavy quark [20]. A non-perturbative lattice computation could be important for a comparison with experiments.

It was realized by [21, 22] that non-relativistic QCD can be used to describe the quark whose mass is much greater than the temperature of the medium. The motion of the heavy quark in the quark-gluon plasma can be treated as in Brownian motion;

and its momentum evolves according to the Langevin equation:

$$\frac{dp}{dt} = \xi(t) - \eta_D p; \qquad \langle \xi(t)\xi(t') \rangle = \kappa\delta(t-t') \tag{3}$$

where $\xi(t)$ is the random (in time) force acting on the heavy quark; η_D is the momentum drag coefficient that slows down the motion of the heavy quark; and hence a property of the medium. κ is the strength of the stochastic interaction and also depends on the medium. The solution of this equation determines the motion of the heavy quark, and hence give us valuable information about the nature of the medium.

In terms of the quark fields, the heavy quark current is given by $J^\mu = \bar{\psi}\gamma^\mu\psi$; and the following expression needs to be evaluated:

$$\kappa^{(M)} \equiv \lim_{\omega\to 0} \frac{M^2\omega^2}{3T\chi} \sum_i \frac{2T\rho^{ii}(\omega)}{\omega}; \qquad \rho^{\mu\nu}(\omega) = \int_{-\infty}^{\infty} dt \mathrm{e}^{\imath\omega t} \int d^3x \left\langle \frac{1}{2}[J^\mu(x), J^\nu(0)] \right\rangle \tag{4}$$

This is the direct analogue of κ introduced in eqn 3 and χ is the number density of heavy quarks.

On expanding in powers of $1/M$, the leading term in this expansion is independent of M. Further simplification is achieved in the static heavy quark limit, where the fermion propagators can be replaced by Wilson lines in the temporal direction. A temporal Wilson line, $U(\vec{x}, \tau_i, \tau_f)$, is the product of the gauge links along the temporal direction from τ_i to τ_f: $U(\vec{x}, \tau_i, \tau_f) = \prod_{\tau=\tau_i}^{\tau=\tau_f} U_\tau(\vec{x}, \tau)$. When the Wilson line goes around the entire τ- direction, it's trace is called the Polyakov loop. In terms of the Wilson lines and Polyakov loops, the following gauge-invariant temporal correlation function of the chromo-electric field (E^i) needs to be evaluated:

$$G_E(\tau) = -\frac{1}{3}\sum_{i=1}^{3} \frac{\left\langle \mathrm{Re\ Tr}\left[U(\beta,\tau) g E^i(\tau,\vec{0}) U(\tau,0) g E^i(0,\vec{0})\right]\right\rangle}{\langle \mathrm{Re\ Tr}[U(\beta,0)]\rangle} \tag{5}$$

The explicit dependence on $\vec{x}$ is suppressed since we average over all $\vec{x}$. From this correlation function, the diffusion coefficient κ is obtained by calculating the corresponding spectral function $\rho(\omega)$ and examining its low-ω behaviour:

$$G_E(\tau) = \int_0^\infty \frac{d\omega}{\pi}\rho(\omega)\frac{\cosh(\frac{\beta}{2}-\tau)\omega}{\sinh\frac{\beta\omega}{2}}; \qquad \kappa = \lim_{\omega\to 0}\frac{2T}{\omega}\rho(\omega) \tag{6}$$

Employing the value of the heavy quark mass, the drag coefficient $\eta_D = \kappa/2MT$, can

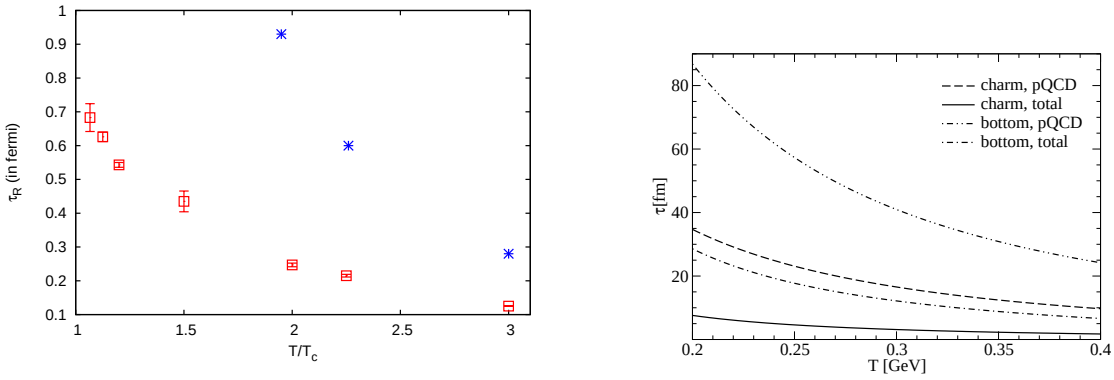

Figure 2: (Left) The relaxation time of the charm quark calculated in pure gauge theory. Upon changing the perturbative renormalization scale by a factor of two, the estimated value changes by about 15 %. The stars are indicative of the thermalization times (τ_0) at different initial temperatures (T_0) estimated for the light partons to explain the flow of light hardons seen in experiments [24]. However, values of thermalization time varying from 0.3 - 0.8 fm are used in the literature. (Right) An perturbative estimate for the thermalization time of the charm and bottom quarks [26]

.

be calculated from the dimensionless diffusion coefficient κ/T^3. The thermalization time is inverse of the drag coefficient.

The dimensionless correlation functions $G_E(\tau)/T^4$ at the same gauge coupling g^2 as a function of τT fall on the same curve. This behaviour suggests the absence of any non-trivial change in the diffusion coefficient in the temperature regime from 1.5 T_c to 3 T_c. This statement is independent of any renormalization scheme chosen to relate the actual value of diffusion coefficient with the experimentally observed value, since it is known [23] that the relevant renormalization constants for this correlation function depend only on the gauge coupling; and hence common to all these correlators. This implies that η_D has a behaviour proportional to the square of the temperature; and hence the thermalization time should fall as the inverse square of temperature from the RHIC measurement to the value measured at ALICE. Significant finite volume effects are absent in these correlation functions.

In order to convert the lattice estimate into a physical value, we have renormalized the Wilson lines in the correlation functions non-perturbatively [25], while a perturbative estimate was used for the chromo-electric fields [23]. In converting our estimates of κ/T^3 to τ_R for the charm quark, we have employed the following scales: T_c= 170 MeV and M = 1.3 GeV. This estimate of the physical scale assumes that

the effect of inclusion of light fermions can be absorbed in a redefinition of T_c. Our results shown in left panel of fig 2 indicate much smaller relaxation time than the perturbative results shown in the right panel of fig 2, roughly by an order of magnitude. These results imply that heavy quarks can thermalize rapidly while interacting with a thermalized medium of quarks and gluons. This could explain the similar magnitude of flows seen for the heavy and the light hadrons in the experiments [24].

Overlap operator with chemical potential

The overlap operator is very useful for the lattice study of the QCD critical point since it allows an exact chiral symmetry as well as permits unique spin flavour identification of the lattice operators with the physical states in the continuum theory. In this chapter, we have studied the chiral properties of the overlap Dirac operator at finite densities. We have also investigated the approach to the continuum limit of the thermodynamic quantities both analytically and numerically for a system of ideal overlap quarks [15]. This work was done in collaboration with Sayantan Sharma, and we will only report the analytic investigations with finite chemical potential in this synopsis.

At zero chemical potential the overlap Dirac operator has the following form for massless fermions:

$$D_{ov} = 1 + \gamma_5 \mathrm{sgn}(\gamma_5 D_W) \tag{7}$$

where sgn denotes the matrix sign function and D_W is the standard Wilson-Dirac operator on the lattice but with a negative mass term $M \in (0, 2)$ and is given as:

$$\begin{aligned} D_W(x,y) &= (3 + \frac{a}{a_4} - M)\delta_{x,y} - \frac{a}{a_4}\left[U_4^\dagger(x-\hat{4})\delta_{x-\hat{4},y}\frac{1+\gamma_4}{2} + \frac{1-\gamma_4}{2}U_4(x)\delta_{x+\hat{4},y}\right] \\ &- \sum_{i=1}^{3}\left[U_i^\dagger(x-\hat{i})\delta_{x-\hat{i},y}\frac{1+\gamma_i}{2} + \frac{1-\gamma_i}{2}U_i(x)\delta_{x+\hat{i},y}\right] \end{aligned} \tag{8}$$

For a diagonalizable matrix, $A = U\Lambda U^{-1}$, where Λ is the corresponding diagonal matrix; the sign function is defined as [27] : sgn(A) = U sign(Re Λ) U^{-1}. If the matrix is non-diagonalizable, then one needs resort to block diagonalization. This non-locality of the operator is manifested through the implementation of the sign function.

The chemical potential is usually introduced as the Lagrange multiplier for the conserved number operator. For local fermion actions, such as the Wilson and staggered fermions, this method gives rise to unphysical μ^2 divergences in the continuum

limit at $T \to 0$. This does not happen when μ is introduced as the fourth component of a constant imaginary vector potential [28]. A further generalization involves the use of functions $K(\hat{\mu})$ and $L(\hat{\mu})$ in place of $\exp(\hat{\mu})$ and $\exp(-\hat{\mu})$ ($\hat{\mu} = \mu a_4$) where $K(\hat{\mu}) = 1 + \hat{\mu} + \mathcal{O}(\hat{\mu}^2)$ and $L(\hat{\mu}) = 1 - \hat{\mu} + \mathcal{O}(\hat{\mu}^2)$. The quadratic divergences are avoided if $K(\hat{\mu}) \cdot L(\hat{\mu}) = 1$ [29]. Note that $\gamma_5 D_W$ which was Hermitian at zero μ, now becomes non-Hermitian.

This procedure is non-trivial for the overlap operator due to its non-locality [30]. Instead, an inspired guess was used in [14] to formulate a form that has the correct continuum limit. It was suggested that $D_W(\mu = 0) \longrightarrow D_W(\mu)$ by multiplying factors $\exp(\mu a_4)$ and $\exp(-\mu a_4)$ to the links U_4 and $U_4^\dagger$ respectively in eq.(8). Since $\gamma_5 D_W(\mu)$ becomes non-Hermitian, and its eigenvalues complex, the usual definition of the sign function needs to be extended. The natural choice [14] is to use the sign function for the real part of the eigenvalues. This however, leaves the case of the imaginary eigenvalues undefined.

In this work we have carried out an analytic investigation of the problem. We introduce the chemical potential as in [29] in terms of functions $K(\hat{\mu})$ and $L(\hat{\mu})$. Since this is a free theory, we can diagonalize the operator exactly in the Fourier space and obtain analytical expression for the energy density, pressure and number density. The expressions involve a summation over the discrete momenta and the Matsubara frequencies. The summation over the latter are done using the contour integral technique.

Our analytic calculations require that $K(\hat{\mu}).L(\hat{\mu}) = 1$ be satisfied to avoid spurious μ^2/a^2 divergences in the continuum limit in the case of the overlap operator as well. Numerically, this result was already verified in [31]. This shows that the non-locality of the operator does not survive the continuum limit. Further, we need to satisfy the condition $K(\hat{\mu}) - L(\hat{\mu}) = 2\hat{\mu} + \mathcal{O}(\hat{\mu}^2)$ to obtain the correct continuum limit of the thermodynamic quantities.

On the lattice, at finite temperature and density, we get the following expression for the energy density:

$$\epsilon a^4 = \frac{2}{N^3} \sum_{p_j} \left[\frac{\sqrt{f}}{\sqrt{1+f}} \frac{1}{e^{(\sinh^{-1}\sqrt{f} - \hat{\mu})N_T} + 1} + \frac{\sqrt{f}}{\sqrt{1+f}} \frac{1}{e^{(\sinh^{-1}\sqrt{f} + \hat{\mu})N_T} + 1} + \epsilon_{3\mu} + \epsilon_{4\mu} \right] \tag{9}$$

where $f = \sum_{j=1}^{3} \sin^2(ap_j)$ and the last two terms are certain line integrals that vanish in the continuum limit. This is the standard expression for the lattice energy density

which reduces to the usual result in the continuum:

$$\epsilon = \frac{2}{(2\pi)^3}\int \frac{E\ \prod_{j=1}^{3} dp_j}{1+e^{\frac{E+\mu}{T}}} + \frac{2}{(2\pi)^3}\int \frac{E\ \prod_{j=1}^{3} dp_j}{1+e^{\frac{E-\mu}{T}}} \tag{10}$$

The equation of state $\epsilon = 3P$ holds in the presence of finite μ on discrete lattices.

Our numerical investigations were mostly aimed at determining the values of N_t and M at which the continuum limit is approximated. We found that this limit is achieved for $N_t \geq 12$ for all M; with the $1.5 < M < 1.6$ region displaying the smallest deviations. We have also found that the exact chiral symmetry properties of the overlap operator are lost at finite μ. These will be reported in detail in the thesis of Sayantan Sharma.

Chemical Potential and the sign problem

Lattice investigations at finite density are also hindered by the sign problem. At finite μ, the Dirac operators lose their Hermiticity properties. We have seen this explicitly for the Wilson-Dirac operator in the last chapter. This makes the fermion action complex, in general. Therefore, in a Monte-Carlo evaluation, it's interpretation as a probability measure fails. Numerically, while calculating the expectation value of any operator, large cancellations take place with a rapid loss of signal-to-noise ratio. Several methods have been experimented with [12] to get rid of this problem, with limited success.

A recent progress in this field has been the revival of an idea tried and tested (rather unsuccessfully) about two decades back. This consists of reformulating theories afflicted by the sign problem in terms of other field variables in certain parameter regimes. QCD with staggered fermions at finite μ in the strong coupling regime ($g^2 \to \infty$) is one such example [32]. In this case, the theory can be rewritten as a configuration of colour-singlet mesons and baryons. The relatively recent introduction of the "worm" algorithm [33] has brought about an renewed interest in the study of these reformulations. Indeed, if this is achieved for full QCD, it could be of use in the theoretical investigations of other phases at finite densities. It could also be employed to cross-check the current results for the critical point by doing simulations at finite μ. In this part, we will discuss the O(2) non-linear sigma model which has the same type of sign problem as QCD; and discuss how such a reformulation and the worm algorithm has helped in determining a large part of the phase diagram [16] at finite μ in 3-dimensions.

This theory, also known as the XY model in condensed-matter literature, consists

of U(1) spins of unit magnitude with ferromagnetic nearest neighbour interactions. The action of the model is:

$$S = -\frac{\beta}{2} \sum_{\vec{x},\alpha} \left(\exp^{\imath(\phi_{\vec{x}+\alpha} - \phi_{\vec{x}}) - \mu\delta_{\alpha,t}} + \exp^{-\imath(\phi_{\vec{x}+\alpha} - \phi_{\vec{x}}) + \mu\delta_{\alpha,t}} \right) \tag{11}$$

and has the property: $S^*(\mu) = S(-\mu^*)$, which is the same as that of the fermionic part of the QCD action.

This theory can be formulated using the (Noether) current variables in terms of which the partition function $\mathcal{Z}$ is explicitly positive definite:

$$\mathcal{Z} = \sum_{[k]} \prod_{x} \left\{ I_{k_{x,\alpha}}(\beta) e^{\mu\delta_{\alpha,t} k_{x,\alpha}} \right\} \delta\Big(\sum_{\alpha} (k_{x,\alpha} - k_{x-\alpha,\alpha}) \Big), \tag{12}$$

where the bond variables $k_{x,\alpha}$ describe "world-lines" or "current" of particles moving from lattice site x to the site $x + \hat{\alpha}$ and take integer values. I_k is the modified Bessel function of the first kind. The global $U(1)$ symmetry of the model is manifest in the local (Noether) current conservation relation represented by the delta function. We have used the worm algorithm to simulate this model.

At zero μ, the model has a second order phase transition at $\beta_c = 0.45421$ [34] going from a symmetric phase at low-β to a broken (superfluid) phase at large-β. We expect that at finite value μ, there is a line of second order transitions, specified by β_c, μ_c, between the superfluid and the normal phase. Non-trivial finite size effects in physical quantities, such as the number density $\rho(\mu)$ were observed. These could be explained by assuming that the energy levels cross each other in a finite volume as the chemical potential varies. As the μ is increased the average particle number changes from N to $N + 1$ at μ_c^N. By measuring the difference in energy, we have concluded that it costs energy to add an extra particle to the system, indicative of a repulsive interaction.

We have used universality arguments to determine the nature of the transition. For a second order transition, close to the critical chemical potential where the density can be made arbitrarily small, universal features emerge. It is known that, when the particles have a purely repulsive interaction, the ground state energy of N particles is always less than the corresponding energy of $N + 1$ particles [35]. Based on our results, this scenario seems to be valid in the current model. Thus, we conclude that at $\mu = \mu_c^{(0)}$ in the thermodynamic limit, there is a second order transition to a superfluid phase.

In the symmetric phase, the low energy physics contains massive bosons with repulsive interactions. The quantity $\mu_c^{(0)}$ is simply the mass of the particle $M(L)$ at

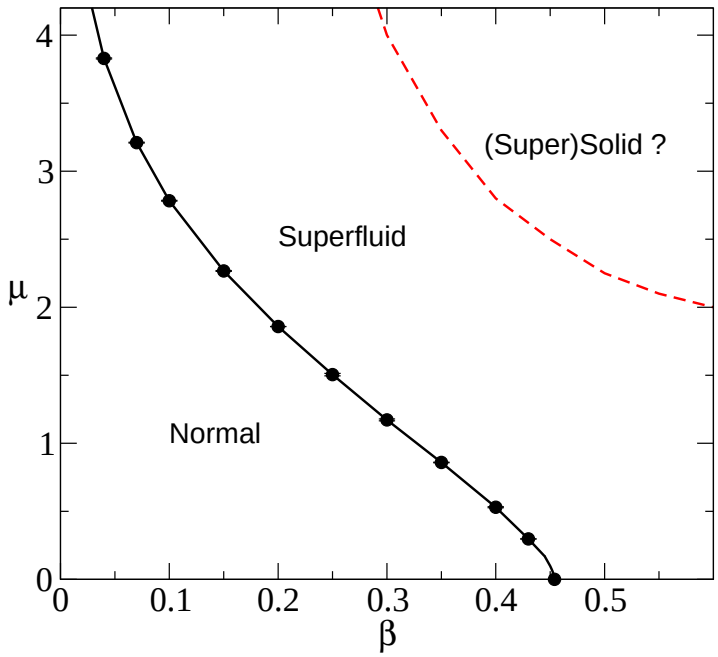

Figure 3: The phase diagram in the β vs. μ plane.

a finite L. The infinite volume mass can thus be obtained from:

$$M = \lim_{L\to\infty} \mu_c^{(0)}. \tag{13}$$

We can reverse this argument and obtain $\mu_c^{(0)}$ in the thermodynamic limit by simply measuring the mass of the particle at $\mu = 0$. Indeed, this result is not general and is valid only in the present study where there is clear evidence that the particles repel each other. The infinite volume extrapolation for the ground state works out very well, but the excited states have non-trivial dependences on $1/L$, which we did not study in detail. In the superfluid phase the $U(1)$ particle number symmetry is spontaneously broken, and there is a Goldstone boson in the spectrum. The low energy spectrum at finite volumes is expected to be governed by $O(2)$ chiral perturbation theory. Once again, we find that higher order corrections in 1/L are important to explain the infinite volume extrapolation.

While the complete phase diagram requires more work, our results above allow us to compute the location of the transition line between the normal phase and the superfluid phase. In particular the value of $\mu_c^{(0)}$ as a function of β determines this line. The second order phase boundary between the different phases is sketched in Fig.3. In principle there could be other interesting phases at larger values of μ which we cannot rule out based on the current work. Since the particles have a repulsive

interaction, there could a (super) solid phase at larger values of μ where the lattice structure becomes important. These transitions can also be studied efficiently with the worm algorithm. We have not studied this, but have speculated the possibility of a solid phase in Fig. 3.

Bibliography

[1] D. J. Gross, F. Wilczek *Phys.Rev.Lett.* **30**, 1343 (1973); H. J. Politzer, *Phys.Rev.Lett.* **30** 1346 (1973)

[2] Particle Data Group *Journal of Physics* **G 33**, 529 (2006)

[3] R. Gupta *Lectures given at the LXVIII Les Houches Summer School "Probing the Standard Model of Particle Interactions"* (1997)

[4] For a reference, see: T. DeGrand, C. DeTar *Lattice Methods for Quantum Chromodynamics*, World Scientific (2006)

[5] H. Nielsen, M. Ninomiya *Nucl. Phys.* **B185** 20 (1981)

[6] C. DeTar and U. Heller *Eur.Phys.J.* **A41**, 405 (2009)

[7] Proceedings of Quark Matter 2009

[8] D. Banerjee, R. V. Gavai, S. Gupta *Phys. Rev.* **D83**, 074510 (2011)

[9] D. Banerjee, S. Datta, R.V. Gavai and P. Majumdar; Manuscript under preparation

[10] K. Rajagopal and F. Wilczek *In Shifman, M. (ed.): At the frontier of particle physics* vol 3 2061 (2000)

[11] M. A. Stephanov,K. Rajagopal,E. Shuryak *Phys. Rev. Lett.* **D 80** 054509 (2009)

[12] For a review see: P. de Forcrand *PoS*(LAT2009) **010** (2009); S. Gupta *PoS* (LAT2010) **007** (2010)

[13] R. Narayanan, H. Neuberger *Phys. Rev. Lett.* **71** 3251 (1993); M. Lüscher *Phys. Lett.* **B 428** 342 (1998)

[14] J. Bloch, T. Wettig *Phys. Rev. Lett* **97**, 012003 (2006)

[15] D. Banerjee, R. V. Gavai and S. Sharma *Phys. Rev.* **D78** 014506 (2008)

[16] D. Banerjee, S. Chandrasekharan *Phys. Rev.* **D81** 125007 (2010)

[17] S. Gupta *Phys. Rev. D* **60** 094505 (1999)

[18] R.V. Gavai, S. Gupta, P. Majumdar *Phys. Rev.* **D65** 054506 (2002)

[19] STAR collaboration, B. I. Abelev et al., *Phys. Rev. Lett.* **98** 192301 (2007); PHENIX collaboration, A. Adare et al. *Phys. Rev. Lett.* **98** 172301 (2007)

[20] R. Rapp, H. van Hees *in Quark Gluon Plasma 4* arxiv: 0903.1096

[21] G. Moore, D. Teaney *Phys. Rev.* **C71** 064904 (2005)

[22] S. Caron-Huot, M. Laine, G. Moore *JHEP* **0904** 053 (2009)

[23] A. M. Polyakov *Nucl.Phys.* **B164** 171 (1980); V. S. Dostenko, S. N. Vergeles *Nucl.Phys.* **B169** 527 (1980); R. A. Brandt,F. Neri,M. Sato *Phys. Rev.* **D24** 879 (1981)

[24] P. Kolb, J. Sollfrank and U. Heinz *Phys. Rev.* **C62** 054909 (2000); D. Molnar and P. Huovinen *Phys. Rev. Lett.* **94** 012302 (2005)

[25] S. Gupta, K. Hubner, O. Kaczmarek *Phys. Rev.* **D77** 034503 (2008)

[26] H. van Hees and R. Rapp *Phys. Rev.* **C71** 034907 (2005)

[27] J. D. Roberts *Int. J. Control* **32** 677 (1980)

[28] P. Hasenfratz, F. Karsch *Phys. Lett.* **125B**, 308 (1983); N. Bilic, R. V. Gavai *Z. Phys.* **C 23** 77 (1984)

[29] R. V. Gavai *Phys. Rev.* **D 32** 519 (1985)

[30] Y. Kikukawa, A. Yamada *arXiv:hep-lat/9810024*; P. Hasenfratz et al., *Nucl. Phys.* **B643** 280 (2002); J. Mandula *arXiv:0712.0651*

[31] C. Gattringer, L. Liptak *Phys. Rev.* **D 76**, 054502 (2007)

[32] P. Rossi and U. Wolff *Nuclear Phys.* **B248** 105 (1984)

[33] N. Prokofév, B. Svistunov *Phys. Rev. Lett* **87**, 160601 (2001)

[34] M. Hasenbusch and S. Meyer *Phys. Lett.* **B241** 238 (1990)

[35] K. Sawada *Phys. Rev.* **116**, 1344 (1959)

Publications

- D. Banerjee, R. V. Gavai, S. Gupta "*Quasi-static probes of the QCD plasma*," Phys. Rev. D 83, 074510 (2010).
- D. Banerjee, S. Datta, R. V. Gavai and P. Majumdar; Manuscript under preparation
- D. Banerjee, R. V. Gavai and S. Sharma "*Thermodynamics of the ideal overlap quarks on the lattice* ," Phys. Rev. D78: 014506 (2008)
- D. Banerjee, S. Chandrasekharan "*Finite size effects in the presence of a chemical potential: A study in the classical non-linear O(2) sigma-model*," Phys. Rev. D81: 125007 (2010)

Chapter 1

Introduction

Quantum Chromodynamics (QCD) is the theory of strong interactions just as Quantum Electrodynamics (QED) is the theory of electromagnetic interactions of matter. QCD is a non-abelian gauge theory, where the gauge group is SU(3). This theory is formulated in terms of quarks and gluons, which are the elementary degrees of freedom. The quarks and gluons carry colour charges, analogous to the electric charges carried by the electron and proton. Unlike photons, the gluons carry colour charges.

QCD is asymptotically free [1], which means that the strength of interactions between the quarks and gluons is smaller for processes which involve large momentum transfer. Thus, perturbation theory can be used to study scattering problems in high-energy collider experiments. Despite numerous experimental efforts, isolated quarks and gluons however have not been seen [2]. This experimental fact lead to the hypothesis of confinement [3], which states that the quarks and gluons are permanently confined inside hadrons. The observed hadrons are colour-singlet bound states of quarks and gluons which occur in the physical spectrum at normal conditions of temperature and density. These bound states cannot be treated in perturbation theory. In the case of hydrogen atom, the binding energy for the constituent electron and proton is only about 13 eV, which is very small compared to their rest masses. On the other hand, the binding energy of the proton almost accounts for 99 % of the total mass. This is a clear indication of the large strength of the coupling and therefore show the inadequacy of the usual weak coupling methods.

A similar requirement for non-perturbative methods also seems to be essential to shed light on the interesting questions on matter at finite temperature and density. Asymptotic freedom leads to the expectation that at very large temperature and density, the equation of state of strongly interacting matter can be computed perturbatively, with the leading term corresponding to an ideal relativistic gas of quarks and gluons. Since then, a lot of work has been done using perturbative techniques

[4]. Unfortunately, the finite temperature perturbation theory breaks down due to the severe infra-red problems of QCD [5]. Moreover, in the interesting regions around the phase-transitions, the coupling is large and non-perturbative methods are called for. This leaves out many of the interesting questions from the regime of validity of perturbation theory. For example, the study of the medium that existed in the early universe, about 10-20 μ-seconds after the Big Bang or the nature of the transition that led to the formation of hadrons as this medium expanded and cooled. There is a worldwide experimental programme underway to study the nature and the properties of this transition. Heavy-ion collisions are used in experimental facilities such as the Relativistic Heavy Ion Collider (RHIC) in the Brookhaven National Laboratory (BNL), New York and the Large Hadron Collider (LHC) in European Centre for Nuclear Research (CERN), Geneva in an attempt to create such extreme temperatures and study the properties of the medium. It is therefore important to make theoretical investigations in details and to check the predictions of QCD against the data from these experiments.

QCD at zero temperature but large chemical potential is expected to have interesting phases such as the colour superconducting phase [6]. Calculations in models that have the same symmetries as QCD with 2+1 flavours of fermions, suggest that there is a line of first order phase transitions starting from $(T = 0, \mu_{c1})$ which ends at a critical point at (T_c, μ_c) [7], leading to a cross-over at the $\mu = 0$ axis. The location of this critical point in the (T, μ) phase diagram is an important problem that demands a non-perturbative method for its precise calculation. Strongly interacting matter at finite densities is expected to be produced in low energy runs at RHIC and in the experiments at the proposed FAIR (Facilities for Anti-Proton and Ion Research) at GSI, Darmstadt. These experiments will look for signals to detect the QCD-critical point (CEP) in the (T, μ) plane as well as the presence of other interesting phases that may exist at higher densities. QCD at finite densities is also needed to understand the conditions existing inside compact stellar objects, such as neutron stars, where the density can be as high as $10^{16} - 10^{17} g/cm^3$.

Lattice QCD is widely regarded as the robust method to perform reliable, precise and systematic calculations for the problems involving strongly interacting matter. Lattice QCD is a useful way of regularizing continuum QCD, which is otherwise plagued by ultraviolet(UV) divergences. The theory is formulated on a discrete space-time lattice with the lattice spacing acting as the UV regulator. Analytic treatment is possible in the limit $g^2 \to 0$ which is the usual weak coupling regime. For the theory defined on the lattice, analytic calculations can also be done in the strong coupling limit. However, it is not clear how to take continuum limit of those results.

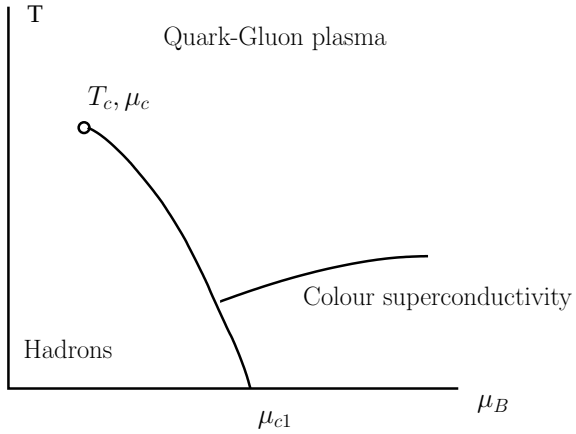

Figure 1.1: A schematic phase diagram of QCD with 2+1 flavours

Non-perturbative predictions of the theory are obtained by numerical simulations with Monte-Carlo methods [8]. In order to obtain reliable continuum results, the grid of the lattice needs to be fine (the $a \to 0$ limit) and the volume needs to be large such that the thermodynamic limit is reached. A significant advantage of this approach is that it involves no arbitrary assumptions or parameters as an input. Zero temperature calculations when compared with the experimentally measured values fix the bare parameters. Thus, starting from basic principles, the theory can be studied non-perturbatively.

Lattice QCD has been successful in the ab-initio calculation of the masses of all the light hadrons. It is being increasingly used [9] to make predictions about decay constants, running coupling, heavier hadrons, excited states, resonances and flavour physics. Lattice QCD has also been extensively used in investigations at finite temperature and density [10]. It has been used to obtain information about the thermodynamic and screening properties of the high temperature medium, the QCD equation of state at zero and small densities, the nature of the transition between low temperature and high temperature phases for different number of fermion flavours and the location of the CEP in the (T, μ_B) phase diagram. Recently, there have been efforts to calculate the transport coefficients of the medium that is expected to be produced in the heavy-ion collisions using the tools of lattice QCD.

1.1 Continuum QCD: Symmetries and Order Parameters

Thermodynamics of a many particle system can be obtained from its grand-canonical partition function $\mathcal{Z}$

$$\mathcal{Z} = \mathrm{Tr}\ \mathrm{e}^{-\beta(H-\mu N)}, \tag{1.1}$$

where H is the Hamiltonian of the theory and $\beta = 1/T$ is the inverse temperature. μ is the chemical potential that couples to the conserved number N (for example baryon number). For QCD, which is formulated in terms of the quark (ψ) and the gluon (A_μ) fields, $\mathcal{Z}$ can be written down as path integral [11]

$$\mathcal{Z} = \int_{bc} \mathcal{D}\psi\mathcal{D}\bar{\psi}\mathcal{D}A_\mu \exp\left[-\int_0^\beta d\tau \int d^3x \mathcal{L}\right], \tag{1.2}$$

where $\mathcal{L}$ is the Lagrangian and τ is the Euclidean time. In terms of the quark and gluon fields, the Lagrangian is

$$\mathcal{L}_{QCD} = \frac{1}{4}\mathrm{Tr}F_{\mu\nu}F_{\mu\nu} + \sum_{f=1}^{N_f}\{\bar{\psi}_f(\not{D} + m_f)\psi_f - \mu_f\bar{\psi}_f\gamma_0\psi_f\}, \tag{1.3}$$

where $F_{\mu\nu}$ is the field strength tensor $F^c_{\mu\nu} = \partial_\mu A^c_\nu - \partial_\nu A^c_\mu + g f_{abc} A^a_\mu A^b_\nu$, Tr denotes sum over the colour index and $\not{D}$ is the covariant derivative. μ_f and m_f are the chemical potential and quark mass of the fermion flavour f. The 'bc' in Eqn 1.2 denotes the boundary conditions on the quark and gluon fields, which arise due to the trace in Eqn 1.1:

$$A_\nu(\mathbf{x}, 0) = A_\nu(\mathbf{x}, 1/T), \tag{1.4}$$

$$\psi(\mathbf{x}, 0) = -\psi(\mathbf{x}, 1/T), \tag{1.5}$$

$$\bar{\psi}(\mathbf{x}, 0) = -\bar{\psi}(\mathbf{x}, 1/T), \qquad \forall \mathbf{x}, \nu. \tag{1.6}$$

QCD has global symmetries in the limits of infinite and vanishing quark mass. They can be utilized to obtain some ideas about the nature of possible phases. Further, effective models can be written down and analyzed in the standard Landau-Ginzburg paradigm in the theory of phase transitions. The order parameters corresponding to these symmetries are useful in locating the phase transitions, and are extensively used in numerical simulations. Since we are interested in studying QCD at finite temperature, it is useful to discuss the nature of the any new phase that may

arise at high temperature.

The low temperature phase at zero densities consist of the familiar colour-singlet states such as the mesons and the baryons. The phase at high temperatures is qualitatively different from the one at low temperatures. At temperatures several times larger than the transition temperature, the quarks and gluons no longer remain confined within the hadrons; they can get delocalized over large distances and exhibit screening. The resulting medium is known as the Quark Gluon Plasma (QGP) [12]. Lattice QCD studies provided the first convincing results of this transition.

The QCD action with N_f flavours of fermions have an exact $SU_L(N_f) \times SU_R(N_f) \times U_A(1) \times U_B(1)$ symmetry in the limit of vanishing quark mass. On quantization, the $U_A(1)$ symmetry is broken. The $U_B(1)$ is an exact symmetry of the action corresponding to baryon number. At low temperatures, the $SU_L(N_f) \times SU_R(N_f)$ chiral symmetry is spontaneously broken to the sub-group $SU(N_f)$. The order parameter that can test whether the vacuum respects chiral symmetry or not, is $\langle \bar{\psi}_f \psi_f \rangle$, called the chiral condensate. Lattice studies show that at low temperatures, the expectation value of this operator is non-zero, and the chiral symmetry is spontaneously broken, giving rise to nearly massless pions but heavy nucleons. Furthermore, as the temperature is raised, the chiral condensate vanishes beyond a certain temperature T_χ, and the chiral symmetry gets restored.

In the limit of infinite quark mass, only the contributions from the gluons matter. In this limit, the theory is the pure SU(3) gauge theory, sometimes referred to as Quenched QCD in the literature. Due to the boundary conditions on the gauge fields, the gauge transformations (see eq. 1.10) are also subject to periodic boundary conditions in $1/T$: $V(\mathbf{x}, 0) = V(\mathbf{x}, 1/T)$. In quenched QCD , the following extra global transformations are also allowed: $V(\mathbf{x}, 0) = zV(\mathbf{x}, 1/T)$, where $z \in Z(3)$, the centre of the gauge group. The action is invariant under this transformation. The corresponding order parameter is the Polyakov loop $L(\mathbf{x}) = \frac{1}{3}\mathrm{Tr} \prod_{\tau=1}^{N_t} U_4(\mathbf{x}, \tau)$, whose expectation value indicates whether the vacuum respects the symmetry or not. Under the above global $Z(3)$ transformation, $L(\mathbf{x}) \to zL(\mathbf{x})$. If the symmetry is respected, then $\langle L \rangle$ should vanish, whereas a non-zero value indicates that it is spontaneously broken. It can be shown [13] that $\langle L \rangle$ is related to the free energy of a static quark in gluonic medium at a temperature T:

$$|\langle L \rangle| \sim \exp(-F_Q(T)/T) \tag{1.7}$$

Lattice studies show that at very small temperatures, $\langle L \rangle = 0$. Thus, one expects that $F_Q = \infty$ in this phase, implying confinement of colour non-singlet states into

colour singlet objects. This is the usual hadronic phase we are familiar with. Further, it is seen that as the temperature is raised, the symmetry is broken at some temperature T_d and $\langle L \rangle \neq 0$, implying that isolated quarks can exist. This is a signature of deconfinement.

For real QCD with 2 light quarks and a heavier quark, none of the above two symmetries are exact. The presence of quarks causes the $Z(3)$ symmetry to break explicitly. Further, a mass term like $m\bar{\psi}\psi$ explicitly breaks the $SU(N_f) \times SU(N_f)$ symmetry to $SU(N_f)$. In an effective action picture, either of the symmetry breaking terms is analogous to the presence of a external magnetic field for spin systems. This has the effect of decreasing the strength of first order transitions, and converting the second order transitions into cross-over. Even then, the order parameters are useful indicators of these transitions, since they usually show a rapid change near the cross-over temperature. The corresponding susceptibilities are therefore usually used to determine the chiral transition temperature, T_χ and the deconfinement transition temperature T_d. Current calculations with improved staggered fermions at physical pion and kaon masses indicate that both these transitions occur in the range 150 - 170 MeV [14]. Indeed, there are other thermodynamic features of this transition. There is a rapid rise in energy density (and a slower rise in pressure) as the temperature is raised above the quark-hadron transition temperature.

1.2 Basics of Lattice QCD at finite temperature and density

Numerical lattice QCD aims at an evaluation of the expectation values of physical quantities starting from the Eqn. 1.2. The path integral in Eqn. 1.2 is ill-defined and needs to be regulated. A way of regulating Eqn. 1.2 that can satisfy the gauge invariance is to discretize the space and time [15]. Analogous to the evaluation of a simple integral as the limit of a sum, the complicated path-integral in Eqn 1.2 can then be performed. To preserve internal symmetries of the theory, such as gauge invariance, it is convenient to introduce the hypercubic space-time lattice. Thus, for a $N_s^3 \times N_t$ lattice, the volume and the temperature is expressed in terms of the lattice spacing a:

$$V = (N_s a_s)^3, \qquad T = \frac{1}{N_t a}. \tag{1.8}$$

Defining the gauge fields and the quark fields on the lattice, the path integral is reduced to a multidimensional integral with a very large dimensionality. Moreover, the lattice spacing acts as an ultra-violet cut-off and provides a regularization scheme

necessary for the quantum field theory.

The lattice formulation defines the quark and the anti-quark fields $\psi(x)$, $\bar{\psi}(x)$ on the lattice sites $x = (x_0, x_1, x_2, x_3)$ and they carry the colour, flavour and spin indices. They are Grassman variables and satisfy the usual anti-commuting properties:

$$\begin{aligned} \{\bar{\psi}(x), \psi(y)\} &\equiv \bar{\psi}(x)\psi(y) + \psi(y)\bar{\psi}(x) = 0, \\ \{\psi(x), \psi(y)\} &= 0, \qquad \forall x, y. \end{aligned} \tag{1.9}$$

The SU(3) matrix-valued gauge fields, $U_\mu(x)$ are defined on the links connecting the lattice sites x to $x + \hat{\mu}$, where $\hat{\mu}$ is the unit vector along the μ-th direction. Even though the lattice formulation explicitly breaks Lorentz invariance (which is restored only in the $a \to 0$ limit), gauge invariance is exactly maintained at all finite lattice spacings. For a local gauge transformation $V(x) \in SU(3)$ the quark and the gluon fields have the following transformation properties:

$$\begin{aligned} \psi(x) \to \psi'(x) &= V(x)\psi(x), \\ U_\mu(x) \to U'_\mu(x) &= V(x)U_\mu(x)V^\dagger(x+\mu). \end{aligned} \tag{1.10}$$

The construction of gauge invariant actions need the trace of closed loops. The smallest of these loops are called plaquettes: $U_{\mu\nu}$ and these are used to define the standard gluon action S_G [15]:

$$\begin{aligned} U_{\mu\nu}(x) &= \mathrm{Tr}(U_\mu(x)U_\nu(x+\mu)U^\dagger_\mu(x+\nu)U^\dagger_\nu(x)), \\ S_G &= \frac{6}{g^2}\sum_{x,\mu<\nu}(1 - \frac{1}{3}\mathrm{Re}U_{\mu\nu}(x)) \end{aligned} \tag{1.11}$$

The SU(3) link field $U_\mu(x)$ is related to the colour vector potential field $A^c_\mu\lambda_c$ through $U_\mu(x) = \exp(igaA^c_\mu(x)\lambda_c)$ where λ_c for $c = 1, 2, 3, \cdots, 8$ are the eight generators of the SU(3) group and g is the gauge coupling constant. In the continuum limit $a \to 0$, the link fields can be expanded in powers of a, and the Wilson action becomes

$$S_G = \int_0^\beta d\tau \int d^3x \frac{1}{4}(F^c_{\mu\nu})^2 + \mathcal{O}(a^2). \tag{1.12}$$

The fermionic part of the QCD action is generically written as

$$S_F = \sum_{m,n} \bar{\psi}_m D_{m,n} \psi_n, \tag{1.13}$$

where $D_{m,n}$ is Dirac operator. The Dirac operator is γ_5-Hermitian, which means that

$D^\dagger = \gamma_5 D \gamma_5$. This property is of great use when dealing with numerical simulations with fermions. Usually the fermions fields are integrated out in the expression for the partition function. This gives the determinant of the Dirac operator in the expression for the path integral

$$\mathcal{Z} = \int \prod_{x,\hat{\mu}} dU_x^\mu \ \exp(-S_G) \ \det D, \tag{1.14}$$

where flavour index is kept implicit in the Dirac operator. The expectation value of an operator $\mathcal{O}$ is calculated using

$$\langle \mathcal{O} \rangle = \frac{1}{\mathcal{Z}} \int_{bc} dU_x^\mu \ \mathcal{O} \ \exp \ (-S_G(U_x^\mu)) \ \det D \tag{1.15}$$

The γ_5-Hermiticity of the Dirac operator implies that the fermion determinant is real. For even N_f, this makes Monte-Carlo estimates of expectation values of the operators feasible since $\exp\,(-S_G(U_x^\mu))\,\det D$ is explicitly positive definite and can be interpreted as the probability weight for performing the integrals.

The naive discretization of the fermion action in QCD is not suitable because of the doubling problem [8]. The lattice propagator for the naive Dirac fermions is

$$S(p) = \frac{-i\gamma_\mu \sin(p_\mu a) + ma}{\sum_\mu \sin^2(p_\mu a) + m^2 a^2}. \tag{1.16}$$

The lattice momenta p_μ range between $-\pi/a$ to π/a. In the continuum limit, the propagator is dominated by contributions from $ap = (0,0,0,0)$ as well as from the edges of the Brillouin zone $ap = (\pi,0,0,0), (0,\pi,0,0), \cdots, (\pi,\pi,\pi,\pi)$. This causes the appearance of extra doubler states in the spectrum from the edges of the Brillouin zone. Starting from a single Dirac field on the lattice, gives rise to 16 fermion flavours in 4 dimensions in the continuum. This doubling problem is the essence of the no-go theorem of Nielsen and Ninomiya [16], which states that for a fermion action that respects hermiticity, locality, translational invariance and has chiral symmetry, doubling is inevitable.

Wilson fermions break chiral symmetry explicitly by having momentum dependent mass for the doubler states that goes to infinity in the continuum limit; thus decoupling the doubler states from the spectrum in the continuum [15]. The action

for the Wilson fermions is

$$\begin{aligned} S_F^{Wilson} &= \frac{1}{2a}\sum_{n,\mu}\left[\bar{\psi}_n\gamma_\mu U_\mu(n)\psi_{n+\mu} - \bar{\psi}_n\gamma_\mu U_\mu(n-\mu)^\dagger\psi_{n-\mu}\right] + m\sum_n \bar{\psi}_n\psi_n \\ &- \frac{r}{2a}\sum_{n,\mu}\bar{\psi}_n\left(\psi_{n+\mu}+\psi_{n-\mu}-2\psi_n\right). \end{aligned} \tag{1.17}$$

The last term in Eqn 1.17 contributes to the mass of the doubler states. Even for $m = 0$, the last term breaks chiral symmetry. This makes the Wilson fermions unsuited for the study of chiral symmetry restoration at high temperatures. However, the Wilson fermions do have the advantage of a clear definition of flavours and spin on the lattice.

The staggered formulation [17] overcomes the doubling problem by distributing the fermionic degrees of freedom over the lattice such that the effective lattice spacing for each type of quark is doubled. The advantage of this formulation is that it preserves an exact U(1) $\times$ U(1) chiral symmetry for all lattice spacings. This makes it useful in the study of problems related to chiral symmetry. The staggered fermion action has the following form:

$$S = \frac{1}{2a}\sum_{n,\mu}\bar{\chi}_n\alpha_\mu(n)\left[U_\mu(n)\chi_{n+\mu} - U_\mu^\dagger(n-\mu)\chi_{n-\mu}\right] + m\sum_n\bar{\chi}_n\chi_n, \tag{1.18}$$

$$\alpha_\mu(n) = (-1)^{n_0+n_1+\cdots+n_{\mu-1}}. \tag{1.19}$$

Here χ and $\bar{\chi}$ are the single component spinors. The main disadvantage of the staggered fermion formulation is that "flavour" is not a well defined concept.

The Overlap operator [18] has much better chiral properties. It can be defined in terms of the Wilson-Dirac operator (D_W) as:

$$D = \frac{1}{a}(1 - \mathrm{sgn}(1 - aD_W)), \tag{1.20}$$

where D_W is the Wilson-Dirac operator of the Wilson fermions in Eqn. 1.17 and sgn is the matrix sign function. This operator has a form of chiral invariance on the lattice: the following transformation [19]

$$\delta\psi = \alpha\gamma_5(1 - \frac{1}{2}aD)\psi, \qquad \delta\bar{\psi} = \alpha\bar{\psi}(1 - \frac{1}{2}aD)\gamma_5, \tag{1.21}$$

leaves the fermion action invariant for all lattice spacings a. Note that in the continuum limit this reduces to the usual definition of chirality. This is interpreted as

exact chiral symmetry for $a \neq 0$. It is important to note that the invariance of the fermionic action with the overlap operator requires the overlap Dirac operator to satisfy the Ginsparg-Wilson relation [20]: $\{\gamma_5, D\} = aD\gamma_5 D$. The overlap operator is clearly better suited than the staggered fermions to study problems pertaining to chiral symmetry. However, the overlap operator is highly non-local, and hence it is expensive to implement it in numerical simulations.

To investigate finite densities, the chemical potential is introduced as the variable conjugate to the conserved number operator. The quark number is the conserved charge of the U(1) global symmetry. The natural way to introduce μ is to construct the number density for the lattice action [21, 22]. The lattice Noether current determined in this way gives a current expressed by nearest neighbour terms. If the chemical potential is introduced in this way, then temporal hopping terms become

$$\frac{1}{2a}\sum_x \left[\bar{\psi}(x)(1+a\mu)(1-\gamma_4)U_4(x)\psi(x+\hat{4}) + \bar{\psi}(x)(1-a\mu)(1+\gamma_4)U_4(x-\mu)^\dagger\psi(x-\hat{4})\right].$$

The calculation of the energy density and the number density in the presence of μ gives rise to divergences proportional to a^{-2}. In order to get rid of that, μ is introduced as the imaginary fourth component of an abelian gauge field [21]. This changes the μ dependence in the action to $f(a\mu)$ and $g(a\mu)$ multiplying the forward and the backward hopping terms respectively. It was shown that the divergences are removed with the condition $f(a\mu).g(a\mu) = 1$ [23]. The most common choice of these functions in the literature are: $f(a\mu) = g(a\mu)^{-1} = \exp(a\mu)$.

In the presence of a finite chemical potential, the Dirac operator loses its usual hermiticity properties. Instead it satisfies the relation: $\gamma_5 D(\mu)\gamma_5 = D^\dagger(-\mu)$. This relation, however, is not enough to guarantee the reality of the fermion determinant. Instead, the fermion determinant satisfies the relation: $\det[D(\mu)] = \det[D(-\mu^*)]^*$. Monte-Carlo simulations cannot be carried out since the fermionic determinant is complex in general, and the theory is said to have a sign problem.

There are several methods in use in the literature to get around this problem [24]

- Imaginary chemical potential [25]: Using imaginary chemical potential makes the fermion determinant positive definite, and therefore Monte-Carlo simulations can be carried out as usual. However, the result needs to be analytically continued to the real μ. The analytic continuation of set of numbers with error-bars is a difficult problem, and usually involves unknown systematic uncertainties.

- Reweighting [26]: In this method, the complex determinant is separated into

a modulus and a phase, $\det D(\mu) = |\det D(\mu)| \exp(i\phi)$, and the phase-quenched ensemble (|det (D)|) is simulated. The expectation values are computed by compounding the phase with the operator:

$$\langle \mathcal{O} \rangle = \frac{\langle \mathcal{O} \exp(\imath\phi) \rangle_{|\det\ (\mathrm{D})|}}{\langle \exp(\imath\phi) \rangle_{|\det\ (\mathrm{D})|}} \tag{1.22}$$

For values of the chemical potential when the phase starts becoming large, the expectation in the denominator vanishes and the measurements become ill-defined.

- Taylor expansion [27]: This method tries to overcome the sign problem at high temperatures by doing a Taylor expansion in $\frac{\mu}{T}$. For example, the pressure at finite μ and large T, $\Delta P(T,\mu) \equiv P(T,\mu) - P(T,\mu=0)$, can be expanded about $\mu/T = 0$, in powers of μ/T:

$$\frac{\Delta P(T,\mu)}{T^4} = \sum_{k=1}^{\infty} c_{2k} \left(\frac{\mu}{T}\right)^{2k}; \quad c_{2k} = \left\langle \mathrm{Tr}\left[f\left(D^{-1}, \frac{\partial D}{\partial \mu} \right) \right] \right\rangle \Bigg|_{\mu/T=0} \tag{1.23}$$

  where f is a polynomial of degree $2k$ of the indicated arguments. The coefficients are calculated in the $\mu = 0$ theory. An improved alternate version of this method considers the expansion of the susceptibilities in terms of Taylor coefficients. A disadvantage of this method is that a large number of Taylor coefficients may be needed, making their computation very difficult.

- Complex Langevin : This method uses the techniques of stochastic quantization [28] to compute the expectation values of the observables. This has not been applied on full QCD with chemical potential yet. This method suffers from convergence problems and instabilities in some of the simpler models it has been tested.

- World-Line methods: It is known [29] that a sign problem present in a theory formulated with one set of field variables might be eliminated if other degrees of freedom are used. The world-line methods aim at this reformulation. Progress in this method is rather slow, since this method is not generic and choosing the right degrees of freedom for each theory requires a lot of insight. At present, this has only been tried on simpler models.

1.3 Outline of the thesis

In this thesis, I will present my research about the different aspects of non-perturbative thermodynamics at finite temperature and density. In this section, I will discuss the broad themes for each of the works chapter wise and outline the major results.

In the second chapter, the medium properties of QCD with 2-fermion flavours will be studied. While the equation of state does give thermodynamic information about the medium, more details are needed in order to understand the nature and composition of the medium. Screening lengths are such quantities [30] which give information about the spatial distance beyond which the effects of putting a test hadron in the medium are screened. The screening lengths are extracted from the exponential fall-off of the long distance part of the spatial correlation function. The screening correlators are also important for studying the restoration of symmetries of the medium. In particular, when the correlation lengths in two different quantum number channels related by chiral symmetry transformation becomes identical, chiral symmetry of the medium is restored.

Screening properties in a plasma have been extensively studied in the literature. In the glue sector, the Debye screening length has been the object of many studies and now seems to be quantitatively understood, both in non-perturbative lattice studies [31] and in weak coupling theory at high temperatures [32]. Screening in other quantum number channels in the glue sector has also been studied [33]. Screening in colour singlet channels due to quark bilinear (meson-like) and trilinear (baryon-like) currents [30] was understood as the first signal of deconfinement above the chiral symmetry restoring temperature in QCD with dynamical quarks [34]. In Chapter 2, I will study the pattern of chiral symmetry restoration in 2-flavour QCD with staggered fermions across the quark-hadron transition [35]. I will use the screening masses of the mesonic operators in various quantum number channels as a diagnostic of the symmetry restoration of the medium.

Chapter 3 will be concerned with the calculation of a transport coefficient of heavy quarks in the gluonic medium. While the screening masses provide a theoretical understanding of the large scale composition of the strongly interacting matter expected to be created in the heavy ion collision experiments it is difficult to relate to experimental quantities. Other quantities can be calculated which allow for a comparison with experimental data. One such quantity is the thermalization time for heavy quarks. This quantity has been inferred for the charm quark by the PHENIX experiment at RHIC [36]. Experimentally, it seems that both the light and the heavy quarks thermalize at the same rate [37]. This is quite in contrast to that expected

from weak-coupling methods, which estimate the thermalization time of the heavy quarks to be suppressed by a factor $\sim T/M$ to that of light quarks, where T is the temperature of the medium and M is the mass of the heavy quark. It is suspected that the effects of strong coupling might be important to make theoretical estimates that compare favourably with experimental results. A calculation using AdS/CFT methods estimate the value of the dimensionless diffusion coefficient to be about an order of magnitude larger than the perturbative estimate [38, 39]. In Chapter 3, I will present a non-perturbative computation of the thermalization time of heavy quarks in a gluon medium from first principles [40]. I will subsequently show that the results are closer to the estimates required by models which successfully explain the experimental data than the predictions from weak coupling methods.

Most studies of QCD at finite temperature and density use staggered fermions, either in their original version, or improved ones [8]. Since the symmetry group of these fermions on the lattice is different from that of continuum QCD, it is more desirable to use fermions with exact chiral symmetry and with the right flavour symmetries to address the issues while working on relatively coarser lattices. The Overlap fermion [18] is one such candidate. However, the non-locality of the overlap fermions makes them very expensive to implement numerically. Moreover, it is the non-locality that makes the construction of a conserved quark number non-trivial, which in turn, is essential for the inclusion of the quark chemical potential. The lattice investigation of the CEP in the $T-\mu_B$ plane of real-world QCD with two light quarks and a strange quark, therefore requires a conceptually sound definition of the overlap operator with a chemical potential. This is of significant importance, since the theoretical studies greatly complement the current experimental searches for the CEP already underway in the low-energy runs of RHIC. We have already discussed the procedure of including the chemical potential in the fermion action. While this procedure is straightforward to implement in the case of Wilson and Staggered fermions, it is non-trivial for the case of overlap fermions, due to its non-locality. The existing formulation of overlap fermions at finite μ employs an educated guess to include the chemical potential in such a way that the correct continuum limit of the action is reproduced [41]. In Chapter 4, I will present an analytical study of this formulation, and will show that the correct expressions for the thermodynamic quantities, such as the energy density, pressure and the equation of state is obtained [42]. I will also show that the conditions needed to avoid the appearance of the spurious a^{-2} divergences in the expressions for the energy density and the number density in continuum limit are the same as that for the local fermions. However, it has been shown that in this formulation the exact chiral symmetry of the overlap at $\mu = 0$ is lost at finite μ [42].

Even if the problem of proper inclusion of the chemical potential in the overlap operator is solved, a non-perturbative study at finite density would require the elimination of the sign problem. Practical calculations using Taylor expansion and reweighting methods can be done in the restricted parameter regime of large temperature and small μ. The alternate methods of formulation of the theory have not yet been successful in producing a sign problem free computational framework. There has however been considerable success in the implementation of the these methods to simpler bosonic and fermionic models, which share certain common features with QCD. It is generally accepted that the experience with the simpler theories would provide valuable insight, both physical and computational, to be of use in formulating the more difficult case of full QCD. In Chapter 5, I will present a study of the non-linear O(2)-sigma model, which has a similar sign problem at finite chemical potential as that of QCD. The sign problem in this model can be eliminated by reformulating the theory in terms of conserved currents, and I will describe the computational framework that has been adopted in explaining the phase diagram at finite density and low temperature [43]. In fact, this is the only method that can be used to eliminate the sign problem in this model and perform numerical simulations. Applications of the complex Langevin method to this model found that the results converged to wrong values. It was realized that complex Langevin dynamics was responsible for the wrong convergence [44].

References

[1] D. J. Gross, F. Wilczek; *Phys. Rev. Lett.* 30, 1343 (1973)
H. J. Politzer; *Phys. Rev. Lett.* 30 1346 (1973)

[2] Particle Data Group; *Journal of Physics* G 33, 529 (2006)

[3] For a review see: J. Greensite; *Prog. Part. Nucl. Phys.* 51, 1, (2003)

[4] J. P. Blaizot and E. Iancu; *Phys. Rept.* 359, 355 (2002)

[5] A. Linde; *Rep. Prog. Phys.* 42, 389 (1979)

[6] K. Rajagopal and F. Wilczek; *In Shifman, M. (ed.): At the frontier of particle physics* Vol 3 2061 (2000)

[7] M. A. Stephanov, K. Rajagopal, E. Shuryak; *Phys. Rev.* D60 (1999) 114028

[8] For a reference, see: T. DeGrand, C. DeTar; *Lattice Methods for Quantum Chromodynamics* World Scientific (2006)

[9] C. DeTar and S. Gottlieb; *Phys.Today* 57N2 (2004) 45-51
HPQCD, UKQCD, MILC and Fermilab Lattice Collaborations (C. T. H. Davies et. al.) *Phys. Rev. Lett.* 92 (2004) 022001
BMW Collaboration (S. Durr et. al.); *Science* 322 (2008) 1224-1227

[10] C. DeTar and U. Heller; *Eur. Phys. J.* A 41 (405), 2009

[11] M. LeBellac; *Thermal Field Theory* Cambridge University Press,1996

[12] For a review see: J. Cleymans, R. V. Gavai and E. Suhonen; *Phys. Rept.* 130, 217 (1986)

[13] L. McLerran and B. Svetitsky; *Phys. Rev.* D24, 450 (1981); *Phys. Rev.* D24, 450 (1981);
J. Kuti, J. Polónyi and K. Szlachányi; *Phys. Lett.* 98B, 199 (1981)

[14] Y. Aoki et. al., (Wuppertal-Budapest-Marseille Collaboration); *JHEP* 1009 (2010) 073

[15] K. Wilson; *Phys. Rev.* 10, 2445 (1974)

[16] H. Nielsen, M. Ninomiya; *Nucl. Phys.* B185 20 (1981)

[17] J. B. Kogut and L. Susskind; *Phys. Rev.* D11, 395 (1975)

[18] R. Narayanan, H. Neuberger; *Phys. Rev. Lett.* 71 3251 (1993)

[19] M. Lüscher; *Phys. Lett.* B 428 342 (1998)

[20] P. H. Ginsparg and K. G. Wilson; *Phys. Rev.* D25, 2649 (1982)

[21] P. Hasenfratz, F. Karsch; *Phys. Lett.* 125B, 308 (1983)

[22] N. Bilic, R. V. Gavai; *Z. Phys.* C 23 77 (1984)

[23] R. V. Gavai; *Phys. Rev.* D 32 519 (1985)

[24] P. de Forcrand; **PoS LATTICE** 2009, 010, (2009)
S. Gupta; **PoS LATTICE** 2010, 007, (2010)

[25] P. de Forcrand and O. Philipsen; *Nucl. Phys.* B642 (2002) 290-306

[26] Z. Fodor and S. Katz; *JHEP* 0203 (2002) 014

[27] C. R. Allton et. al.; *Phys. Rev.* D66 (2002) 074507
R. V. Gavai and S. Gupta; *Phys. Rev.* D68 (2003) 034506

[28] G. Aarts and I. O. Stamatescu; **PoS LATTICE** 176, 2008

[29] S. Chandrasekharan; **PoS LATTICE** 2008, 003 (2008)
U. Wolff; **PoS LATTICE** 2010, 020 (2010)

[30] C. DeTar and J. B. Kogut *Phys. Rev.* D36, 2828 (1987)

[31] O. Kaczmarek; **PoS CPOD** 07 (2007) 043.

[32] K. Kajantie et. al; *Phys. Rev. Lett.* 79 (1997) 3130

[33] S. Datta and S. Gupta; *Nucl. Phys.* B 534 (1998) 392

[34] K. D. Born et. al. (MT_c Collaboration); *Phys. Rev. Lett.* 67 (1991) 302.

[35] D. Banerjee, R. V. Gavai, S. Gupta; *Phys. Rev.* D83, 074510 (2011)

[36] A. Adare et al.; *arXiv*: 1005:1627

[37] R. Rapp, H. van Hees; *In Quark Gluon Plasma 4, arxiv*: 0903.1096

[38] J. Casalderrey-Solana and D. Teaney; *Phys. Rev.* D74, 085012 (2006)

[39] G. Moore and D. Teaney; *Phys. Rev.* C 71, 064904 (2005)

[40] D. Banerjee, S. Datta, R. V. Gavai and P. Majumdar; *In preparation*

[41] J. Bloch, T. Wettig; *Phys. Rev. Lett.* 97, 012003 (2006)

[42] D. Banerjee, R. V. Gavai and S. Sharma; *Phys. Rev.* D78 014506 (2008)

[43] D. Banerjee, S. Chandrasekharan; *Phys. Rev.* D81 125007 (2010)

[44] F. James and G. Aarts; *JHEP* 1008 (2010) 020

Chapter 2

Screening correlators as QGP probes

2.1 Introduction

A generic method to study the properties of a medium is to record the response of the medium to external probes. One such probe is the screening length which indicates the spatial distance beyond which the effects of putting a test hadron in the medium is screened. Of particular interest is the longest screening length, ξ_0, or its inverse, the smallest screening mass, $\mu_0 = 1/\xi_0$ [1]. For the QCD plasma with non-vanishing quark masses, it is known that all fields are screened [1, 2]. Nevertheless, an understanding of screening masses is of practical importance for the study of matter in high-energy collisions. If ℓ is the smallest dimension of the fireball produced in heavy-ion collisions, then thermodynamic properties become manifest only when $\ell\mu_0 \gg 1$. In the other limit, the system would be subject to finite size effects and the thermodynamic results from lattice QCD calculations may not be directly applicable.

Screening properties in a plasma have been extensively studied in the literature. In the glue sector, the Debye screening length has been the object of many studies both in non-perturbative lattice studies [3] and in weak coupling theory at high temperatures [4]. Screening in other quantum number channels in the glue sector has also been studied [5]. Screening in colour singlet channels due to quark bilinear (meson-like) and trilinear (baryon-like) currents [1] was understood as the first signal of deconfinement above the chiral symmetry restoring temperature in QCD with dynamical quarks [6]. Analyticity arguments relate these hadron-like screening masses in the low-temperature confined and chiral symmetry broken phase to the (pole) masses and properties of the hadrons. This has implications for models of

heavy-ion collisions such as the hadron resonance gas model.

Hadron-like screening masses have been studied previously in [7, 8]. In QCD with light dynamical quarks they have been studied before using 2 flavours of staggered quarks [9] and with 2+1 flavours of p4 improved quarks [10]. They have been studied also with overlap valence quarks [11]. In all these studies the renormalized light quark masses are almost equal, and nearly physical. It is known that while the chiral symmetry restoration in the vector and axial-vector channels happens just after T_c (the cross-over temperature of the theory), this restoration happens at higher temperatures in the scalar and pseudo-scalar channels. The scalar and pseudo-scalar screening lengths approach the free theory limit more slowly than the vector axial-vector screening lengths.

In this work, we extend previous studies through the analysis of meson-like spatial correlation functions in 2-flavour QCD with staggered quarks. This brings the state of the art for dynamical staggered quarks into the regime of lattice spacings already reached using quenched overlap quarks. We will discuss our studies of chiral symmetry restoration in the 2-flavour QCD using the screening masses and correlators [12, 13]. We will present a detailed study of this hierarchical symmetry restoration in the screening lengths of the various mesons and also locate the temperature at which the scalar and pseudo-scalar screening lengths become identical using several different diagnostics. We will describe our efforts to shed more light on the issue of different symmetry restoration temperatures in different quantum number channels by controlling the amount of explicit chiral symmetry breaking by tuning the quark mass. We further checked for stability of the mesonic states and do not find any signature of decay in the confined phase.

2.2 Formalism and Analysis details

A large part of this study uses decorrelated gauge configurations described in [14]. Two light flavours of staggered quarks were used with the bare quark mass tuned so as to give $m_\pi \simeq 230$ MeV at zero temperature. The lattice spacing was $a = 1/(6T)$. The T_c was identified through the peak of the Polyakov loop susceptibility. The lattice sizes in the range $12 \leq N_s \leq 24$ were used. The aspect ratio $\zeta = N_s/N_t$ was always between 2 and 4. Most of our results are reported for the largest volumes, $\zeta = 4$. A detailed finite volume scaling study was performed at $T = 0.94T_c$ with $4/3 \leq \zeta \leq 5$. We have used at least 50 decorrelated configurations for our measurements.

The meson screening correlation functions are studied in one spatial directions

with other spatial and temporal directions summed over and are given by—

$$C_z^\gamma = \frac{1}{\mathcal{V}} \left\langle \sum_{\mathbf{x}} \mathrm{Tr}\left[G(\mathbf{x},z)G^\dagger(\mathbf{x},z)\right] \phi_\gamma(\mathbf{x}) \right\rangle \tag{2.1}$$

where $\mathbf{x}$ stands for sites labelled by the triplet (x,y,t), $\mathcal{V} = N_x N_y N_t$, $G(\mathbf{x},z)$ is the inverse of the Dirac operator, i.e., the quark propagator from the origin to the point $(\mathbf{x},z)$, the angular brackets denote an average over gauge field configurations with the correct weight, and the staggered phase factors $\phi_\gamma(\mathbf{x})$ pick out the quantum numbers, γ, of the meson under study.

All eight possible local staggered mesons have been studied here. At $T = 0$ they would correspond to the flavour non-singlet scalar (S) (corresponding to the a_0 meson), the Goldstone pion (PS), and three components each of the local vector meson (V) and the axial vector (AV). Symmetry operations of the spatial slice interchange the components of the V and AV, so the three components are expected to be identical after averaging over gauge configurations.

Since we measure spatial direction correlators at finite temperature, the symmetries of the (x,y,t) slice orthogonal to the direction of propagation are not the same as they would be in the corresponding zero temperature computation [15]. The S/PS operators both lie in the trivial representation, called the A_1^{++}, of the spatial direction transfer matrix. The sum of the x and y polarizations of the V/AV, and, separately, the t polarization, also lie in the A_1^{++} representation. These six different kinds of A_1^{++} operators do not mix under the symmetries of the (x,y,t) slice, and hence we need separate notations for them. For the S/PS correlators it is economical to carry on the $T = 0$ notation. For the sum of the x and y polarizations of the V we use the notation Vs (and AVs for the sum in the AV sector) and for the t polarizations we use the notation Vt and AVt. The difference of the x and y polarizations of the V/AV lie in a non-trivial representation called the B_1^{++}. We use the notation VB and AVB for these. These particular realizations of the B_1^{++} correlator have earlier been seen to vanish [16].

We will use the S and PS susceptibilities [17] defined as

$$\chi_{PS} = \sum_z C_z^{PS}, \qquad \text{and} \qquad \chi_S = \sum_z (-1)^z C_z^S. \tag{2.2}$$

to demonstrate that at high temperatures the S/PS correlators are essentially dominated by a single parity state.

The inversion of the Dirac operator was done using a conjugate gradient (CG)

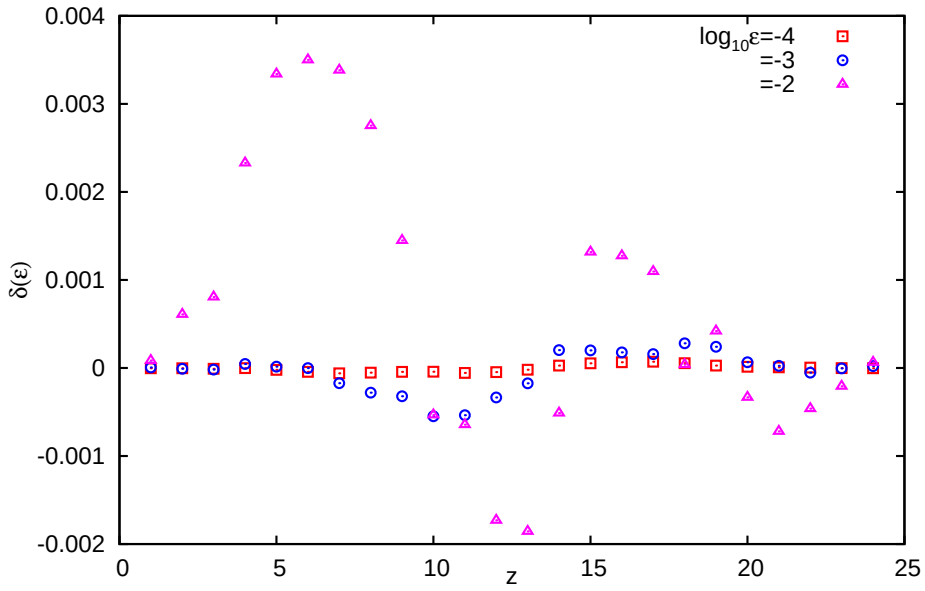

Figure 2.1: $\delta(\epsilon)$, see eq. (2.3), as a function of the separation z for varying ϵ, with a fixed value of $\epsilon' = 10^{-5}$.

algorithm. The tolerance for stopping was chosen such that the residual vector had squared norm less than $\epsilon N_t N_s^3$. We investigated whether we had an acceptable stopping criterion by monitoring

$$\delta(\epsilon) = 1 - \frac{C^{PS}[\epsilon]}{C^{PS}[\epsilon']} \tag{2.3}$$

where $C^{PS}[\epsilon]$ is the PS correlation function obtained when the stopping tolerance parameter is ϵ. We chose a fixed $\epsilon' = 10^{-5}$. Figure 2.1 shows δ computed on a randomly chosen test configuration at $T = 0.94T_c$ with $\zeta = 4$. The configuration to configuration variance of C^{PS} is about 2–5% of the expectation value, so keeping $\delta < 0.01$ suffices. Clearly, the errors converge fast, and our choice of $\epsilon = 10^{-5}$ is seen to be more than sufficient.

Each staggered correlation function may contain contributions from two parity partners, and can be parameterized through the doubled-parity fit

$$C(z) = A_1(\mathrm{e}^{-\mu_1 z} + \mathrm{e}^{-\mu_1(N_z - z)}) + (-1)^z A_2(\mathrm{e}^{-\mu_2 z} + \mathrm{e}^{-\mu_2(N_z - z)}), \tag{2.4}$$

where μ_1 and μ_2 are the screening masses of the lightest natural parity meson appropriate for the operator used and its opposite parity partner.

Since measurements of the correlation function at different distances, z, are made using the same gauge configurations, they are correlated, and the fit must take care

of these correlations. Therefore, we used the definition of χ^2

$$\chi^2 = \sum_{zz'} \left[C_z - C(z)\right] \Sigma^{-1}_{zz'} \left[C_{z'} - C(z')\right]. \tag{2.5}$$

Here z is the spatial separation, C_z are the measured expectation values of eq. (2.1), the function $C(z)$ is the 2-mass form of eq. (2.4), and $\Sigma_{zz'}$ is the covariance of C_z and $C_{z'}$. When $\Sigma_{zz'}$ is diagonal, the definition reduces to the more familiar one. In actuality, the correlation coefficients are fairly high, so the matrix $\Sigma_{zz'}$ is nearly singular. The inversion was done in Mathematica to an accuracy of $\mathcal{O}(10^{-10})$. The errors in the inversion were therefore negligible compared to the statistical errors in the measurements, σ_z, which were of the order of a few percent.

Local masses were used as a consistency check on the results obtained from fits. Due to the even-odd oscillations for staggered fermions, we used the definition of [9]—

$$\frac{C_{z+1}}{C_{z-1}} = \frac{\cosh[-m(z)(z+1-N_z/2)]}{\cosh[-m(z)(z-1-N_z/2)]}. \tag{2.6}$$

Given the measurement on the left, the effective mass, $m(z)$, can be extracted by solving the equation and errors estimated by jack-knife. This differs from a procedure where successive time slices are used for the modified correlator $(-1)^z C_z$ [10].

In the chiral symmetry broken phase there is no particular relation between μ_1, μ_2 and A_1, A_2 for different correlators. However, when chiral symmetry is restored, the staggered phases give

$$C_z^{PS} = (-1)^z C_z^S, \qquad C_z^{AVs} = (-1)^z C_z^{Vs}, \qquad C_z^{AVt} = (-1)^z C_z^{Vt}. \tag{2.7}$$

This implies the relations

$$A_1^{Vs} = A_2^{AVs}, \qquad \mu_1^{Vs} = \mu_2^{AVs} \quad \text{and} \quad (Vs \leftrightarrow AVs), \tag{2.8}$$

and similarly for the Vt and AVt or the S and PS channels. These relations are very easily demonstrated by using the projections

$$C_z^{(\pm S)} = C_z^{PS} \pm (-1)^z C_z^S, \qquad C_z^{(\pm Vs)} = C_z^{Vs} \pm (-1)^z C_z^{AVs}, \qquad C_z^{(\pm Vt)} = C_z^{Vt} \pm (-1)^z C_z^{AVt}. \tag{2.9}$$

If the correlators $C_z^{(-\gamma)}$ vanish for all z then chiral symmetry is restored for the full spectrum of excitations.

2.3 Results

2.3.1 Thermal effects

The screening correlators at any non-zero temperature should be decomposed according to the symmetry group of the finite temperature slice. At sufficiently low temperature, however, one expects the Vt and Vs correlators to be nearly equal, and the symmetries of the $T = 0$ problem to be realized approximately. We investigated this by computing the ratios of the Vt and Vs correlators (normalized to be unity at $z = 0$). The statistical analysis was performed using a bootstrap, since the distribution of the ratio is not expected to be Gaussian [14]. The results below T_c are shown in Figure 2.2; the ratio is consistent with unity at all z. The normalization is the value of the ratio of the correlators at $z = 0$. In Figure 2.2 we have plotted C_0^{Vs} and C_0^{Vt} as a function of T. Below T_c the two are equal within statistical errors. The two facts taken together imply that the $T = 0$ symmetries remain good until rather close to T_c. Quite abruptly, just above T_c this higher symmetry is broken, and the symmetry of the finite temperature problem is obtained. Similar results are obtained for the AVs and AVt. In view of this, in most of our subsequent analysis, we will group the correlators below T_c into S, PS, V and AV. For $T \geq T_c$ we will continue to use the decomposition into S, PS, Vs, Vt, AVs and AVt.

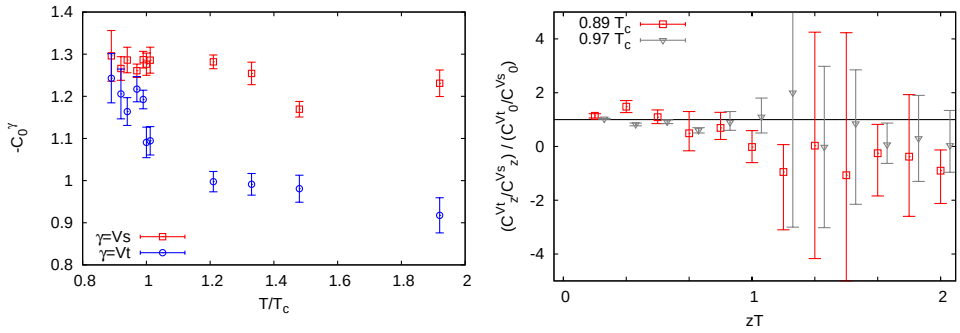

Figure 2.2: The panel on the left shows Vs and Vt correlators at $z = 0$ as a function of T/T_c. Note the abrupt lifting of the degeneracy at T_c. The panel on the right shows the ratio of the Vs and Vt correlators as a function of z, normalized by their values at $z = 0$. The data at $T = 0.97T_c$ is displaced slightly to the right for clarity.

To examine whether the correlation functions exhibit chiral symmetry restoration at any temperature, the most straightforward way is to plot $C_z^{(-\gamma)}$ at each T and ask whether it is consistent with zero at all z. In Figure 2.3 we show these quantities at two temperatures above T_c. From the correlator $C_s^{(-S)}$ we see that at $T = 1.48T_c$ the symmetry is clearly restored, whereas for $T = 1.012T_c$ the symmetry is broken. The

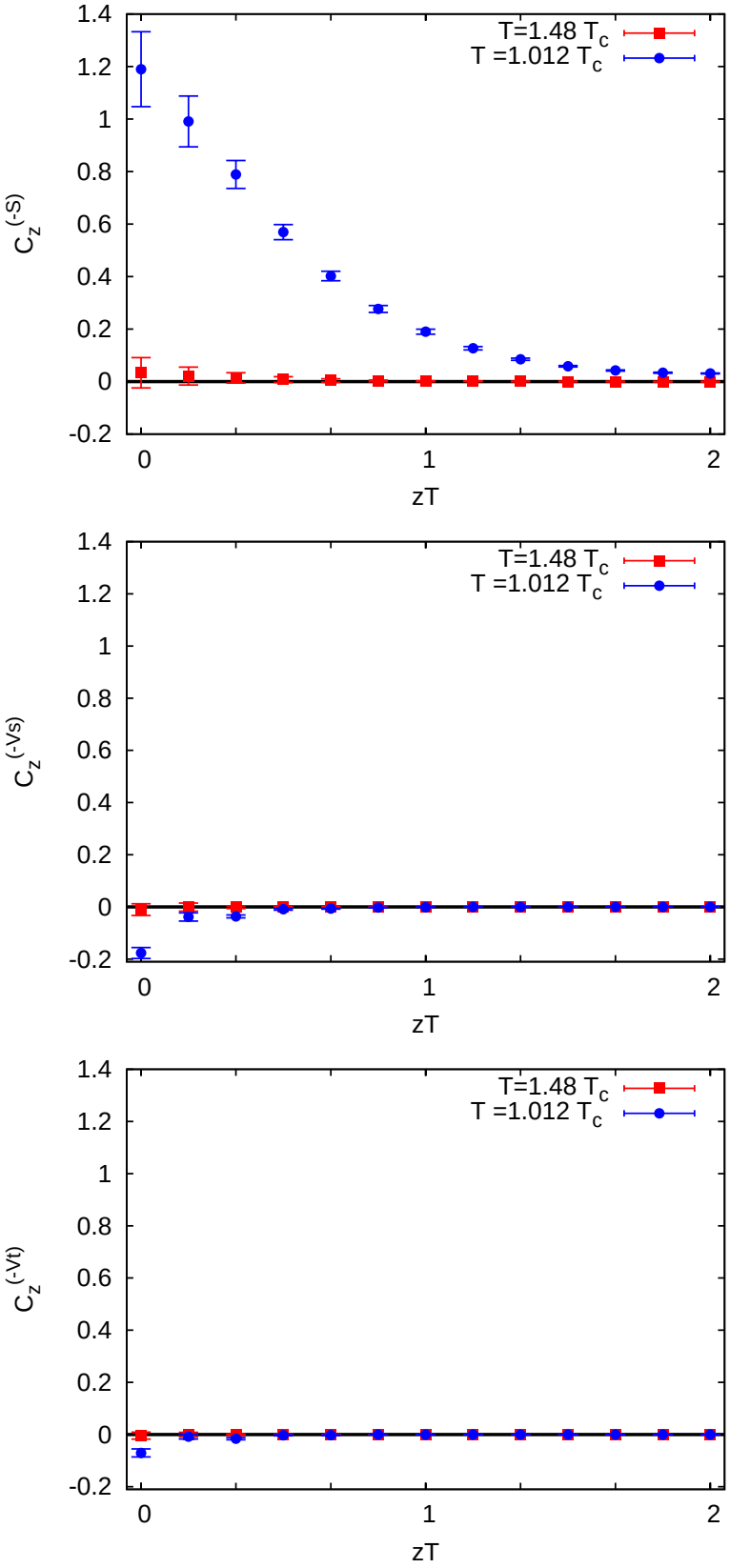

Figure 2.3: The chiral projections $C_z^{(-S)}$, $C_z^{(-Vs)}$ and $C_z^{(-Vt)}$ of eq. (2.9) at two temperatures as computed on lattices with $\zeta = 4$. The Vt channel shows chiral symmetry is close to being restored immediately above T_c.

correlator $C_z^{(-Vs)}$ is consistent with zero for $zT > 1$, but at distances less than $1/T$ there is clear chiral symmetry breaking close to T_c. The correlator $V_z^{(-Vt)}$ most nearly exhibits chiral symmetry restoration immediately above T_c, with only the value at $z = 0$ being significantly non-zero. At higher temperatures all the $C_z^{(-\gamma)}$ are consistent with zero at all z, thereby indicating chiral symmetry restoration.

T/T_c	χ^2_S	χ^2_{Vs}	χ^2_{Vt}	χ^2_{VB}	χ^2_{AVB}
1.92	0.52	0.42	0.86	16.2	16.2
1.48	9.62	1.33	0.77	10.2	11.5
1.33	13.5	2.07	1.13	14.1	11.7
1.21	441	27	15	19.8	8.8
1.012	1429	107	40	6.2	12.1
1.00	878	125	56	19.0	9.1
0.99	3009	214	114	10.1	17.2
0.97	3013	440	212	14.0	9.2
0.94	746	188	92	28	14.9
0.92	936	348	141	15.0	14.5
0.89	539	101	80	21.3	18.8

Table 2.1: This table lists the values of χ^2 at different temperature for tests of the hypotheses that various correlators vanish. The number of degrees of freedom in all these cases is 12, since there are 13 independent values of z on the lattices with $\zeta = 4$ with periodic boundary conditions. In order to rule out the hypothesis that a correlator vanishes at the 99% CL, the value of χ^2 should be more than 36.

In order to extend this analysis to all temperatures it is useful to introduce a less local quantity,

$$\chi^2_\gamma = \sum_{zz'} C_z^{(-\gamma)} \Sigma^{-1}_{zz'} C_{z'}^{(-\gamma)}, \tag{2.10}$$

where $\Sigma_{zz'}$ is the covariance matrix of the measurements of the correlator at different distances. This is a measure of the likelihood that the correlators at all z are consistent with zero, and hence that chiral symmetry is restored. Values of these variables are collected in Table 2.1. Note that χ^2_{Vt} shows a distinct change at T_c, although it is consistent with chiral symmetry restoration only at $T = 1.21T_c$. χ_{Vs} also shows a change at T_c, although it is less dramatic. From Figure 2.3 it would appear that the change in χ^2_{Vs} at T_c is due to the long distance ($z > 1/T$) correlation function becoming consistent with zero, whereas the short distance ($z \leq 1/T$) part disappears only at larger T. χ^2_S, on the other hand, does not seem to undergo any significant change at T_c and signals chiral symmetry restoration only at $T = 1.33T_c$. One sees the difference in behaviour in Figure 2.3; the S/PS correlators, unlike the V/AV, do not show any kind of effective long distance chiral symmetry restoration. This spatial

structure has not been noticed before, and could be worth further investigation in future.

The late restoration of chiral symmetry breaking can be understood from the fact that the non-vanishing quark mass provides explicit chiral symmetry breaking. In the chiral limit, there is a phase transition at T_c. In the high temperature phase there is, effectively, a single scale, T, so the screening mass $\mu \propto T$. However, when there is a non-vanishing bare quark mass, m, there is no phase transition at T_c but only a cross-over. In the absence of a phase transition, the screening-mass could depend on the m_π on a non-trivial way.

The projection of the local V and AV channel correlators on the B_1^{++} channel is expected to vanish. This was demonstrated in [16, 9] with lattice spacing $a = 1/(4T)$. Here we investigate the vanishing of these correlators at smaller lattice spacing using a correlated χ^2 definition similar to that above. In $\chi^2_{VB/AVB}$ the factors of $C_z^{-\gamma}$ in eq. (2.10) are replaced by the VB or AVB correlator. The results are collected in Table 2.1 and show that the VB and AVB correlators vanish.

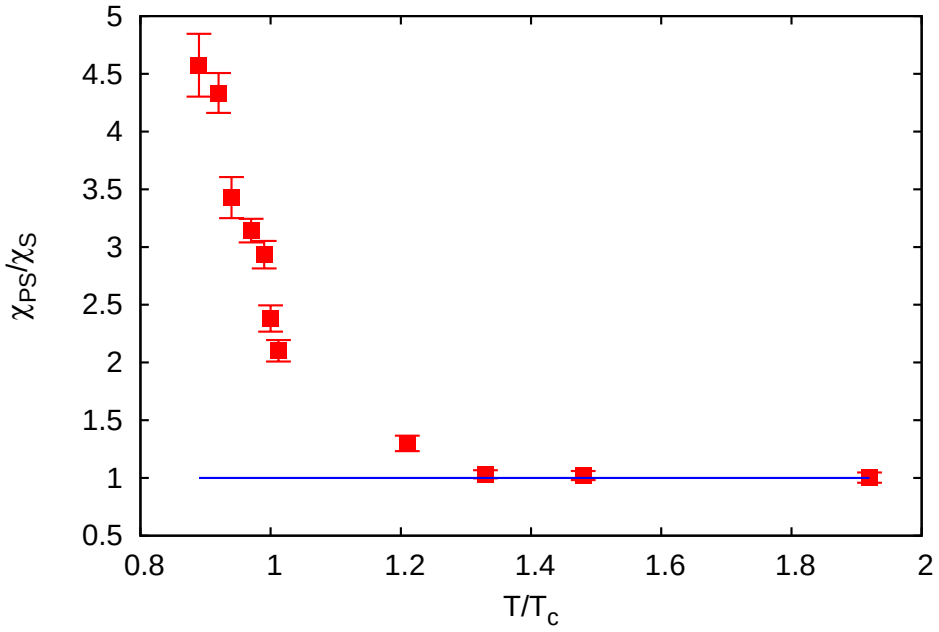

Figure 2.4: The ratio for susceptibilities of the pion to the scalar meson.

In Figure 2.4 we show the ratio of the PS and S susceptibilities (see eq. 2.2). As expected, they become equal at $T = 1.33T_c$, which is the point where the two correlators begin to satisfy eq. (2.7). At lower temperatures χ_{PS} is larger, essentially because μ_{PS} is smaller than μ_S.

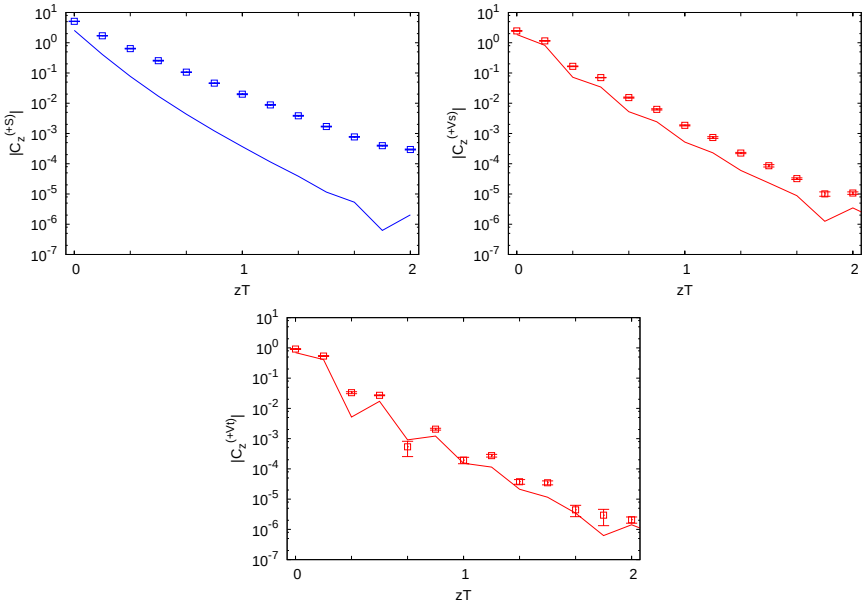

Figure 2.5: The correlators $C_z^{(+\gamma)}$ obtained at $T = 1.92T_c$ with bare quark mass $m/T = 0.1$. The lines show the result for free field theory computed with the same quark mass.

The other projection, $C_z^{(+\gamma)}$, is non-zero at all temperatures. At high enough temperature one might expect the whole correlation function to be described in a weak-coupling theory. In Figure 2.5 we show the correlators at $T = 1.92T_c$. One sees that the correlation function is far from the free field theory result, especially the correlator $C_z^{(+S)}$; indicating that even at this temperature the theory cannot be treated as weakly interacting. This is consistent with previous observations on the lattice [9, 10, 11].

2.3.2 Screening Masses

Figure 2.6 displays all four screening correlators at two temperatures, one each in the hadron and the plasma phase, at $T = 0.97T_c$ and $T = 1.92T_c$ respectively. The V/AV correlators show clear even-odd oscillations at both temperatures, whereas these staggered artifacts are less clear in the S/PS correlators. This has clear implications for the fits: the former always requires a doubled-parity fit of the form given in eq. (2.4), whereas for the latter a single parity form may suffice.

In Table 2.2 we show that this is indeed correct. The PS channel can be fitted to a single mass judging by the value of χ^2/dof, and the fitted value does not change significantly when a doubled-parity fit is performed. In fact, when a doubled-parity fit is attempted to the data, the mass of the parity partner is ill-determined. In the

V channel, on the other hand, the doubled-parity fit turns out to be indispensable. In the AV channel the behaviour is similar to that in the V. In the S channel a single mass suffices, although one needs a $(-1)^z$ factor multiplying the exponential to take care of staggered oscillations. Only at the highest temperature were we able to extract a second mass from the S/PS correlators. The table also shows that the fitted masses are reasonably stable against changes in the fit range in both the PS and V channels. We find similar results for all T.

Interestingly, although the covariance matrix is nearly singular (the smallest correlation coefficient being about 0.8), the difference between the parameters extracted using or neglecting the covariance matrix in the PS channel is marginal. The major difference seems to be that the value of χ^2 obtained when covariances are neglected are clearly too small for the usual statistical interpretation.

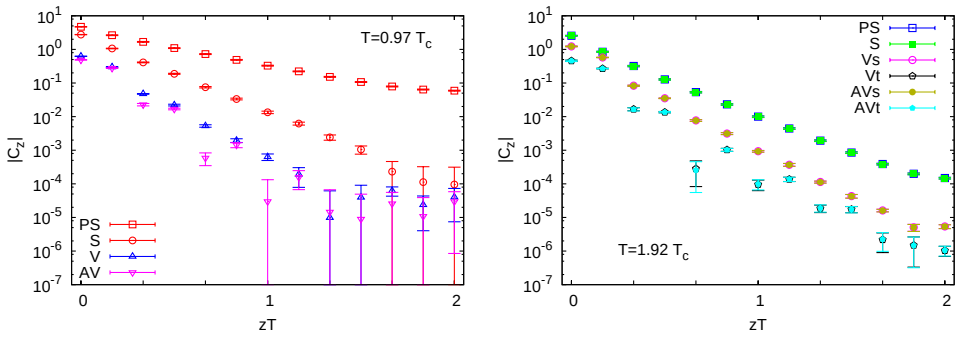

Figure 2.6: The correlators for all the mesons at representative temperatures in the two phases on the lattice with $\zeta = 4$. Note the absence of even-odd oscillations for the S and PS correlators.

In Figure 2.7 we demonstrate that the fitted masses agree with the local mass extracted from eq. (2.6). We draw attention to the fact that the local masses exhibit a very well developed plateau, indicating that the correlation functions of fixed parity can be well described by a single mass. The spatial structure of chiral symmetry restoration shown in Figure 2.3 is visible also in the local masses at high temperature.

In Table 2.3 we collect the results for the fitted masses at all temperatures. We checked in all cases that the local masses for $z > 1/T$ were compatible with these fits. For the V/AV correlators we also checked that if the fits were restricted to $z \leq 1/T$ the fit results were generally different. Wherever doubled-parity fits are available, one can look for chiral symmetry restoration by checking whether or not the relations of eq. (2.8) are satisfied. Consistent with previous analysis, we find that this happens only for $T \geq 1.33T_c$ in the S/PS channels. Surprisingly, the equalities of eq. (2.8) hold in the V/AV channels, within statistical errors, from just above T_c.

	PS				V		
	Uncorrelated single parity fit						
Range	3–11	4–11	5–11		4–9	4–10	
A	3.61(7)	3.59(6)	3.59(6)				
m	0.401(2)	0.400(2)	0.400(2)				
χ^2/dof	0.24/7	0.01/6	0.01/5				
	Correlated single parity fit						
A	3.64(18)	3.59(16)	3.58(16)		0.053(4)	0.053(3)	
m	0.401(3)	0.400(3)	0.400(2)		0.484(7)	0.480(8)	
χ^2/dof	11.0/7	2.1/6	1.9/5		9.5/4	9.8/5	
	Correlated doubled-parity fit						
		4–11	5–11	6–11	2–11	1–10	3–9
A_1		3.59(14)	3.59(12)	3.58(11)	-0.67(4)	-0.70(3)	-0.55(5)
μ_1		0.400(2)	0.400(2)	0.400(2)	1.18(3)	1.20(3)	1.14(3)
A_2		0.02(6)	0.04(12)	3.1(*)	0.38(6)	0.49(4)	1.4(4)
μ_2		0.9(*)	0.9(*)	1.5(*)	1.62(8)	1.71(5)	1.98(11)
χ^2/dof		1.60/4	1.58/3	1.28/2	6.55/6	6.56/6	2.20/3

Table 2.2: Fits to PS and V Correlators at $T = 0.97T_c$ on a lattice with $\zeta = 4$. An asterisk on a number indicates that the fit value is not determined reliably.

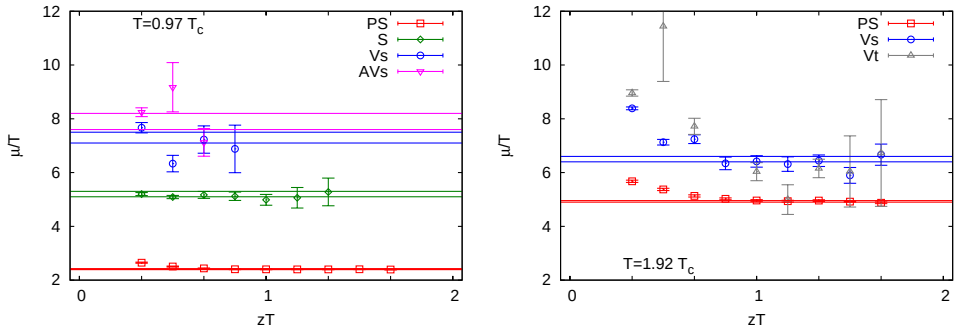

Figure 2.7: The extracted local masses for the mesons at representative temperatures in the two phases on a lattice with $\zeta = 4$. In the high temperature phase, where chiral symmetry is restored, only the PS, Vs and Vt masses are shown since the S, AVs and AVt exactly coincide.

In Figure 2.8 we plot the lowest screening mass in each channel as a function of T/T_c. Above T_c we could plot three channels. To avoid clutter we plotted only the S/PS and Vt/AVt channels. As one sees in Table 2.3, the lowest Vs/AVs masses are slightly larger, but consistent with Vt/AVt at the 2-σ level. All the features discussed are clearly visible here. Also visible is the fact that μ_{PS}/T increases monotonically with T whereas μ_S/T dips near T_c. Note also that μ_{Vt}/T may approach its ideal gas value from above, becoming consistent with the limit already at $T \simeq 2T_c$. How-

T/T_c		PS	S	Vs	AVs	Vt	AVt
1.92	μ_1/T	4.93(3)	5.1(6)	6.5(1)	12.6(4)	9.4(3)	6.1(2)
	μ_2/T	5.1(7)	4.93(3)	12.8(4)	6.5(1)	6.1(2)	9.3(4)
χ^2		15.8	16	9.2	9.3	7.4	7.2
1.48	μ_1/T	4.44(4)	17(1)	6.8(1)	5.8(4)	8.9(4)	6.6(4)
	μ_2/T	—	4.5(4)	5.6(4)	6.8(1)	6.6(4)	8.7(4)
χ^2		8.1	1.8	5.2	5.3	9.6	9.2
1.33	μ_1/T	4.15(2)	7.0(7)	6.7(2)	9.6(6)	8.7(3)	6.8(5)
	μ_2/T	—	4.22(4)	8.7(5)	6.8(2)	6.6(6)	8.9(4)
χ^2		31.8	9.2	11.4	11.3	6.0	7.7
1.21	μ_1/T	3.31(7)	—	6.5(2)	9.4(8)	8.1(4)	6.1(8)
	μ_2/T	—	3.91(5)	15.0(6)	6.8(2)	6.8(8)	9.1(4)
χ^2		18.2	6.3	5.4	12.5	2.2	3.8
1.012	μ_1/T	2.65(4)	23(3)	6.9(3)	4.5(9)	6.4(5)	5.7(7)
	μ_2/T	—	4.3(1)	4(2)	8.8(4)	5(1)	5.3(6)
χ^2		21.2	7.4	5.2	2.1	1.0	2.8
1.00	μ_1/T	2.54(3)	—	5.9(3)	5.2(6)	7.9(4)	13(2)
	μ_2/T	—	4.6(2)	9.8(9)	8.6(4)	—	11.6(5)
χ^2		11.9	7.0	6.1	4.6	3.2	7.8
		PS	S	V	AV		
0.99	μ_1/T	2.47(2)	5(1)	5.5(2)	6.4(5)		
	μ_2/T	—	4.6(2)	12(1)	6.0(4)		
χ^2		8.4	2.6	6.3	4.3		
0.97	μ_1/T	2.41(2)	4(1)	7.0(2)	7.0(3)		
	μ_2/T	—	5.2(1)	11(1)	7.7(3)		
χ^2		11.0	3.6	6.5	1.7		
0.94	μ_1/T	2.35(2)	4(2)	5.9(2)	4(1)		
	μ_2/T	—	5.2(2)	—	14.4(3)		
χ^2		15.3	3.2	2.8	2.4		
0.92	μ_1/T	2.31(2)	5(1)	7.3(3)	7.3(7)		
	μ_2/T	—	5.7(2)	—	10.0(7)		
χ^2		7.5	1.3	6.5	7.6		
0.89	μ_1/T	2.27(2)	—	5.5(6)	7(1)		
	μ_2/T	—	4.9(4)	7(2)	5(1)		
χ^2		5.6	7.7	4.3	12.2		

Table 2.3: Screening masses at different temperatures. The fit range was z/a=3–11 except for the S/PS at $1.92T_c$, where the fit range was z/a=4–11 (the larger range gave very large χ^2 without appreciably changing the best fit values). Also note that except at $1.92T_c$, the PS fit was done with a single-parity fit form, and therefore has two more degrees of freedom than the other channels. A dash indicates that some mass could not be obtained because staggered oscillations were not visible. At temperatures below T_c the analysis was performed on the V/AV channels.

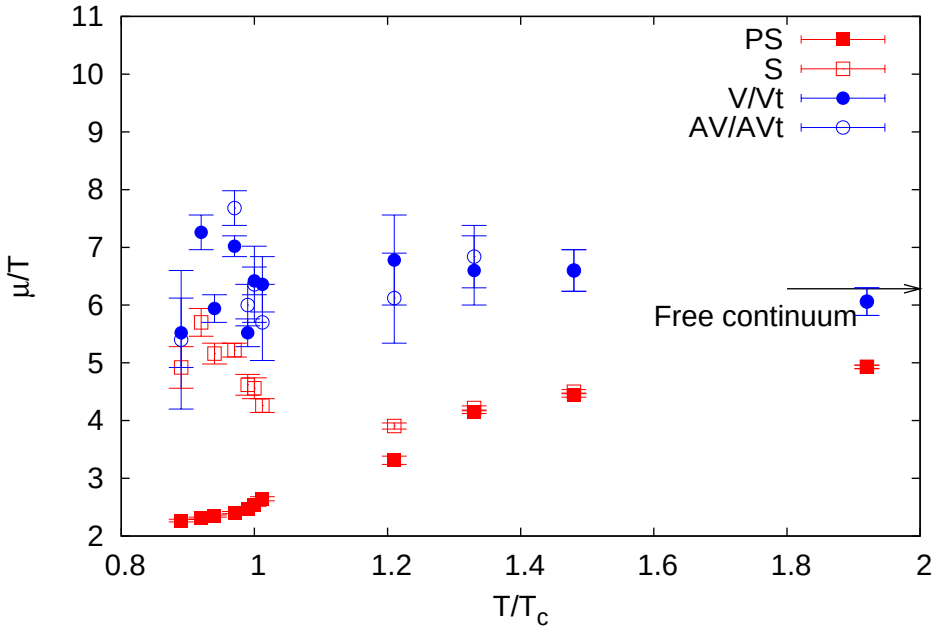

Figure 2.8: Screening masses as functions of T/T_c. Below T_c the S, PS, V and AV channels are shown. At T_c and above the S, PS, Vt and AVt are shown. The free continuum value of 2π is indicated with an arrow.

ever μ_S/T remains about 20% below this limit even at the highest temperature we explored. We shall return to this point later when we discuss the continuum limit.

2.3.3 The role of explicit chiral symmetry breaking

In free field theory one has no pion and the explicit chiral symmetry breaking scale is the quark mass. In this case one has

$$\frac{\mu}{T} = 2\sqrt{\pi^2 + \left(\frac{m}{T}\right)^2} \simeq 2\pi \left[1 + \frac{1}{2}\left(\frac{m}{\pi T}\right)^2\right]. \tag{2.11}$$

Substituting the bare quark mass into this expression, it can be seen that the effect is of the order of a few parts in 10^5, and hence negligible. However, it turns out that in weak-coupling theory one has to insert in the above equation the thermal mass of the quark [18]. Since this is $gT/\sqrt{3}$, and g is large near T_c [19], the effect can be significant. Of course, when g is large, the weak-coupling theory is unlikely to be quantitatively useful, and should be taken only as an indication that one must explore the quark mass dependence of the chiral symmetry breaking seen in the screening masses.

Changing the quark mass involves in principle a completely new set of computa-

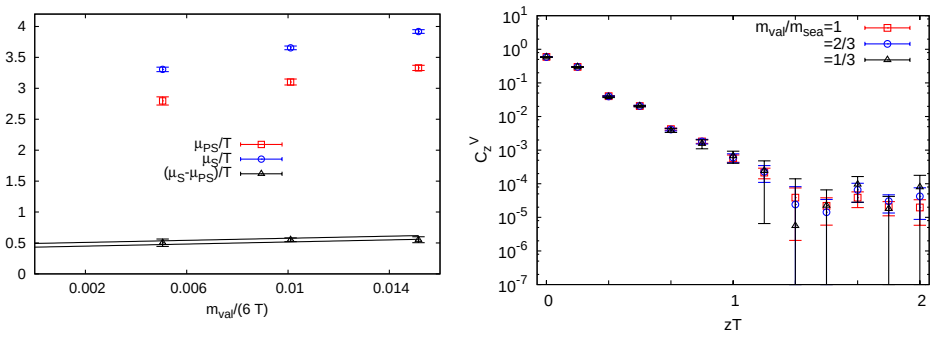

Figure 2.9: The valence quark mass dependence of various quantities at $T = 1.21T_c$ when the bare sea quark mass is held fixed at the value $m/T_c = 0.1$ (corresponding to $m_\pi \simeq 230$ MeV). The screening masses in the S/PS sector depend significantly on the valence quark mass, whereas the V sector screening correlators are insensitive.

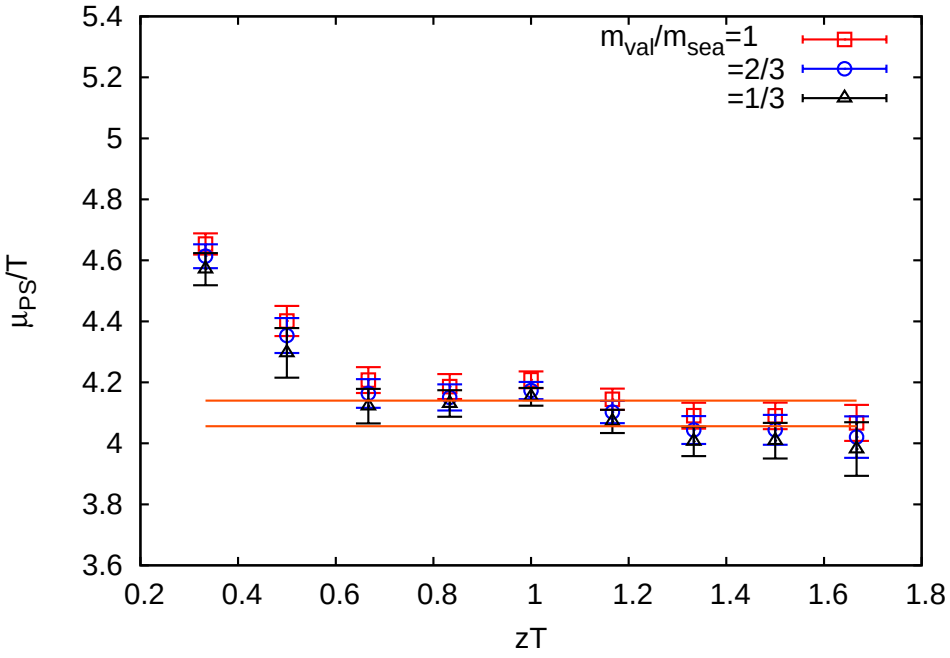

Figure 2.10: Local masses in the PS channel for different valence quark masses at $T = 1.33T_c$ with $\zeta = 4$. The horizontal lines are the 1-sigma bounds from the fit to the correlator for $m_{val} = m_{sea}$.

tions. However, we have changed the valence quark mass (m_{val}) without changing the sea quark mass (m_{sea}) on the same configurations. We repeated our analysis above T_c with m_{val} chosen to be 2/3 and 1/3 of m_{sea}. Sample results are shown in Figure 2.9.

We find that a change in the valence quark mass has insignificant effect in the V/AV channels (see, for example, the second panel of Figure 2.9). However, there are statistically significant changes in the S/PS sector. Both the S and PS screening mass increase with m_{val}. The difference also increases, although the limiting value for $m_{val} = 0$ is finite. We find that

$$\left.\frac{\mu_S - \mu_{PS}}{T}\right|_{T/T_c=1.21} = 0.46 \pm 0.03 \qquad (\text{for } m_{sea}/T_c = 0.1,\ m_{val} = 0). \tag{2.12}$$

It is possible that decreasing m_{sea} in a future computation can lower this mass difference further. We note that μ_{PS}/T and μ_S/T both drop as the quark mass changes, and move further away from the weak-coupling expectation.

In fact, the dependence of correlation functions on the bare quark mass can be deeper than what was discussed above. We illustrate this in Figure 2.10, where local masses in the PS channel are shown for several values of m_{val}. It seems that with decreasing m_{val} the plateau in the local masses becomes less well developed; for the smallest m_{val}, in fact, a slight slope is visible.

2.3.4 The effect of finite volume

ζ		PS	S	V	AV
4/3	μ_1	2.45(4)	—	8.0(2)	4.3(6)
	μ_2	—	5.0(3)	—	7.7(6)
2	μ_1	2.41(2)	—	6.8(3)	13.1(7)
	μ_2	—	5.5(2)	14.7(5)	9.2(5)
3	μ_1	2.44(3)	6(1)	6.5(2)	8.0(3)
	μ_2	—	5.3(2)	6.4(8)	9.1(3)
4	μ_1	2.35(2)	4(2)	6.4(3)	7.6(3)
	μ_2	—	5.2(2)	29(4)	9.4(2)
5	μ_1	2.39(2)	4.2(-)	6.6(4)	8.1(5)
	μ_2	—	5.5(4)	9(1)	8.6(4)

Table 2.4: Screening mass estimates at $T = 0.94T_c$ at fixed $a = 1/(6T)$ with changing spatial volume $(\zeta/T)^3$.

Finite volume effects in the high temperature phase of QCD have been explored

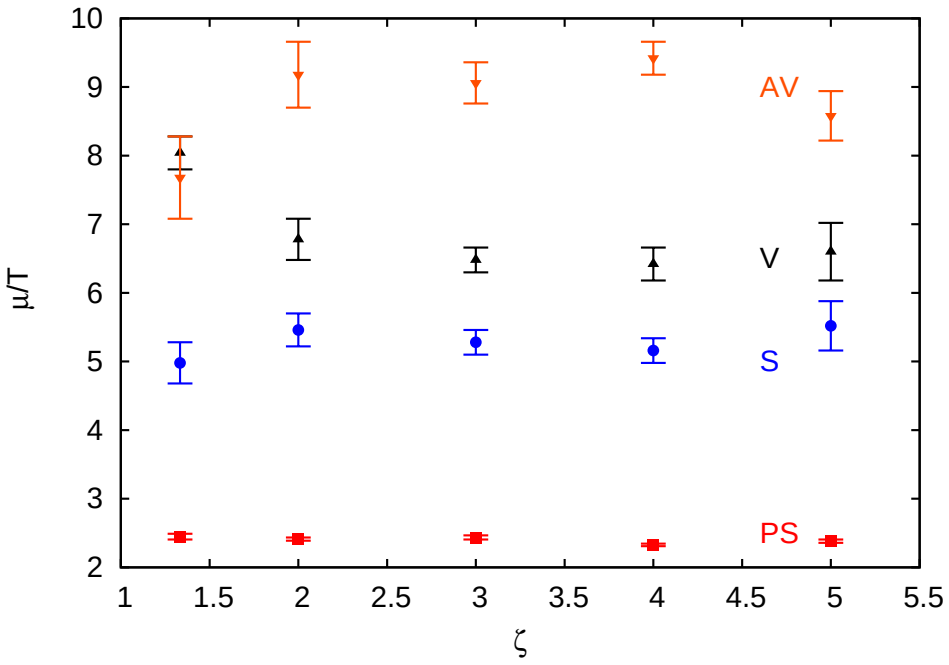

Figure 2.11: Screening masses in various channels as a function of ζ at $T = 0.94T_c$. Note that there is nothing special about the S channel masses.

earlier [9] and are by now well understood. These effects are under control as long as μ_{PS} is large compared to the inverse size of the smallest lattice dimension, i.e., T. Since we find $\mu_{PS}/T > 2.5$ in the high temperature phase, we expect that finite volume effects are under control for $T > T_c$.

In this work, we have studied these effects below T_c, on lattices with $4/3 \leq \zeta \leq 5$ at $T = 0.94T_c$. As shown in Table 2.4 and Figure 2.11, finite volume effects are invisible within statistical errors. Again, since $\mu_{PS}/T \simeq 2.3$, this may not seem unexpected. While such studies can have some bearing on decay widths at finite temperature, much larger lattices and smaller quark masses and lattice spacings may be required for those. For example, the scalar under study cannot decay into two pions, and must have at least three pions in the final state. This is ruled out kinematically here.

However, since $\mu_S/\mu_{PS} \simeq 2.2$, one must ask whether the long-distance behaviour of the S correlator is determined by a single scalar exchange or multi-particle exchanges (this is the finite temperature analogue of particle decays, and we shall save space by using the word decay). In the continuum theory, this non-isosinglet scalar cannot decay into two pions. From this point of view, since $\mu_S/\mu_{PS} \simeq 2.2 < 3$, one could expect that the scalar does not decay. However, with staggered quarks on a lattice, there are spurious two pion states (taste multiplets) through which the scalar current could be correlated [20]. The featureless behaviour of the volume dependence of the

screening masses is indicative of a stable state.

2.3.5 The continuum limit

T/T_c	$a = 1/(4T)$		$a = 1/(6T)$	
	S/PS	Vt/AVt	S/PS	Vt/AVt
1.5	3.67 ± 0.02	5.44 ± 0.08	4.44 ± 0.04	6.6 ± 0.4
2.0	4.08 ± 0.01	5.72 ± 0.04	4.93 ± 0.03	6.1 ± 0.2

Table 2.5: The lattice spacing dependence of μ/T in various quantum number channels. The temperature scale is rounded off. Data for $a = 1/(4T)$ is taken from [9].

In Table 2.5 we extract the values of the screening masses in units of temperature, μ/T for two different temperatures in the chirally symmetric phase, at two different lattice spacings. From two pieces of data in each case it is hard to construct a continuum extrapolation. However, we can test whether the extrapolation is consistent with the expectation $\mu \simeq 2\pi T$ by attempting a fit to the form

$$\frac{\mu}{T}\Big|_{N_t} = 2\pi + \frac{s}{N_t^2}. \tag{2.13}$$

It is possible to get reasonable fits in the V/AV channel, yielding

$$s = \begin{cases} -13 \pm 2 & (T = 1.5T_c) \\ -9.0 \pm 0.2 & (T = 2T_c) \end{cases} \tag{2.14}$$

This is consistent with previous results. However, in the S/PS case this procedure fails to yield the expected result; the extrapolated screening length remains below the ideal gas value. One cannot rule out the possibility that the weak-coupling result emerges at even smaller lattice spacings.

We note however, that the screening of meson-like correlations in the weak coupling theory occurs, not through the exchange of a single particle, but through multiparticle exchange. As a result, the zero-momentum correlator is not expected to be strictly exponential, but to have some curvature. Such a curvature was actually seen in computations in the quenched theory using staggered [21] and Wilson [8] quarks using much smaller lattice spacings. An easily observed feature of such a curvature is that local masses do not show a plateau, but change continuously with z. Such behaviour was neither seen here (see Figure 2.7), nor with p4 improved quarks at the

same renormalized quark mass [10]. However, as pointed out in Section 2.3.3, when the quark mass is lowered such a feature could emerge.

2.4 Summary

We studied screening correlation functions and screening masses of meson-like probes of strongly interacting matter, both in the low temperature hadron and high temperature plasma phases. We used configurations described in [14]; these were generated using two flavours of dynamical staggered quarks with masses tuned to give $m_\pi \simeq 230$ MeV. Most of the results come from lattice spacing $a = 1/(6T)$, although we have attempted to check assumptions about the continuum limit using earlier measurements with the same renormalized quark mass and lattice spacing $a = 1/(4T)$. We have explicitly checked for finite volume effects, and found that these are negligible when we take the aspect ratio $\zeta = 4$.

We checked that the correlators at $T < T_c$ effectively have the symmetries of the $T = 0$ transfer matrix, and that there is a fairly abrupt transition at T_c to the symmetries of the screening transfer matrix (see Figure 2.2). Although the QCD cross over occurs at T_c, we found a lack of parity doubling in the spectrum of screening masses up to a temperature of $1.33T_c$ (see, for example, Figure 2.4 and Table 2.1). Interestingly, there turns out to be a lot of structure in this apparent breaking of chiral symmetry above T_c. The V/AV correlators are equal to each other at distances $z > 1/T$, and the chiral symmetry breaking in this sector is entirely a short distance effect (see Figure 2.3). In the S/PS sector the non-degeneracy of the correlators persists into the long distance regime.

Non-degeneracy of the S/PS correlators could also be due to $U_A(1)$ symmetry breaking. This is suspected to persist well into the high temperature plasma phase [22]. We tested what happens to the S/PS difference as the valence quark mass is changed (see Figure 2.9). Our results imply that other physics effects can be disentangled from the explicit symmetry breaking effect due to finite quark mass only through computations with smaller quark masses.

We made the first study of hadron decays at finite temperature (below T_c) through a systematic exploration of the volume dependence of screening masses. We found no significant volume dependence (see, for example, Table 2.4 and Figure 2.11), indicating the stability of the scalar. As we discussed already, this study needs to be carried out with smaller quark masses so that $\mu_S/\mu_{PS} > 3$, or at smaller lattice spacings, so that taste violations are reduced.

We combined the analysis of this paper with data from an earlier source [9] in

which the same renormalized quark masses were used to study screening at a coarser lattice spacing, $a = 1/(4T)$ to explore the continuum limit. Being restricted to only two values of the lattice spacing at each T, we ask whether the continuum limit of screening masses is compatible with the ideal gas expectation, $2\pi T$, in the high-temperature phase. We find that it is, in the V/AV channels, but not in the S/PS channels.

If the high temperature phase is deconfined, then correlations of static currents with meson quantum numbers must be mediated by the exchange of a quark anti-quark pair. The most straightforward signal of this is that the local masses do not show a well-developed plateau. In most of our studies we did not see this. Only in a study with rather small valence quark masses did we see a signal of such behaviour (see Figure 2.10). Studies with lower sea quark masses in the future will be needed to resolve the question of deconfinement above T_c in QCD with physical quark masses.

References

[1] C. DeTar and J. B. Kogut *Phys. Rev.* D36, 2828 (1987).

[2] M. LeBellac *Thermal Field Theory* Cambridge University Press, Cambridge, 2000

[3] O. Kaczmarek **PoS CPOD**07 (2007) 043.

[4] K. Kajantie et. al *Phys. Rev. Lett* 79 (1997) 3130

[5] S. Datta and S. Gupta *Nucl. Phys.* B 534 (1998) 392

[6] K. D. Born et. al. (MT_c Collaboration) *Phys. Rev. Lett.* 67 (1991) 302.

[7] C. Bernard et. al., (MILC Collaboration) *Phys. Rev. Lett.* 68 (1992) 2125;
E. Laermann and P. Schmidt *Eur. J. Phys.* C 20 (2001) 541.

[8] S. Wissel **PoS LAT**2005 164;
E. Laermann **PoS LAT**2008 (2008) 193

[9] R. V. Gavai, S. Gupta and P. Majumdar *Phys. Rev.* D 65 (2002) 054506.

[10] M. Cheng et. al. *Eur. J. Phys.* C71 1564,2011

[11] R. V. Gavai, S. Gupta and R. Lacaze *Phys. Rev.* D72 (2008) 014502

[12] D. Banerjee et.al. **PoS LAT**2010 (2010) 168

[13] D. Banerjee, R. V. Gavai, S. Gupta *Phys. Rev.* D83, 074510 (2011)

[14] R. V. Gavai and S. Gupta *Phys. Rev.* D78 (2008) 114503

[15] S. Gupta *Phys. Rev.* D 60 (1999) 094505

[16] R. V. Gavai and S. Gupta *Phys. Rev. Lett.* 83 (1999) 3784

[17] S. Gupta *Phys. Lett.* B 288 (1992) 171

[18] M. Vespäläinen, *JHEP* 0703 (2007) 022;
W. M. Alberico et. al., *Nucl. Phys.* A 792 (2007) 152

[19] S. Gupta *Phys. Rev.* D64 (2001) 034507

[20] S. Prelovsek *Phys. Rev.* D 73 (2006) 014506;
C. Bernard et. al. (MILC Collaboration) *Phys. Rev.* D 76 (2007) 094504

[21] R. V. Gavai and S. Gupta *Phys. Rev.* D 67 (2003) 034501

[22] R. V. Gavai, S. Gupta and R. Lacaze *Phys. Rev.* D 65 (2002) 094504

Chapter 3

Diffusion constant of heavy quarks in the gluon plasma

3.1 Introduction

The mass of both the charm and the bottom quarks are much heavier than the temperatures attained in RHIC and in LHC experiments. This leads to the expectation that these quarks are produced largely in pre-equilibriated state of the collision. This provides an important probe for studying the early stages of the collision. Since the energy loss mechanism for the heavy quarks is expected to be different from that of the light quarks based on perturbative arguments, a comparative study of the energy losses of heavy and light quark jets could provide a crucial insight into the mechanism of energy loss of jets in quark gluon plasma.

For light quark jets, gluon radiation ("bremsstrahlung") is expected to be the leading mechanism for energy loss in medium [1]. But gluon bremsstrahlung is suppressed for jets of heavy quarks [2], and collisional energy loss is expected to be the dominant mechanism for thermalization of heavy quark jets. Since collision with a thermal quark does not change the energy of a heavy quark substantially, one would expect that the thermalization time of the heavy quarks is much larger than that of the light quarks. Since most of the elliptic flow is developed early, the elliptic flow velocity, v_2, of the hadrons with heavy quarks can be expected to be much less than that of the light hadrons.

Interesting predictions follow from these simple, weak coupling-based intuitions, which can be checked in the heavy ion collision experiments. One can expect a mass ordering of both flow and the nuclear suppression factor, R_{AA}: $v_2^h \gg v_2^D \gg v_2^B$ and $R_{AA}^h \ll R_{AA}^D \ll R_{AA}^B$; here h, D, B refer to the light hadrons, mesons of the

D family (one charm and one light quark) and those in the B family (one bottom and one light quark). Experimentally, on the other hand, it was found that the open charm mesons show a large elliptic flow, $v_2^D \sim v_2^h$, and a strong nuclear suppression, $R_{AA}^D \sim R_{AA}^h$ [3].

Since the parton densities of the medium created in experiments like RHIC and LHC are very large, and the momentum of the heavy quark, being much larger than the temperature, is changed very little in a single collision, successive collisions can be treated as uncorrelated and a Langevin description of the motion of the heavy quark in the medium has been proposed [4, 5]. Using this formalism, the energy loss can be expressed in terms of the diffusion coefficient of the heavy quark in the medium. The diffusion coefficient has been calculated in perturbation theory [4, 5]. It has been found, however, that the perturbative value is too low to explain the charm quark flow seen in RHIC [5]. A nonperturbative estimate of the diffusion coefficient will be necessary for the applicability of the Langevin formalism to the understanding of the heavy quark flow.

In the infinite quark mass limit, a nonperturbative definition of the diffusion coefficient was given in Refs. [6, 7]. In this limit, the formalism of Ref. [5] reduces to evaluation of retarded correlator of electric fields connected by Wilson lines [6]. In Ref. [6], this formalism was used to calculate the diffusion coefficient for the $\mathcal{N} = 4$, SU($N_c \to \infty$) gauge theory, using the AdS/CFT correspondence. The results of this calculation indicate a considerably large diffusion coefficient at moderately high temperatures. On the other hand, a leading order perturbative evaluation led to a negative value for the diffusion coefficient at such temperatures [7, 8].

Lattice QCD provides the only way of doing reliable calculations in the quark-gluon plasma at moderately high temperatures, where perturbation theory is known to be unreliable. The formalism outlined in Ref. [7] can be adapted to numerical calculation on the lattice. As we outline in the next section, this involves the calculation of Matsubara correlators of color electric field operators, and extracting the low frequency part of the spectral function from it. The extraction of the spectral function from the Matsubara correlator is, however, a very difficult problem numerically. A direct inversion of the correlator is an ill-posed problem. In some cases, Bayesian analysis techniques have been used, with varying degrees of success. Here we will assume a form of the spectral function, which turns the problem to a standard χ^2-fitting problem.

3.2 Formalism

To understand why the motion of a quark much heavier than the system temperature can be described in the Langevin formalism, we note that if the kinetic energy is $\sim T$, then the momentum, $\sim \sqrt{MT}$, is not changed substantially in individual collisions with thermal gluons and quarks, which can only lead to a momentum transfer $\sim T$. Therefore, the force on the heavy quark can be written as the sum of a drag term and a term of "white noise" form, corresponding to uncorrelated random collisions:

$$\frac{dp_i}{dt} \;=\; -\eta_D p_i \;+\; \xi_i(t), \qquad \langle \xi_i(t)\xi_j(t')\rangle \;=\; \kappa\;\delta_{ij}\;\delta(t-t'). \tag{3.1}$$

From Eq. (3.1) the momentum diffusion coefficient, κ, can be obtained from the correlation of the force term:

$$\kappa \;=\; \frac{1}{3}\int_{-\infty}^{\infty} dt\;\sum_i \langle \xi_i(t)\xi_i(0)\rangle. \tag{3.2}$$

The drag coefficient, η_D, can be connected to the diffusion coefficient using standard fluctuation-dissipation relations [9]:

$$\eta_D = \frac{\kappa}{2MT}. \tag{3.3}$$

Here M is the heavy quark mass. To have a field theoretic generalization of Eq. (3.2), one introduces [7] the conserved current for the heavy quark number density, $J^\mu(\vec{x},t) \;=\; \bar{\psi}(\vec{x},t)\gamma^\mu\psi(\vec{x},t)$, where ψ is the heavy quark field operator. The force acting on the heavy quark is given by $M\;dJ^i/dt$ and so, Eq. (3.2) generalizes to

$$\kappa \;=\; \frac{1}{3}\;\lim_{\omega\to 0}\left[\lim_{M\to\infty}\;\frac{M^2}{T\;\chi^{00}}\;\int_{-\infty}^{\infty} dt\;e^{i\omega(t-t')}\;\int d^3x\;\left\langle \frac{1}{2}\left\{\frac{dJ^i(\vec{x},t)}{dt}\;,\;\frac{dJ^i(\vec{0},t')}{dt'}\right\}\right\rangle\right]. \tag{3.4}$$

where χ^{00} is the quark number susceptibility and is related to the number density of the heavy quark through

$$\int d^3x \langle J^0(\vec{x},t)\;J^0(\vec{0},t)\rangle \;=\; T\chi^{00}. \tag{3.5}$$

The force term and the number density term are :

$$\begin{aligned} M\frac{dJ^i}{dt} \;&=\; \left\{\phi^\dagger E^i\phi \;-\; \theta^\dagger E^i\theta\right\}, \\ J^0 \;&=\; \phi^\dagger\phi \;+\; \theta^\dagger\theta, \end{aligned} \tag{3.6}$$

where ϕ and θ are the two-component heavy quark and antiquark field operators, respectively, and E^i is the color electric field. In the leading order in an expansion in $1/M$, only electric field contributes to the force term.

With the substitution of Eq. (3.6), the real time correlator in Eq. (3.4) can be calculated as analytical continuation of the Matsubara correlator,

$$G_E(\tau) \;=\; -\frac{1}{3}\sum_{i=1}^{3}\lim_{M\to\infty}\frac{1}{T\chi^{00}}\int d^3x\,\left\langle\left\{\phi^\dagger E^i\phi \;-\; \theta^\dagger E^i\theta\right\}(\tau,\vec{x})\;\left\{\phi^\dagger E^i\phi \;-\; \theta^\dagger E^i\theta\right\}(0,\vec{0})\right\rangle. \tag{3.7}$$

The spectral function, $\rho(\omega)$ is related to $G_E(\tau)$ by the integral equation [9]

$$G_E(\tau) \;=\; \int_0^\infty \frac{d\omega}{\pi}\;\rho(\omega)\;\frac{\cosh\omega(\tau-\frac{1}{2T})}{\sinh\frac{\omega}{2T}}. \tag{3.8}$$

The momentum diffusion coefficient, Eq. (3.4), is given by

$$\kappa \;=\; \lim_{\omega\to 0}\;\frac{2T}{\omega}\;\rho(\omega). \tag{3.9}$$

In this limit, the expression (3.7) simplifies considerably. The heavy quark correlators give a static color field, besides an exponential suppression factor: e.g., $\langle\theta_a(\tau,\vec{x})\theta_b^\dagger(0,\vec{0})\rangle = \delta^3(\vec{x})\;U_{ab}(\tau,0)\;\exp(-M\tau)$, where $U_{ab}(\tau,0)$ is the timelike gauge connection, the delta function comes because of the static nature of the heavy quark, and there is an exponential suppression factor with the heavy quark mass. Since a similar factor comes also from χ^{00}, the exponents cancel and, for the infinitely heavy quarks, one is left with the rather simple expression

$$G_E(\tau) \;=\; -\frac{1}{3L}\;\sum_{i=1}^{3}\;\left\langle\mathrm{Re\ Tr}\;\left[U(\beta,\tau)\;E_i(\tau,\vec{0})\;U(\tau,0)\;E_i(0,\vec{0})\right]\right\rangle, \tag{3.10}$$

where $L = \mathrm{Tr}U(\beta,0)$ is the Polyakov loop. Once again, intuitively it is easy to understand Eq. (3.10): for the infinitely heavy quarks, all that the force-force correlator gives is the correlator of color electric fields, connected through Wilson lines, and normalized by the Polyakov loop.

The extraction of $\rho(\omega)$ from $G_E(\tau)$ using Eq. (3.8) is formidable because of the small extent of the Euclidean time τ in the plasma phase. With little data, it is difficult to isolate the contributions of the different ω regimes in $G_E(\tau)$. Since we in general have only $O(10)$ data points where $G_E(\tau)$ is measured, the problem of extraction of $\rho(\omega)$ becomes a completely ill-posed problem without any further input.

For some problems, a Bayesian analysis, with prior information in the form of

perturbative results, have been useful. In general, though, a stable application of these techniques require both a very large number of points in the τ direction and very accurate data for $G_E(\tau)$. Moreover such methods (the Maximum Entropy Method is one example) are often sensitive to the default model which is input from physical intuition. For the kind of extended objects we are considering, wrapping the lattice in the Euclidean time direction further decreases the number of independent data. As we will discuss, typically we only reach 2-3 % accuracy with our lattices, that have $\lesssim 20$ points in the time direction.

Parametrizing $\rho(\omega)$ in terms of a small number of parameters, therefore, seems to be the simplest way to extract the low-ω behaviour of the spectral function. In our case, the leading order perturbative form of the spectral function is $\sim a_3\omega^3$. Also in the $\omega \to 0$ regime, we need $\rho(\omega) \sim \kappa\omega$ to get a physical value of the diffusion constant using Eq. (3.9). The calculation of Ref. [6] get $\rho(\omega) \sim c\omega$ for the $\mathcal{N} = 4$ theory. Motivated by these, we postulated a simple form for the spectral function at small ω, $\rho(\omega) \sim a_1\omega + a_3\omega^3$. Of course, at large ω this form is not valid, and a complicated form, that takes into account the effect of lattice Brillouin zones should be considered. We restrict ourselves to the large distance regime in our fits, and expect that the lattice distortions will not matter so our simple form will suffice to get a first estimate of the diffusion coefficient. This also satisfies the general relation for the spectral bosonic function : $\rho(\omega) = -\rho(-\omega)$. We will discuss the possibility of other forms in the discussion of systematics.

3.3 Algorithm and simulation parameters

A reliable estimate of κ requires an accurate computation of the correlation function $G(\tau)$ especially at large temporal separations. As is well known in the case of Polyakov loops, accurate determination of objects like $G(\tau)$ (see Eqn. 3.10) is very difficult for large τ. A brute force application of the standard methods (combination of overrelaxation and Metropolis) to calculate these correlation functions does not yield acceptable results for this problem. We use the Multilevel algorithm [10] which is known to exponentially reduce errors on certain operators. This algorithm has been used previously in the literature to accurately calculate the Wilson loop, correlation functions of Polyakov loops as well as the glueball spectrum [10, 11, 12, 13, 14]. We will explain later how the use of this algorithm improves over the results from standard method.

The key idea of the multilevel algorithm is to divide the lattice into several sublattices. The locality of the gauge action allows the value of certain extended operators

to be expressed as the product of the expectation values of certain other operators over the sub-lattices. These sub-lattice expectation values are calculated by holding the boundary links fixed. From the averaging in each of the time slices, a single measurement of the operator of interest is obtained. The operator is then measured N times by repeating the procedure. A variety of parameters such as number of sublattices, number of sublattice averaging or even the use of nested sublattices can be tuned to increase the efficiency of the algorithm.

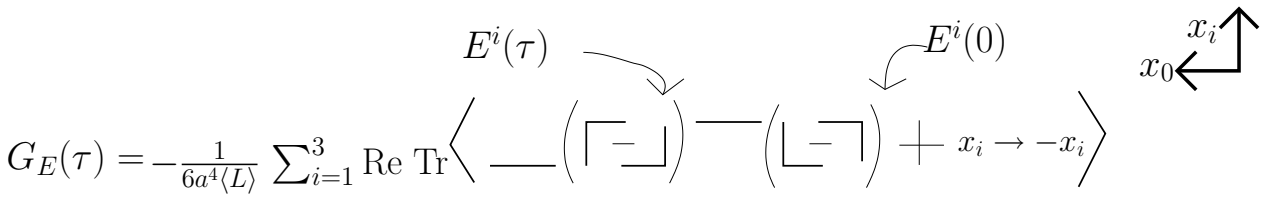

Figure 3.1: Graphical representation of the chromo-electric field correlation function.

The standard lattice form of the chromo-electric field is a (x,t) plaquette where x is the generic spatial index [15, 16]. In Ref [7], the authors suggest another discretization of the chromo-electric field which has only two right-angled cusps; and hence is expected to be less ultra-violet sensitive than the standard plaquette representation. This is obtained from a lattice representation of the spatial heavy quark current in the non-relativistic regime, and this has been used for our calculations. A heuristic way to understand the operator is to observe that $E_i = [D_0, D_i] = D_0D_i - D_iD_0$. On the lattice, the D_0, D_i may be replaced by the gauge links in $0, i$ directions. Thus, the correlation functions in Eqn. 3.10 can be best represented graphically as shown in Fig 3.1. The graphical expression given in Fig. 3.1 can expressed in terms of a combination of loop operators, each with a "handle". The expression in numerator (which we call $E(\tau)$) can be expressed as: $E(\tau) = 2C(\tau) - C(\tau+1) - C(\tau-1)$ where $C(\tau)$ is a loop operator with a "handle" in the spatial direction of extent τ, and is represented graphically in fig 3.2

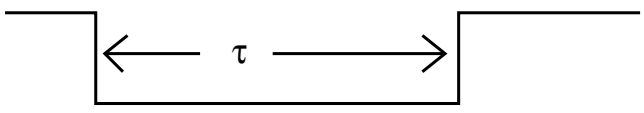

Figure 3.2: Graphical representation of $C(\tau)$

For the explicit construction of the correlators using the Multilevel algorithm, let us consider a specific example of a lattice with $N_t = 8$. Because of periodicity, there are only four independent correlation functions that need to be calculated, as shown

in Fig 3.3. For the purposes of this section, we will use the notation $G(\tau) = E(\tau)/L$, where $E(\tau)$ is the operator with the insertion of the chromo-electric fields on two different timeslices, a distance of τ apart and L is the Polyakov loop.

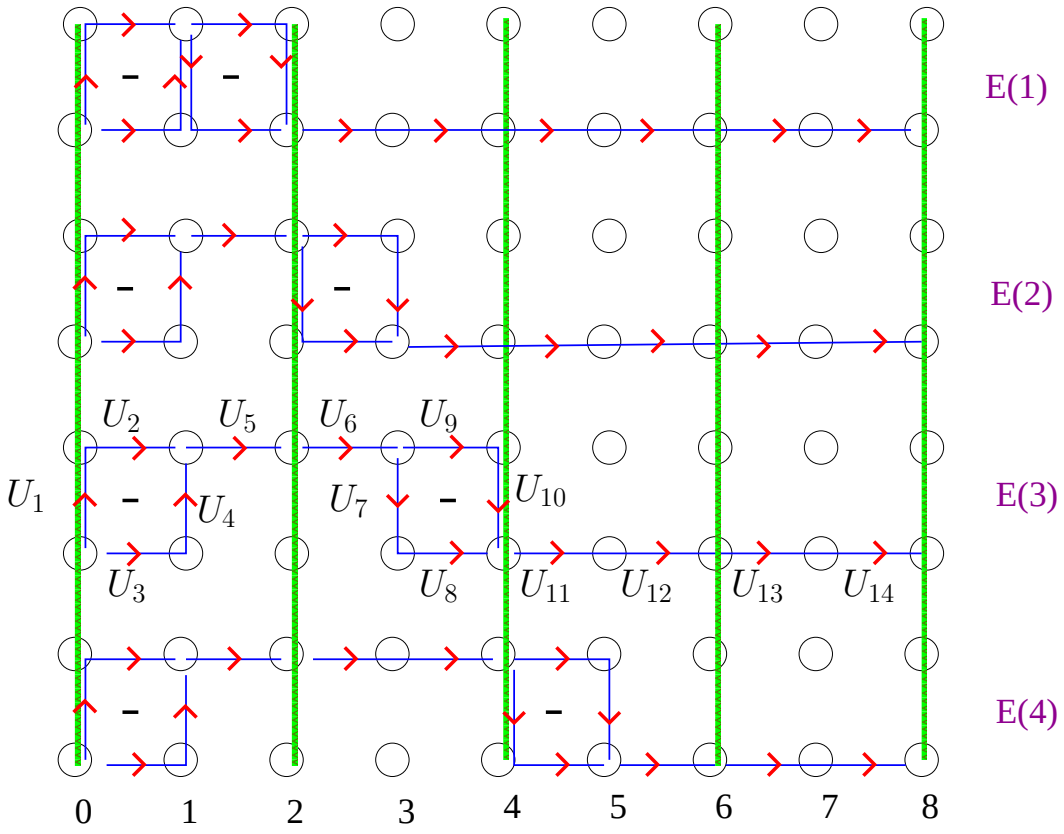

Figure 3.3: Schematic figure explaining the calculation of $E(\tau)$ on $N_t = 8$ lattice using the Multi-level algorithm

Consider the calculation of the $E(3)$ in Fig 3.3. The electric fields are separated by three lattice spacings in the temporal direction, with the gauge links denoted by arrows. The lattice has been divided into 4 sublattices each of width of two lattice spacings. Because of periodic boundary conditions the 8^{th} time-slice co-incides with the 0^{th} time-slice. In terms of these links, the expression for $E(3)$ is

$$\begin{aligned} E(3) &= \langle \mathrm{Tr}\,\{(U_1U_2 - U_3U_4)U_5U_6(U_7U_8 - U_9U_{10})U_{11}U_{12}U_{13}U_{14}\}\rangle \\ &= \langle \mathrm{Tr}\,\{[(U_1U_2 - U_3U_4)U_5]\,[U_6(U_7U_8 - U_9U_{10})]\,[U_{11}U_{12}]\,[U_{13}U_{14}]\}\rangle \end{aligned} \quad (3.11)$$

The sublattice averaging $[(U_1U_2 - U_3U_4)U_5]$ means that this sublattice is averaged over keeping all other links frozen. An identical procedure is followed for measuring each of the correlation functions. The Polyakov loop L appearing in the denominator is also measured using this procedure. Note that this is only possible because the

action is local. With fermions put in, the non-local fermion determinant appears in the measure and this method cannot be used because it is no longer possible to hold any link fixed while others are updated.

Note that $E(\tau)$ used in the calculation transform exactly like L under the global Z_3 transformation, and therefore vanishes in the confined phase. Without any modification using source terms, the $G(\tau)$ as defined in Eqn. 3.10 cannot be calculated below T_c. Our calculations using the Multilevel algorithm therefore focussed on temperatures above T_c to calculate the correlation functions at seven different temperatures varying from 1.066 T_c to 3.0 T_c on a variety of lattices with different temporal extents and spatial volumes. In Table 3.1 we list all the lattices used and the couplings, the number of sublattices used in the multi-level updates and the number of averaging in each sublattice (called *iupd*). The table also lists the number of measurements collected at each of these parameter values.

For most of our runs we have used 2000 sublattice averagings. This was essential for the larger lattices with $N_t = 20, 24$. For smaller β, larger averaging was required to get error-bars down to a few percent. For $N_t = 12$ at larger β values, we found that even 200 sublattice averagings yielded good signals when the number of sublattices were large. We noted that using smaller sublattice averagings often gave rise to larger autocorrelation. For our runs, we have tuned these such that all correlators have autocorrelation times less than 3 - 4.

It is known that the Multilevel algorithm can be especially useful to calculate quantities that have an exponentially decaying signal-to-noise ratio. The merit of the Multilevel lies in the fact that with proper tuning, it can maintain fixed *relative* error even for observables at very large spatial or temporal extents. This was first shown by Lüscher and Weisz [10] on the expectation values of Wilson loops. For large Wilson loops, the signal-to-noise ratio decreases like $\mathrm{e}^{-\sigma A}$ in the confined phase with standard algorithms, where A is the area of the loop and σ is the string tension. For a Wilson loop of $r = 6a \simeq 1fm$ and $T = 12a$, they noted that the Multilevel is more efficient by a factor of about 3×10^5 (which was measured in terms of the computer time to reach the same error in the same machine). This increases for loops with even larger extents.

Let us give a quantitative estimate of the improvement in our correlation functions with the Multilevel algorithm. For $\beta = 6.9$, $N_t = 20$ and $N_s = 36$, $G(\tau)$ was also calculated using the standard method. The correlator for the largest τ, $G(10)$ has the value of 2.133(76) $\times 10^{-4}$ from 350 multilevel measurements. The multilevel takes about 800 minutes to make a single measurement on an Intel Xeon CPU processor with a speed of 2.5 GHz. For the same correlator, the standard method gives the

N_t	N_s	β	T/T_c	# sublattice	*iupd*	# measure
12	24	6.4	1.066	3	2000	190
12	36	6.4	1.066	3	2000	200
12	48	6.4	1.066	6	200	180
16	48	6.6	1.066	4	2000	132
20	48	6.76	1.066	5	4000	170
12	48	6.42	1.125	3	2000	150
16	36	6.65	1.125	4	2000	250
16	48	6.65	1.125	4	2000	215
20	48	6.80	1.125	5	3000	150
12	48	6.47	1.2	3	2000	150
16	48	6.68	1.2	4	2000	120
20	36	6.9	1.2	5	2000	350
20	48	6.9	1.2	5	2000	96
12	24	6.65	1.5	6	200	400
12	36	6.65	1.5	6	200	260
12	48	6.65	1.5	6	200	180
16	36	6.9	1.5	4	2000	230
16	48	6.9	1.5	4	2000	200
24	48	7.192	1.5	4	2000	450
24	56	7.192	1.5	4	2000	50
24	56	7.192	1.5	4	4000	45
12	36	6.9	2.0	6	200	220
12	48	6.9	2.0	6	200	188
16	48	7.074	2.0	4	2000	132
20	48	7.255	2.0	5	2000	194
12	48	6.94	2.25	3	2000	132
16	48	7.192	2.25	4	2000	200
12	48	7.192	3.0	3	2000	210
16	48	7.457	3.0	4	2000	140

Table 3.1: Parameters of the runs used in the computation of the chromo-electric correlation functions $G(\tau)$

value: -3.26(2.28) $\times 10^{-3}$ for a runtime of about 8500 minutes on the same machine. Since the achieved error-bar using the multilevel is a factor of 300 lesser, it would take about 7.6 $\times 10^8$ min to get same level of error using the standard method. In this time about 9 $\times 10^5$ multilevel measurements can be made. The multilevel is therefore about a factor of 2.5 $\times 10^3$ times more efficient than the standard algorithm for G(10) at this coupling. An exactly similar comparison made for $G(3)$ shows that the time required to reduce the errors in the standard method to the level of 350 multilevel measurements is sufficient to make 6 $\times 10^4$ multilevel measurements, an improvement by a factor of 200. This demonstrates the use of the Multilevel to be indispensable

for this calculation, especially for larger τ.

3.4 Results

In this section we will discuss the structure of the correlation functions and the theoretical inputs that we have used in order to parameterize them. We will present a discussion on our approach to obtain renormalized values of the diffusion coefficient from the bare fit parameters and a discussion on finite volume effects.

3.4.1 Correlation Functions

Since the electric field has mass dimension 2, we study the dimensionless combination $G(\tau)/T^4$ to analyze the temperature dependence at a fixed gauge coupling β arising from different N_t. Fig 3.4 shows the correlation functions at two different β; each for three different values of N_t. The top figure is for $\beta = 6.9$ with the N_t chosen such that the temperature varies from 1.2 to 2 T_c; while the bottom figure is for $\beta = 7.192$ and temperature varying from 1.5 to 3 T_c. The most remarkable result is that the long distance part of the correlation functions fall on top of each other, which indicates that this part captures some temperature independent continuum physics. It is possible therefore that the dimensionless diffusion coefficient extracted from the long distance part of the correlation functions may not have a pronounced temperature dependence. This result is independent of the renormalization factors since they will solely depend on the gauge coupling β, which is the same for all the different N_t's. Since κ has a mass dimension of 3 (Eq. 3.9), the dimensionless ratio to consider is κ/T^3. The figures then imply that the renormalized values of κ/T^3 may not have any pronounced temperature dependence in the aforementioned temperature range. This point will be discussed in detail later. Further, the long distance part of the correlation functions are much flatter than expected from only a single particle state. The discretization effects of the finite lattice spacing is visible in the correlation functions for small τ, but seem to decrease considerably by $\tau T \sim 0.25$.

As discussed before, the spectral function is parameterized as $\rho(\omega) = a_1\omega + a_3\omega^3$. Using Eqn. 3.8, the functional form of $G(\tau)$ that needs to be fitted with the data is

$$\frac{G(\tau)}{T^4} = \frac{1}{\langle L\rangle} N_t^4 \left[\frac{a_1\pi}{N_t^2}\frac{1}{\sin^2(\pi\hat{\tau}/N_t)} + \frac{a_3 6\pi^3}{N_t^4}\left(\frac{1}{3\sin^2(\pi\hat{\tau}/N_t)} + \frac{\cos^2(\pi\hat{\tau}/N_t)}{\sin^4(\pi\hat{\tau}/N_t)}\right)\right] \quad (3.12)$$

where we have explicitly written out the Polyakov loop ($\langle L\rangle$) and the N_t dependence in the correlation function. $\hat{\tau} = \tau/a$ is the dimensionless temporal distance, where

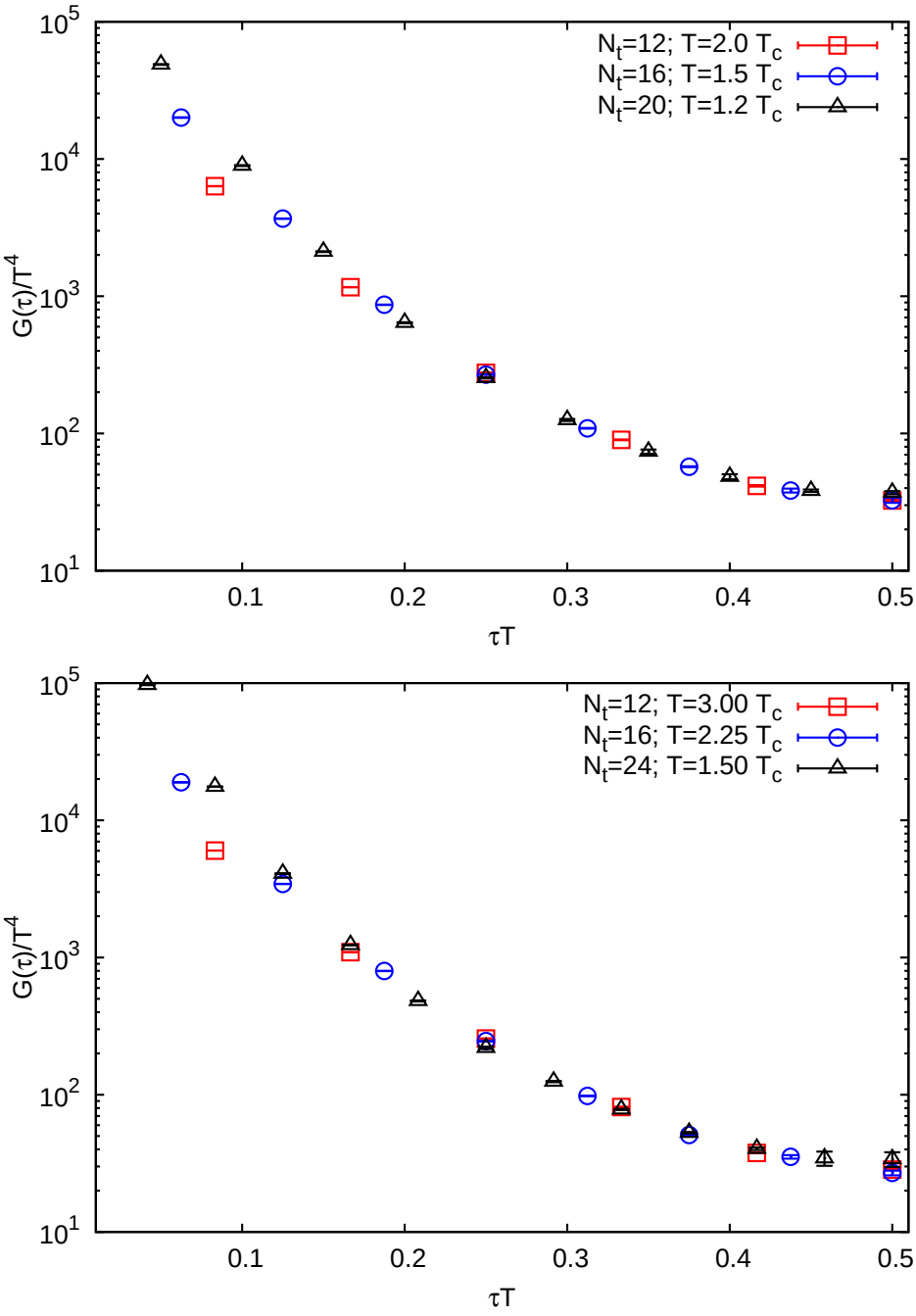

Figure 3.4: Comparison of correlation functions for different N_t

a is the lattice spacing. The behaviour of the LO result ($\rho(\omega) = a_3\omega^3$) is not too different from the full correlation function. Fig 3.5 shows this at $\beta = 7.192$, with the value of a_3 chosen arbitrarily. In fact, a fit using only the ω^3 contribution is able to describe the data on smaller lattices of $N_t = 12, 16$. Fig 3.5 shows an example of fitting $N_t = 16$ lattice at 1.5 T_c with only the ω^3 contribution. This leads us to

suspect that the diffusive part is rather small, so that the few data points we have for the smaller lattices is not enough to disentangle the contribution of a_1. Therefore, we have not quoted any estimate of a_1 from these lattices. However, on finer lattices, with lattice spacings of $a = 1/(20T)$ and $1/(24T)$, the contribution of a diffusive part is unambiguous, and we are able to extract values of a_1, characterizing the diffusive contribution. Even then, the ω^3 gives the dominant contribution and the fitted value of a_1 is about two orders of magnitude smaller than the fitted a_3, making it rather difficult to extract even on our largest lattices. Finer lattices with more data in the large τ region and with at least similar percentage errorbars seem essential in determining a_1 reliably to a few percent.

The results obtained by fitting the form in Eqn. 3.12 to the correlation functions are reported in Table 3.2. All the fits were done by taking into account the correlations existing between the different $G(\tau)$ at different τ via a covariance matrix. The errors on the fit parameters were calculated by the standard Jackknife procedure. The quoted values in the Table 3.2 are for the largest temporal lattices of N_t=20 and 24. The fits were made in the range 0.3 - 0.5 to avoid the lattice discretization effects, as we discuss later. The value of the fitted a_1 was found to be rather dependent on the range used to make the fit, and changed roughly about 30-40%. The quality of the fits for some lattices is displayed in Fig. 3.6.

β	T/T_c	N_t	N_s	Range	χ^2/DOF	a_1	err	a_3	err
6.76	1.066	20	48	6-10	1.97	9.09×10^{-6}	1.54×10^{-6}	0.99×10^{-3}	4.9×10^{-5}
6.80	1.125	20	48	6-10	0.23	8.66×10^{-6}	1.17×10^{-6}	1.17×10^{-3}	3.0×10^{-5}
6.90	1.2	20	36	6-10	1.03	1.45×10^{-5}	2.39×10^{-5}	1.46×10^{-3}	2.9×10^{-5}
6.90	1.2	20	48	6-10	1.47	1.49×10^{-5}	2.81×10^{-6}	1.53×10^{-3}	3.7×10^{-5}
7.192	1.5	24	48	6-12	1.08	7.36×10^{-6}	4.21×10^{-7}	8.09×10^{-4}	1.0×10^{-5}
7.192	1.5	24	56	6-12	0.82	6.06×10^{-6}	3.29×10^{-6}	8.22×10^{-4}	3.4×10^{-5}
7.255	2.0	20	48	7-10	0.55	3.15×10^{-5}	8.82×10^{-6}	2.57×10^{-3}	1.2×10^{-4}

Table 3.2: Fitted parameters of the chromo-electric correlation functions $G(\tau)$

Systematics of the choice of the fit function

Ideally one would like to rule out any other physically motivated fit form based on fitting to the non-perturbatively calculated results alone. In our case, we have found that just the diffusive part, together with two δ-function peaks in the spectral function gives a reasonably good description of the correlation functions over almost all the temperatures and different N_t lattices. The motivation for the δ-functions come from the expectation that the spectral function for large-ω will be affected by the edges of Brillouin zone, and would give rise to some non-universal structure in it. This was

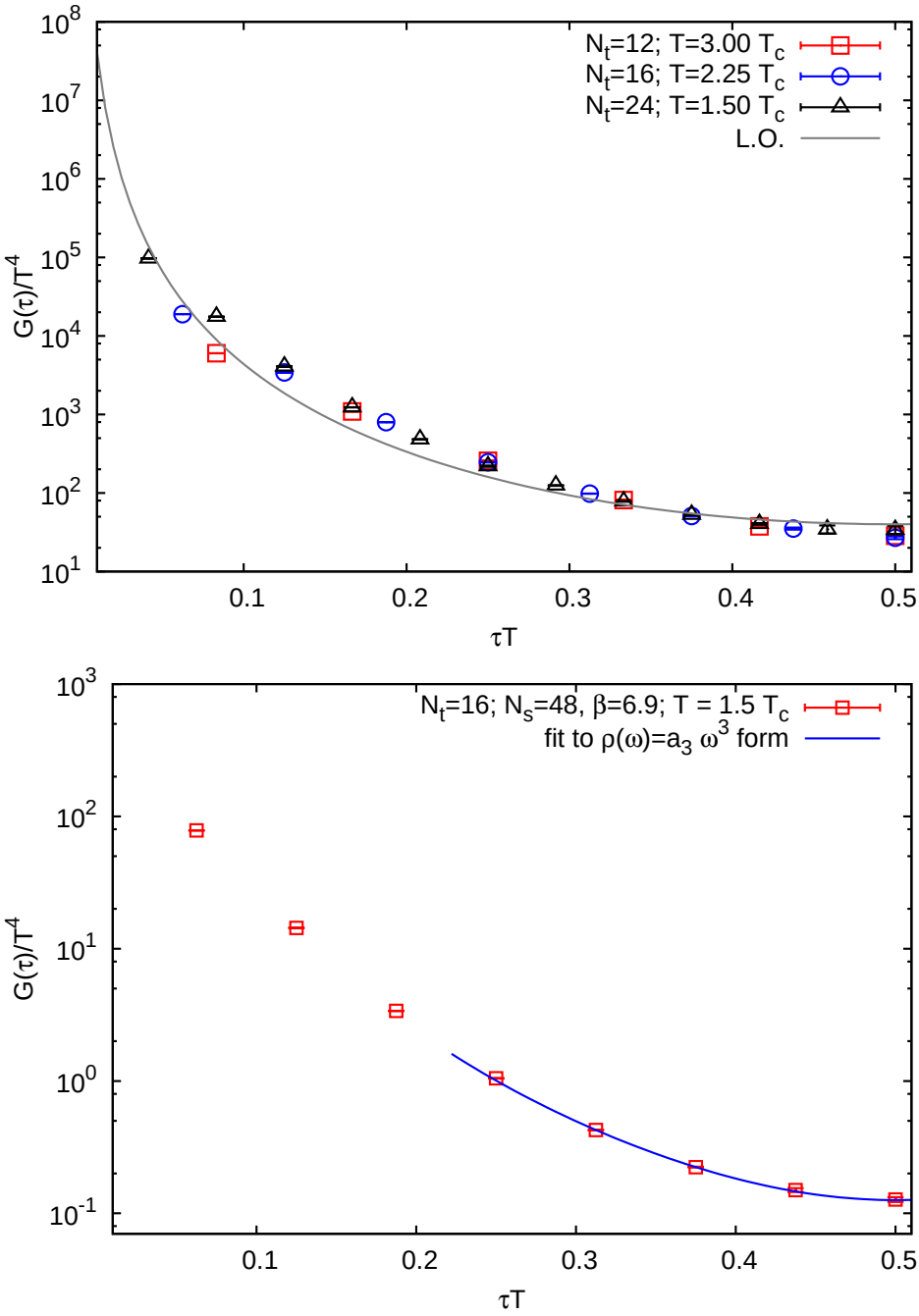

Figure 3.5: (Top): Comparison of correlation functions for different N_t at $\beta = 7.192$ with the leading order result. (Bottom): $\rho(\omega) = a_3\omega^3$ can fit the long distance correlation function for the small N_t. This is an example of $N_t = 16$ at $\beta = 6.9$.

actually seen in in Ref [17], which found the existence of peaks at the edges of the Brillouin zone in the spectral function from a lattice calculation in the Hamiltonian formulation. Approximating the peaks as delta-functions in the spectral function, we

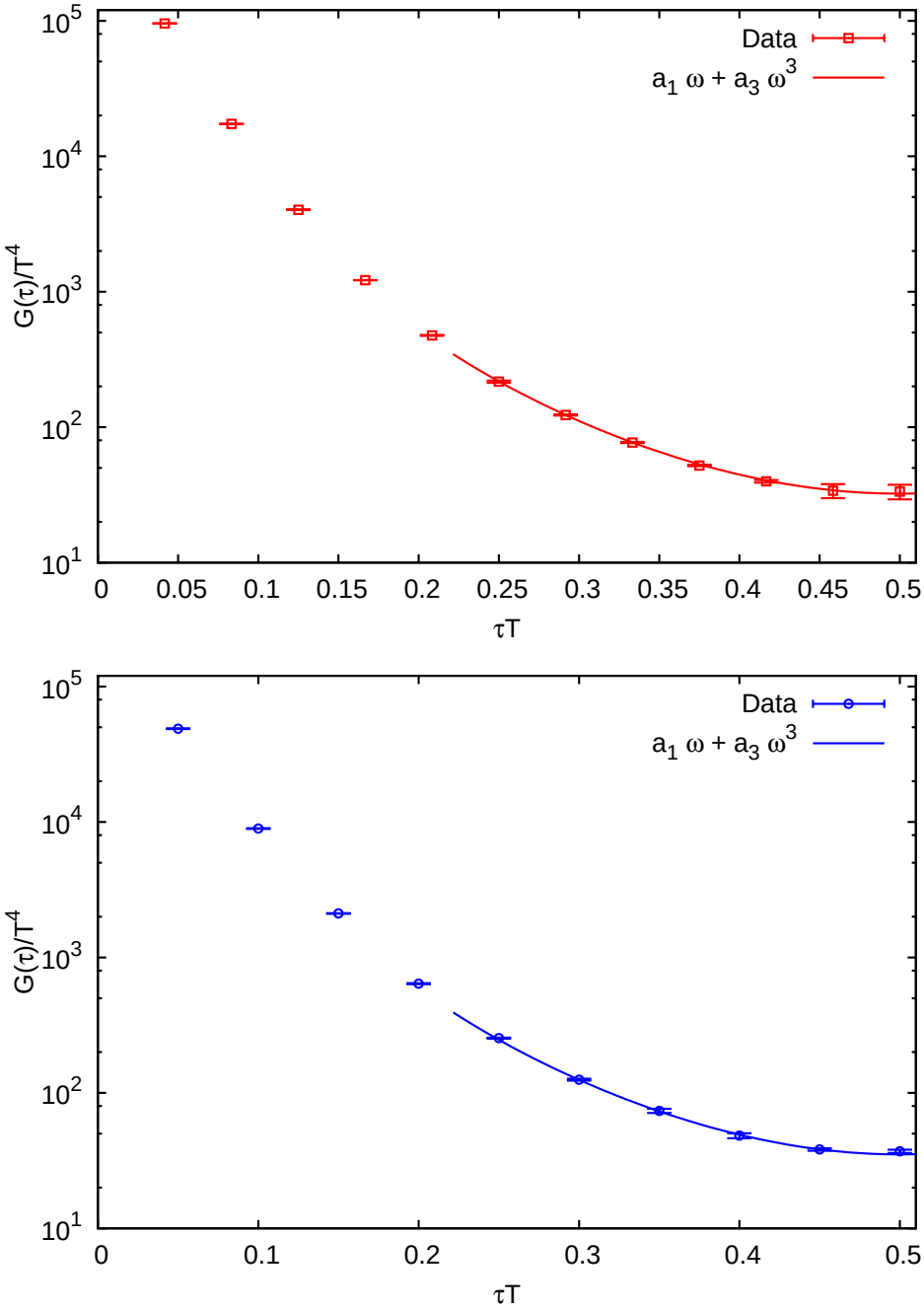

Figure 3.6: The fit of the correlation functions with the form in Eqn 3.12. The top figure is for N_t=24, N_s=48, β=7.192 which corresponds to a physical temperature of 1.5 T_c, while the bottom panel is for N_t=20, N_s=48, β=6.9 at 1.2 T_c. In both cases the numerical value of a_3 is about a hundred times larger than a_1.

get the following from for the correlation function $G(\tau)$:

$$G(\tau) = \frac{a_1 \pi}{N_t^2} \frac{1}{\sin^2(\pi\tau/N_t)} + A_1 \cosh(M_1(\tau - 1/2T)) + A_2 \cosh(M_2(\tau - 1/2T)) \quad (3.13)$$

Since the last two terms are lattice artefacts, we expect that M_1 and M_2 will not scale with temperature. While this form of the correlation function can fit almost the whole of the correlation function, even in the low-τ region, the behaviour of M_1 and M_2 are very different. While M_2 does not change with N_t, we found that M_1 scales. For example, at $\beta = 7.192$, we found that $M_1 = 0.70, 1.02, 1.38$ on $N_t = 24, 16, 12$ respectively which implies that $M_1/T \sim 16.5$ and does not change with temperature from 1.5 T_c to 3 T_c. This is not expected for a lattice artefact.

An example of fitting the N_t=24, N_s=48 and β=7.192 result with the form in Eqn. 3.13 is shown in Fig 3.7. From the figure, it is suggestive that if the low-τ region is indeed parameterized by 2-mass terms *only* then doing the fit in the range 0.3-0.5 should ensure that the result for a_1 is not dominantly contaminated by discretization effects. The value of a_1 is larger by roughly a factor of 5 than the values quoted in Table 3.2, which is because of the absence of the ω^3 term. In particular, the inclusion of the $a_3\omega^3$ term to the form in Eqn. 3.13 makes the fit rather unstable. This is probable since we are trying to do a non-linear fit with many parameters but a few points. We have not used the fit form in Eqn. 3.13 to quote results for a_1, since we feel it is more physical to include ω^3 in the fit form, and restrict to larger-τ, such that a_1 is reasonably free from discretization effects. Moreover, the unexpected scaling of M_1 is also not very clear.

3.4.2 Renormalization

The bare correlation functions have been calculated at different N_t and for different couplings. These need to be renormalized in order to construct a physical observable. It is known that the Wilson loops, with a finite number of cusps are multiplicatively renormalizable upto all orders in perturbation theory [18, 19, 20]. All these renormalization factors are dependent on g^2 and hence on β, as is the case for $T = 0$. Non-perturbative renormalization constants are not known for this electric field operator. However, the renormalization can still be done by relating the value of $\langle P \rangle$ measured in the simulation to α_S at the scale $\mu = (3.4/a)\exp(-5/6)$. Since this scale is rather large, it might just be sufficient to perform the renormalization upto the leading order by removing the self-energy corrections to the heavy quarks. For this purpose, we have implemented the tadpole improvement on our correlation functions [21].

Tadpole improvement replaces all links U_μ in the lattice expressions with $Z_L U_\mu$ where Z_L is related to the expectation of the plaquette (at $T = 0$) measured in a

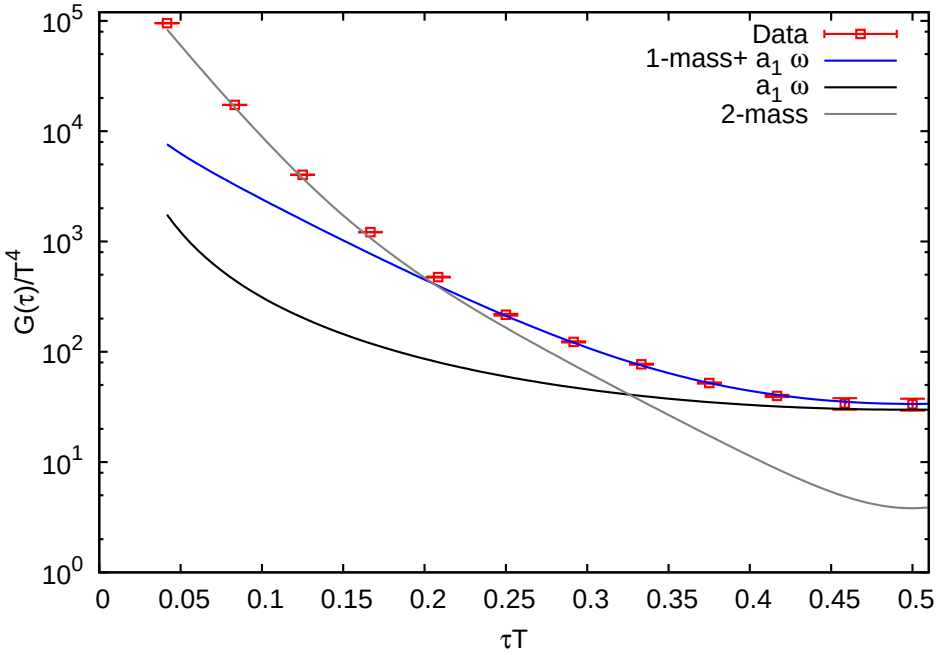

Figure 3.7: Attempts to parameterize the discretization effects in the correlation function. This is for N_t=24, N_s=48, β=7.192. Note that the 2-mass contribution fits the short distance correlators nicely.

simulation:

$$Z_L^{-1} = \left(\frac{1}{N}\langle \mathrm{Tr} U_p \rangle\right)^{1/4} = (\langle P \rangle)^{1/4}. \tag{3.14}$$

Because Z_L is measured in the simulation, it might also remove some of the non-perturbative renormalization of the lattice operators. For our operators, the renormalization of the straight temporal part of the correlation functions is cancelled by that of the Polyakov loop. The renormalized value of the correlation functions are simply given by multiplying Z_L^2 with our bare correlator values, since $E(\tau)$ has two more links than L. The Z_L^2 factor in our case is then just given by the inverse of the square root of the plaquette at the respective β and is listed in Table 3.3.

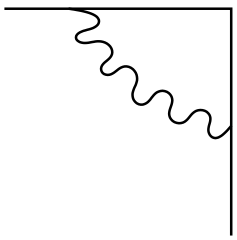

Figure 3.8: The leading contribution to the cusp renormalization factor.

Our operators also have four cusps, which can give a logarithmic divergence depending on its orientation [18]. For the cusp renormalization factor Z_C, the one gluon exchange diagrams of the type shown in Fig 3.8 are responsible for the leading order contribution in perturbation theory. It can be argued that this contribution vanishes in the leading order. This diagram is proportional to the gluon propagator, which in the Feynman gauge is, in turn, proportional to $\delta_{\mu\nu}$. Since the cusp is formed by two loop segments in mutually orthogonal directions, this factor is zero. This result is already known in perturbative calculations of Wilson loops [23]. Thus, to leading order, $Z_C = 1$.

To cross-check our renormalization procedure, we use the tadpole improvement with the cusp factors set to unity on the electric field operators used in [16]. Since the non-perturbative renormalization constants are calculated there, a direct comparison can be made. Ref. [16] use the standard plaquette representation of the electric fields. This means that the tadpole improvement factor for this operator is $1/\langle P \rangle$. For $\beta = 6.0$, the tadpole improvement gives the value 1.68, while with non-perturbative renormalization they obtain 1.62. At $\beta = 6.3$, the former gives 1.61 while the latter obtain 1.56. This agreement of better than 4 % is very encouraging since this procedure, though naive, can capture the non-perturbative renormalization very well. Moreover, at higher β, the agreement is expected to improve further. Therefore, we have used the tadpole improvement renormalization factor to renormalize our final bare values.

To cross-check these estimates, we have also obtained non-perturbative renormalization factors for Z_L, by computing the bare Polyakov loops L_B at high temperatures and then relating it to the non-perturbatively computed Polyakov loops L_R in [22]. It is known that the Polyakov loop gets renormalized as [18]:

$$L_R = Z_L^{N_t} L_B \tag{3.15}$$

where N_t is the temporal extent of the lattice. This has the advantage that any systematic dependence on N_t is expected to be removed since this procedure was implemented with lattices having identical N_t. These values of Z_L^2 are also reported in Table 3.3. These two schemes for calculating Z_L^2 gives us values that vary by 30 - 40 % in the temperature range considered here.

3.4.3 Finite Volume Results

We have observed practically no volume dependence in our correlation functions. Fig 3.9 (top) shows this result for the largest N_t lattices used in the extraction of the

β	T/T_c	Z_L^2 (Tadpole improvement)	Z_L^2 (from $\langle L_R \rangle$ matching)
6.76	1.066	1.23409	1.71484
6.80	1.125	1.23165	1.70660
6.90	1.2	1.2258	1.68374
7.192	1.5	1.21049	1.62960
7.255	2.0	1.20749	1.61831

Table 3.3: The different estimates for the factor Z_L^2 obtained using Tadpole improvement and from matching with renormalized Polyakov loop. The agreement is typically 30-40 % within the temperature range considered.

diffusion coefficient at two different temperatures T=1.2 T_c and 1.5 T_c. At the each temperature, the correlation functions from lattices with different spatial extents fall on top of each other. An exactly similar result is obtained for the renormalized dimensionless diffusion coefficient κ/T^3 as shown in Fig 3.9. The values of the renormalized κ/T^3 quoted here are obtained using the tadpole improvement factor for Z_L.

3.4.4 Discussion

In this section, we will discuss our results about the renormalized dimensionless diffusion constant and compare its estimation with that of other methods used, namely, perturbation theory and AdS/CFT techniques. We will also compare our results with the values required by various models that give reasonable description to the RHIC data [26]. To have a more direct comparison to calculations using these other methods, we will convert our estimates of κ/T^3 to DT by simply using the Einstein fluctuation-dissipation relation:

$$D = \frac{T}{M\eta_D} = \frac{2T^2}{\kappa}, \tag{3.16}$$

where η_D is the drag constant already encountered in Eqn. 3.3.

Fig 3.10 shows the renormalized non-perturbative estimates of DT from our computation. The main values shown in red circles are obtained using the fit parameters listed in Table 3.2 along with the tadpole improvement for the renormalization constant in Table 3.3. We have also indicated the shift in the mean value due to the change in the fit range by blue lines above and below. The primary result that emerges out of these values is that there is no significant temperature dependence of the dimensionless quantity DT in the temperature range from 1.066 T_c to 2 T_c. The behaviour of the correlation functions from fig 3.4 suggest that this behaviour may continue upto higher temperatures $\sim 3T_c$. Finer lattices with more data in the

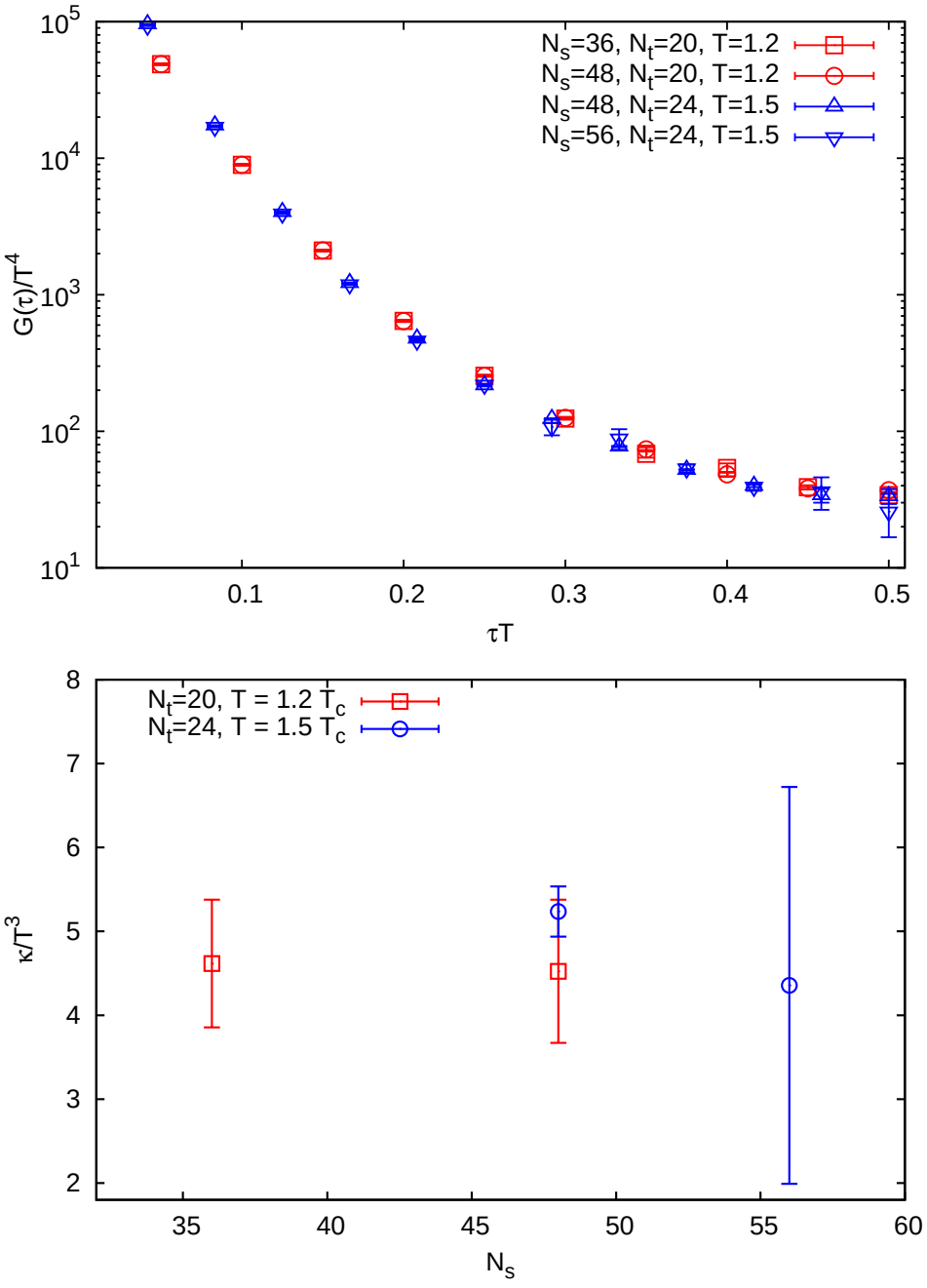

Figure 3.9: Volume independence of our results (Top): Correlation functions for different N_s at T = 1.2 T_c and 1.5 T_c fall on top of each other. (Bottom): Renormalized value κ/T^3 at the same two temperatures as before, do not show any volume dependence. The error-bar on N_s=56 is large due to small statistics.

large-τ direction will be required to confirm our expectations.

Let us now consider how the estimates obtained from perturbation theory [5] compare with the non-perturbative values presented here. For very high temperatures,

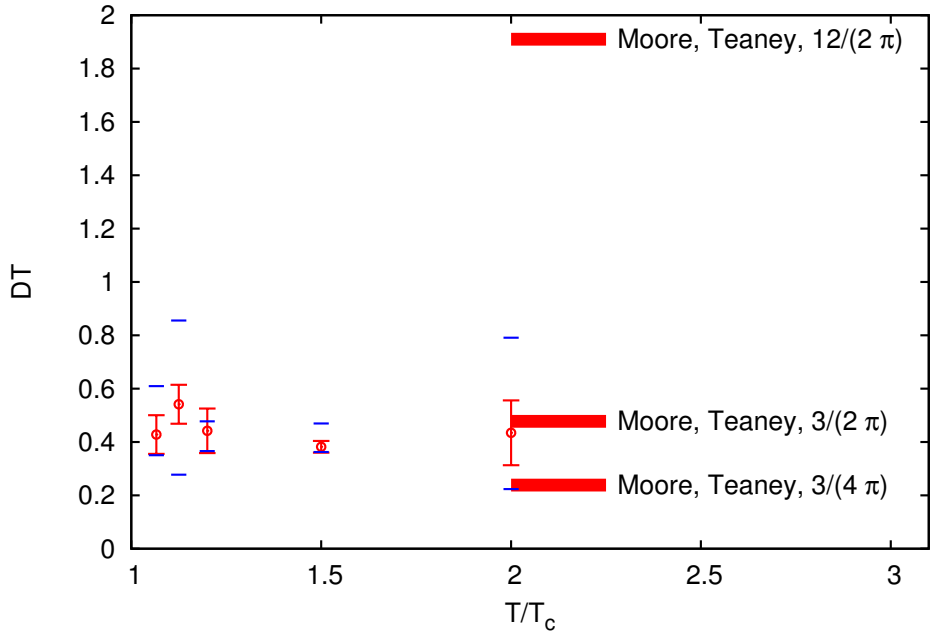

Figure 3.10: The non-perturbative estimates of the dimensionless diffusion coefficient $DT = 2/(\kappa/T^3)$. The blue lines above and below the usual symbols denote the shift in mean due to change in the fit range. There is no pronounced temperature dependence in the range 1.066 T_c to 2 T_c. The value $3/4\pi$ is the value required by phenomenological models to give a reasonable description to the RHIC data [5].The value of $12/2\pi$ is a very optimistic estimate from perturbation theory using $\alpha_S \approx 0.5$ and $m_D/T \approx 1.5$, where m_D is the Debye mass [5].

such that $m_D/T \ll 1$, the analytic expression for DT has been obtained [5]

$$DT = \frac{36\pi}{C_F g^2}\left[N_c\left(\ln\frac{2T}{m_D} + \frac{1}{2} - \gamma_E + \frac{\zeta'(2)}{\zeta(2)}\right) + \frac{N_f}{2}\left(\ln\frac{4T}{m_D} + \frac{1}{2} - \gamma_E + \frac{\zeta'(2)}{\zeta(2)}\right)\right]^{-1}, \tag{3.17}$$

where $C_F = 4/3$ for SU(3) gauge theory. At very high temperatures, DT diverges as $1/\alpha_S^2$. This expression however, becomes unreliable for lower temperatures of a few T_c, and even diverges close to T_c, for the pure gauge theory. This happens because as temperature decreases, $\ln\frac{2T}{m_D}$ decreases, since m_D/T increases. At some critical value, this cancels the factor $1/2 - \gamma_F + \frac{\zeta'(2)}{\zeta(2)} = -0.647$, and the denominator vanishes. In fact, the expression for DT in Eqn. 3.17 is based on a small m_D/T expansion of Eqn. (11) of [5] and therefore becomes invalid at lower temperatures. A numerical evaluation of the expression for DT in Eqn. (11) of [5] is indispensable if any comparison needs to be made with our results. For this comparison, we will not write out the complicated expression, but rather state the numerical values obtained

for the DT values. In making this estimate, the α_S is evaluated in the $\overline{MS}$ scheme at a scale $\mu = 3T$. First, the non-perturbative value of α_S at the inverse lattice spacing scale, $\mu_1 = (3.4/a)\exp(-5/6)$ is obtained from the plaquette values [21] and then the 2-loop beta function is used to flow to the scale $\mu = 3T$ to get the estimate of α_S at 1.5 T_c, which is about 0.229. At this temperature, the non-perturbative estimate of the Debye mass from lattice calculation is about 2.345 T [24]. The dimensionless diffusion coefficient is then $DT \simeq 14$ [5]. This estimate is about 28 times the non-perturbative value. A similar procedure at temperatures, 2.25 T_c and 3 T_c yield the values of DT to be 18.47 and 21.07 respectively. It is clear therefore that the result from perturbation theory is drastically different from the non-perturbative values that we have obtained both in terms of absolute value and in terms of temperature dependence.

In perturbation theory, the inclusion of two light fermion flavours decrease the value of DT by almost a factor of two in the leading order. Since at the temperatures we are concerned with, the medium is strongly interacting, the magnitude of the change in an non-perturbatively calculated result might be very different even if the trend is similar.

The next-to-leading order (NLO) contribution to the diffusion constant has also been calculated in perturbation theory. At similar temperatures, with $\alpha_S \sim 0.2$, this gives the $DT \sim 8.4/(2\pi)$ for $N_f = 3$ [25]. While this brings the value much closer to our non-perturbative estimate, it is rather disconcerting since it differs about 40 % from the leading order result. This shows that the convergence of the perturbation theory for this observable is rather poor, and accurate predictions cannot be made with it. Nevertheless staying with the NLO calculation, the estimate of DT comes closer to our estimate.

This quantity has also been computed in the strong coupling limit using AdS/CFT methods [6]. In this calculation, the expression for DT in terms of the strong coupling α_{SYM} is

$$DT \simeq \frac{0.9}{2\pi}\left(\frac{1.5}{\alpha_{SYM}N}\right)^{\frac{1}{2}} \tag{3.18}$$

To compare the estimate with perturbation theory and our results, we use N=3 and $\alpha_{SYM} = 0.23$; which gives $DT \simeq 0.2$. This is less than our central value, but not inconsistent with our results with the systematics included. However, this is about 56 times less than the corresponding value of DT using similar α_S in LO perturbation theory. It is also worthwhile to note that the parametric dependence on α_S in the results from perturbation theory and AdS/CFT are very different.

In fact, it is interesting to note that our results are in the neighbourhood of the values favoured by the phenomenological models that try to explain the PHENIX

results of v_2 and R_{AA} [26], shown as red lines in figure 3.10 corresponding to the values $DT = 3/2\pi$ and $3/4\pi$. Note that the work of Ref. [5] involved the tuning of various parameters in their model and the AdS/CFT methods [6] need to tune parameters to make the theory similar to QCD. Ours is the first non-perturbative first principles based calculation in quenched QCD, which gives a value of DT capable of explaining the charm flow data of the PHENIX at RHIC. It is clearly desirable to improve on this calculation by going to finer lattices and including light dynamical fermions. However, the various details of the models in [26] could also accommodate a variation of other parameters such that a variation of DT by a factor of 2 will still be in a good agreement with the data.

3.5 Conclusion

In this chapter, we have calculated the diffusion coefficient of heavy quarks in the gluon plasma. Using a formulation discussed in [5, 7], we have calculated the chromo-electric field correlation functions. The low-ω limit of the spectral function corresponding to this correlation function is directly related to the momentum diffusion coefficient of the heavy quarks.

To calculate the correlation functions to a few % accuracy, we used the Multilevel algorithm of Lüscher and Weisz. We have quantitatively compared the performance of the standard algorithm and the Multilevel scheme and concluded that the latter is indispensable if the standard Wilson action for the gauge action and the electric field operators proposed in [7] are used. We have used lattices of temporal lengths of $N_t = 12$ to 24, and with several volumes to check the finite volume effects in the final results. Our study spans the temperature range from 1.066 T_c to 3 T_c.

Our results indicate that very fine lattices with spacing of at least $a = 1/(20T)$ are essential to obtain any estimate of the diffusion coefficient. The diffusion constant is proportional to a_1, the coefficient of the ω term in $\rho(\omega)$. Due to the rather large contribution from the $a_3\omega^3$ term in $\rho(\omega)$, the former contribution is difficult to disentangle. We have been successful in doing this for a_1 on N_t =20 and 24 lattices.

Finally, we have compared our renormalized estimates of the dimensionless diffusion coefficient DT, with similar estimates from perturbation theory and AdS/CFT. We do not find any pronounced temperature dependence in this quantity in the temperature ranges that we have studied. While our estimates are about a factor 2 more than the corresponding results from AdS/CFT methods, they differ by an order of magnitude with the leading order perturbation theory at temperatures of $\sim 2T_c$. Further, our estimates are very close to the values of this quantity favoured by phe-

nomenological models that aim to describe the RHIC data.

References

[1] R. Baier et. al. *Nucl. Phys.* B 483 (1997) 291.

[2] Y. Dokshitzer and D. Kharzeev *Phys. Lett.* B 519 (2001) 199.

[3] A. Adare et. al. (PHENIX Collab.) *Phys. Rev. Lett.* 98 (2007) 172301 B.I. Abelev et. al. (STAR Collab.) *Phys. Rev. Lett.* 98 (2007) 192301.

[4] B. Svetitsky *Phys. Rev.* D 37 (1988) 2484.

[5] Guy D. Moore and Derek Teaney *Phys. Rev.* C 71, 064904 (2005)

[6] J. Casalderrey-Solana and D. Teaney *Phys. Rev.* D 74 (2006) 085012.

[7] S. Caron-Huot, M. Laine and G. D. Moore *JHEP* 0904 (2009) 053.

[8] Y. Burnier, M. Laine, J. Langelage and L. Mether *JHEP* 1008 (2010) 094

[9] J. Kapusta and C. Gale, *Finite Temperature Field Theory*, Cambridge University Press.

[10] M. Lüscher and P. Weisz *JHEP* 0109 (2001) 010

[11] M. Lüscher and P. Weisz *JHEP* 0207 (2002) 049

[12] P. Majumdar *Nucl. Phys. Proc. Suppl.* 119 (2003) 1021-1023; *Nucl. Phys.* B664 (2003) 213-232

[13] S. Kratochvila and P. de Forcrand *Nucl. Phys. Proc. Suppl.* 119 (2003) 670-672; *Nucl. Phys.* B671 (2003) 103-132

[14] H. Meyer *JHEP* 0301 (2003) 048

[15] A. Huntley and C. Michael *Nucl. Phys.* B286 (1987) 211

[16] Y. Koma, M. Koma and H. Wittig *Phys. Rev. Lett.* 97 (2006) 122003

[17] M. Laine, G. Moore, O. Philipsen and M. Tassler *JHEP* 0905 (2009) 014

[18] A. M. Polyakov *Nucl. Phys.* B164, 71 (1980)

[19] V. S. Dostenko and S. N. Vergeles *Nucl. Phys.* B169, 527 (1980)

[20] R. A. Brandt, F. Neri and M. Sato *Phys. Rev.* D24, 879 (1981)

[21] G. Peter Lepage and P. B. Mackenzie *Phys. Rev.* D48, 5 (1993)

[22] S. Gupta, K. Hubner and O. Kaczmarek *Phys. Rev.* D77, 034503 (2008)

[23] U. Heller and F. Karsch; *Nucl. Phys.* B251 (1985) 254
G. Curci, G. Paffuti and R. Tripiccione; *Nucl. Phys.* B240 (1984) 91

[24] O. Kaczmarek and F. Zantow *Phys.Rev.* D71 (2005) 114510

[25] S. Caron-Huot and G. D. Moore *Phys. Rev. Lett.* 100 (2008) 052301; *JHEP* 0802 (2008) 081

[26] PHENIX collaboration (A. Adare et. al.) arXiv: 1005.1627

Chapter 4

Overlap operator at finite chemical potential

4.1 Introduction

In Chapter 2, we investigated the pattern of finite temperature restoration in 2-flavour QCD using staggered fermions. The finite temperature transition in our world is expected to be governed by chiral symmetry, since the up and down quarks have masses which are much smaller than the symmetry breaking scale of QCD. Pions are thus regarded as Goldstone bosons resulting from the dynamical symmetry breaking by the vacuum. Chiral perturbation theory and other phenomenological studies have demonstrated the utility and consistency of such assumptions [1].

As explained in Chapter 1, it is therefore desirable to have the chiral symmetry group of continuum QCD in the relevant fermion action that aims at studying the thermodynamics of QCD. The Overlap fermion formulation [2] is ideal for formulating fermion actions with the right symmetries as continuum QCD since it has an exact chiral invariance on the lattice. A fundamental aspect of QCD is the existence of the critical point in the $(T - \mu_B)$ plane, where μ_B is the chemical potential for baryon number. Based on models which have symmetries common with continuum QCD, the $(T - \mu_B)$ phase diagram is expected to have a critical point for two light and one moderately heavy quarks. Since it is important to have the right flavour identification, overlap fermions present a better choice from the staggered formulation.

Another interesting puzzle that requires a calculation using the overlap fermions concern the pion screening masses. It is known that, at 2 T_c, the quantity $1-\mu/\mu_{FFT}$ (where μ is the screening mass of the pion in the interacting theory and μ_{FFT} is the corresponding value in free field theory) increases from 8 % when the quarks

are quenched [3] to about 15 % when two flavours of light quarks are included (as discussed in Chapter 2) [4]. Quenched Wilson fermion seems to perform as well [5] as the quenched staggered. Recently, a calculation with the quenched overlap suggests that this deviation is only a few percent [6]. It is therefore important to check by doing dynamical calculations using the overlap if similar behaviour persists on making the quarks dynamical. It is however, difficult since the overlap operator is highly non-local, and dynamical simulations with overlap quarks are not yet feasible.

There are, however, other interesting questions that can be resolved analytically. It is known that the inclusion of chemical potential μ_B in the standard way in local Dirac operators such as the Wilson and the Staggered give rise to divergences in the thermodynamical quantities $\propto a^{-2}$ unless certain conditions are satisfied. Since the overlap operator is non-local it is unclear how such a procedure be implemented for it. It is non-trivial to construct the conserved current operator due to its non-locality. In this chapter, we study a proposal for the inclusion of chemical potential in the overlap operator [7]. A modification of the overlap operator was suggested there, such that the correct continuum action is obtained in the $a \to 0$ limit. We will analytically study this proposal and demonstrate that provided the modification of the overlap operator satisfy certain conditions, the spurious divergences do not arise and the correct expressions for the energy density, number density and the ideal gas equation of state (EOS) can be obtained. Interestingly, it turns out that the same conditions will be needed here as in the case of the local Dirac operators.

4.2 Thermodynamics of the overlap operator

The overlap Dirac operator [2] has the following form for massless fermions on asymmetric lattice with spacing a and a_4 in the spatial and temporal directions:

$$D_{ov} = 1 + \gamma_5 \mathrm{sgn}(\gamma_5 D_W) \ , \tag{4.1}$$

where sgn denotes the sign function and

$$\begin{aligned} D_W(x,y) &= (3 + \frac{a}{a_4} - M)\delta_{x,y} - \frac{a}{a_4}[U_4^\dagger(x-\hat{4})\delta_{x-\hat{4},y}\frac{1+\gamma_4}{2} + \frac{1-\gamma_4}{2}U_4(x)\delta_{x+\hat{4},y}] \\ &- \sum_{i=1}^{3}[U_i^\dagger(x-\hat{i})\delta_{x-\hat{i},y}\frac{1+\gamma_i}{2} + \frac{1-\gamma_i}{2}U_i(x)\delta_{x+\hat{i},y}] \end{aligned} \tag{4.2}$$

is the standard Wilson-Dirac operator on the lattice but with a negative mass term $M \in (0,2)$. The overlap operator satisfies the Ginsparg-Wilson relation [8] and

has exact chiral symmetry on the lattice. The corresponding infinitesimal chiral transformations [9] on a finite lattice for $N_f = 1$ are

$$\delta\psi = \alpha\gamma_5(1 - \frac{1}{2}aD_{ov})\psi \quad \text{and} \quad \delta\bar{\psi} = \alpha\bar{\psi}(1 - \frac{1}{2}aD_{ov})\gamma_5 \ , \tag{4.3}$$

ψ and $\bar{\psi}$ are the usual four component fermion and antifermion fields. For more than one fermion flavour, a flavour index is needed with the corresponding modification of the chiral transformations. Because of this invariance, which reduces to the usual definition of chirality in the continuum limit, a fermion action that has the same symmetries as continuum QCD can be formulated.

The expression for energy density and pressure can be obtained from the partition function, $Z = \det D_{ov}$, obtained by integrating the quark-antiquark fields :

$$\epsilon = \frac{T^2}{V}\left.\frac{\partial \ln Z(V,T)}{\partial T}\right|_V , \quad \text{and} \quad P = T\left.\frac{\partial \ln Z(V,T)}{\partial V}\right|_T ,$$

where the spatial volume $V = N^3a^3$ and the temperature $T = (N_T a_4)^{-1}$ for an $N^3 \times N_T$ lattice. Since these formulae require taking derivatives with respect to the temperature keeping the volume constant, it is convenient to formulate the theory on an anisotropic lattice with the spacing along the time and space directions taken to be a_t and a_s respectively. We restrict ourselves to $U = 1$ here to focus on the ideal gas limit. Noting that the sign function for a matrix can be defined in terms of its eigenvalues, the energy density can be written as

$$\epsilon = -\frac{1}{N^3a^3N_T}\left(\frac{\partial \ln(\prod_n \lambda_n)}{\partial a_4}\right)_a = -\frac{2}{N^3a^3N_T}\sum_{\lambda_\pm}\left(\frac{\partial \ln \lambda_\pm}{\partial a_4}\right)_a$$

where the chiral nature of the eigenvalue spectrum in the free case was used in the last line. The eigenvalues of the free overlap operator in the momentum space can be easily worked out [10] to be

$$\lambda_\pm = 1 - \frac{\mathrm{sgn}\left(\sqrt{h^2 + h_5^2}\right) h_5 \pm i\sqrt{h^2}}{\sqrt{h^2 + h_5^2}} \ , \tag{4.4}$$

where the variables h above are given by

$$\begin{aligned} h_5 &= M - \sum_{j=1}^{3}(1-\cos(ap_j)) - \frac{a}{a_4}(1-\cos(a_4p_4)) \\ h_j &= -\sin(ap_j) \qquad \text{where } j = 1,2,3 \\ h_4 &= -\frac{a}{a_4}\sin(a_4p_4) \\ h^2 &= h_1^2 + h_2^2 + h_3^2 + h_4^2 \ . \end{aligned} \tag{4.5}$$

From the (anti)periodic fermion boundary conditions in the (time) space directions, the discrete p_μ's appearing in the equations above are seen to have the following allowed values :

$$\begin{aligned} ap_j &= \frac{2n_j\pi}{N}, n_j = 0,..,(N-1), j = 1,2,3 \text{ and} \\ a_4p_4 &= \frac{(2n+1)\pi}{N_T}, n = 0,..,(N_T-1) \end{aligned} \tag{4.6}$$

Taking the appropriate derivatives with respect to a and a_4, the pressure and the energy density can be straightforwardly calculated.

4.3 Including the chemical potential

The chemical potential is usually introduced as the Lagrange multiplier to investigate thermodynamics at constant conserved number. Constructing the relevant number operator for the overlap Dirac fermions is not easy due to its nonlocality [11] and may even be not unique [12]. Instead of deriving the conserved number, an inspired guess for it such that it has the right continuum limit was made in [7]. The idea there was to introduce it in D_W as one would for the usual Wilson fermions:

$$D_{ov} = 1 + \gamma_5 \mathrm{sgn}(\gamma_5 D_W(\hat{\mu})) \ , \tag{4.7}$$

where the chemical potential $\hat{\mu} = \mu a_4$ appears only as multiplying factors $\exp(\hat{\mu})$ and $\exp(-\hat{\mu})$ to the links U_4 and $U_4^\dagger$ respectively in eq.(4.2). This, of course, renders $\gamma_5 D_W(\mu)$ to be non-hermitian, necessitating an extension of the usual definition of the sign function. The natural choice [7] was to use the sign of the real part of the eigenvalues of $\gamma_5 D_W(\mu)$ in the equation above. It is important to note that the extended sign function it is not defined for purely imaginary eigenvalues. Numerical simulations showed that [10] for an ideal gas of overlap fermions, the above way of introducing μ does not encounter any quadratic divergences at zero temperature. Such

divergences were known to arise [13, 14] for staggered and Wilson fermions, if μ was introduced naively as a coefficient of the conserved number. These were eliminated by the the choice of the $\exp(\pm\hat{\mu})$ factors. A more general way to introduce the chemical potential is to introduce functions $K(\hat{\mu})$ and $L(\hat{\mu})$ in place of the factors $\exp(\hat{\mu})$ and $\exp(-\hat{\mu})$ respectively such that $K(\hat{\mu}) = 1 + \hat{\mu} + \mathcal{O}(\hat{\mu}^2)$ and $L(\hat{\mu}) = 1 - \hat{\mu} + \mathcal{O}(\hat{\mu}^2)$. It was shown [15] that the quadratic divergences are avoided if $K(\hat{\mu}) \cdot L(\hat{\mu}) = 1$.

Here we follow that idea and introduce chemical potential in the overlap Dirac operator through the K and L factors in D_W and study the condition to eliminate the quadratic divergences. Introducing

$$\frac{K(\hat{\mu}) - L(\hat{\mu})}{2} = R\sinh\theta, \quad \frac{K(\hat{\mu}) + L(\hat{\mu})}{2} = R\cosh\theta$$

the eigenvalues can be easily recalculated. They can be written in terms of the h_i of eq.(4.5) but with h_4 and h_5 changed to :

$$\begin{aligned} h_5 &= M - \sum_{j=1}^{3}(1-\cos(ap_j)) - \frac{a}{a_4}(1 - R\cos(a_4p_4 - i\theta)) \\ h_4 &= -\frac{a}{a_4}R\sin(a_4p_4 - i\theta)\ . \end{aligned} \tag{4.8}$$

In the presence of a finite chemical potential, the energy density is defined as

$$\epsilon(\mu) = -\frac{1}{N^3a^3N_T}\left(\frac{\partial \ln\det D}{\partial a_4}\right)_{a,a_4,\mu} = -\frac{2}{N^3a^3N_T}\left(\frac{\partial\ln(\lambda_+\lambda_-)}{\partial a_4}\right)_{a,a_4,\mu} \tag{4.9}$$

For our purposes, we will assume that the sign function is unity for the finite μ case. For $\hat{\mu} = 0$, it is $+1$; while for large $\hat{\mu}$ it can become negative, depending on the M value. These issues are important in a numerical calculation of the approach to the continuum limit and is discussed in detail in [16, 17].

The energy density is obtained using eq.(4.9) and setting $a = a_4$. The full expression for the energy density is rather cumbersome and it is convenient to introduce the following compact notation:

$$h_5 = g + cos(\omega - i\theta), \qquad h^2 = f + \sin^2(\omega - i\theta), \qquad h^2 + h_5^2 = d + 2g\cos(\omega - i\theta), \tag{4.10}$$

where $\omega = ap_4$ and the functions g, f and d are given by

$$\begin{aligned} g &= M - 4 + b; \qquad b = \cos(ap_1) + \cos(ap_2) + \cos(ap_3); \qquad f = h_1^2 + h_2^2 + h_3^2; \\ d_R &= f + g^2 + R^2. \end{aligned} \tag{4.11}$$

The functions g, f and d_R only depend on the spatial momentum p_j and will be summed over. We will give explicit expressions for the thermodynamic quantities in terms of ω in the continuum limit. For lattices with finite N_T, ω_n will be used to denote the Matsubara frequencies. In terms of the functions defined above, the expression for the energy density is:

$$\begin{aligned} \epsilon a^4 &= \frac{2}{N^3 N_T} \sum_{p_j,n} \left[\frac{1 - R\cos(\omega_n - i\theta)}{d_R + 2gR\cos(\omega_n - i\theta)} + \frac{R^2 \sin^2(\omega_n - i\theta)(g + R\cos(\omega_n - i\theta))}{(d_R + 2gR\cos(\omega_n - i\theta))(f + R^2\sin^2(\omega_n - i\theta))} \right] \\ &\times \left[g + R\cos(\omega_n - i\theta) + \sqrt{d_R + 2gR\cos(\omega_n - i\theta)} \right] \\ &= \frac{2}{N^3 N_T} \sum_{p_j,n} F(R, \omega - i\theta). \end{aligned} \tag{4.12}$$

A similar straightforward evaluation for the pressure shows that the EOS for the ideal gas $\epsilon = 3P$ on the finite lattice also holds in the presence of a chemical potential. Furthermore, the number density at finite chemical potential can be computed using the definition:

$$n = \frac{1}{N^3 a^3 N_T} \left(\frac{\partial \ln \det D}{\partial \hat{\mu}} \right)_{a_4} \tag{4.13}$$

In terms of h's this can be calculated explicitly to give:

$$\begin{aligned} n a^3 &= \frac{-2i}{N^3 N_T} \sum_{p_j,n} [R\sin(\omega_n - i\theta) \times \left(\frac{gR\cos(\omega_n - i\theta) + R^2 + f}{(d_R + 2gR\cos(\omega_n - i\theta))(f + R^2\sin^2(\omega_n - i\theta))} \right) \\ &\times \left(g + R\cos(\omega_n - i\theta) + \sqrt{d_R + 2gR\cos(\omega_n - i\theta)} \right)] \\ &= \frac{-2i}{N^3 N_T} \sum_{p_j,n} F_N(R, \omega_n - i\theta) \ . \end{aligned} \tag{4.14}$$

4.3.1 $T = 0$ divergence cancellation

In order to obtain the condition for removing the divergences, we first calculate the energy density at zero temperature, i.e., for the limit $N_T \to \infty$ at finite a. The frequency sum $\frac{1}{N_T}\Sigma$ in eq.(4.12) gets replaced by the integral $\frac{1}{2\pi}\int_{-\pi}^{\pi} d\omega$. Subtracting the vacuum contribution corresponding to $\mu = 0$, i.e., $R = 1, \theta = 0$, the energy

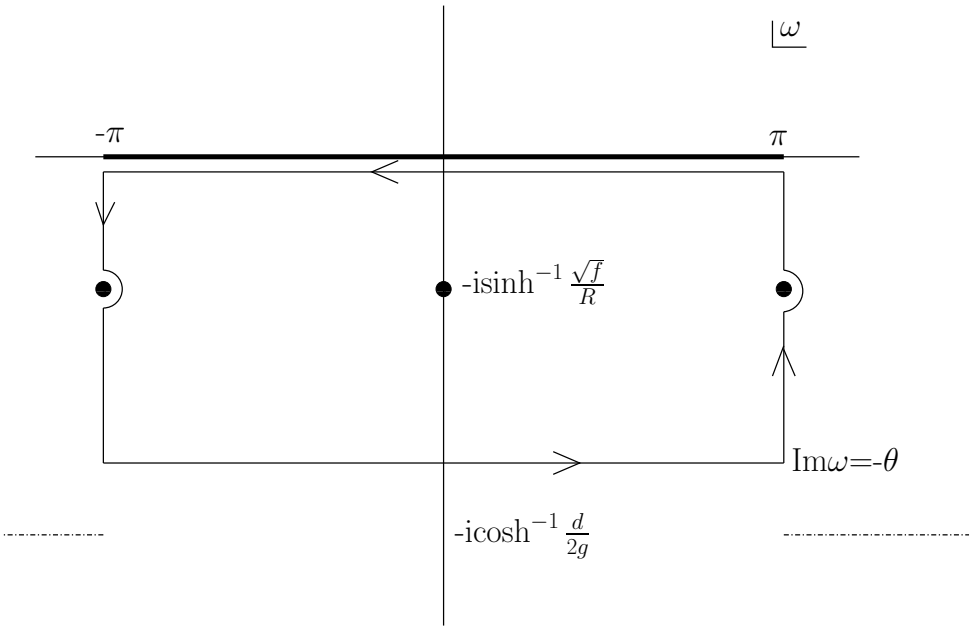

Figure 4.1: Contour chosen for evaluating the energy density and the number density for nonzero of chemical potential at zero temperature. The thick line indicates the Matsubara frequencies while the filled circles denote the poles of $F(R,\omega)$. The dashed lines are the branch cuts due to the presence of the square root in the integrand.

density at zero temperature is given by

$$\epsilon a^4 = \frac{1}{\pi N^3}\sum_{p_j}\left[\int_{-\pi}^{\pi} F(R,\omega-i\theta)d\omega - \int_{-\pi}^{\pi} F(\omega)d\omega\right]. \tag{4.15}$$

Choosing the contour shown in Figure 4.1, the expression above can be evaluated in the complex ω-plane as

$$\begin{aligned}\epsilon a^4 &= \frac{1}{\pi N^3}\sum_{p_j}\left[2\pi i\sum_i \text{Res } F(R,\omega_i) - \int_{\pi-i\theta}^{\pi} F(R,\omega)d\omega - \int_{\pi}^{-\pi} F(R,\omega)d\omega\right.\\ &- \left.\int_{-\pi}^{-\pi-i\theta} F(R,\omega)d\omega - \int_{-\pi}^{\pi} F(\omega)d\omega\right].\end{aligned} \tag{4.16}$$

The second and fourth terms cancel since F is an even function which satisfies $F(\pi+i\eta) = F(-\pi+i\eta)$. Hence, we obtain

$$\epsilon a^4 = \frac{1}{\pi N^3}\sum_{p_j}\left[2\pi R_3\Theta\left(\frac{K(\hat{\mu})-L(\hat{\mu})}{2}-\sqrt{f}\right) + \int_{-\pi}^{\pi} F(R,\omega)d\omega - \int_{-\pi}^{\pi} F(\omega)d\omega\right], \tag{4.17}$$

where -iR_3 is the residue of the function $F(R,\omega)$ at the pole $-i\,\sinh^{-1}(\sqrt{f}/R)$ and is given by

$$R_3 = \frac{\sqrt{f}(g+\sqrt{f+R^2}+\sqrt{d_R+2g\sqrt{f+R^2}})}{2\sqrt{f+R^2}(d_R+2g\sqrt{f+R^2})} \times (g+\sqrt{f+R^2})\ . \tag{4.18}$$

Noting that the number density in eq.(4.14) has the same pole structure as the energy density, with only the residues being different in the two cases, the latter can also be calculated in the same way to obtain,

$$na^3 = \frac{1}{\pi N^3}\sum_{p_j}\left[2\pi R_4\Theta\left(\frac{K(\hat{\mu})-L(\hat{\mu})}{2}-\sqrt{f}\right)-i\int_{-\pi}^{\pi}F_N(R,\omega)d\omega+i\int_{-\pi}^{\pi}F_N(\omega)d\omega\right], \tag{4.19}$$

where R_4 is the residue of the function $F_N(\omega)$ at the pole $-i\,\sinh^{-1}(\sqrt{f}/R)$ given by,

$$R_4 = \frac{(g+\sqrt{f+R^2}+\sqrt{d_R+2g\sqrt{f+R^2}})}{2\sqrt{f+R^2}(d_R+2g\sqrt{f+R^2})} \times (g\sqrt{R^2+f}+R^2+f)\ .$$

It is clear from both eqs.(4.17) and (4.19) that the condition $R=1$ cancels the two integrals in each of them, yielding the canonical forms of the Fermi surface. For $R\neq 1$, there will in general be violations of the Fermi surface on the lattice. Moreover, in the continuum limit $a\to 0$, one will in general have the μ^2/a^2 and μ/a^2-divergences for $R\neq 1$ in the energy density and the number density respectively. The condition to obtain the correct continuum values of $\epsilon=\mu^4/4\pi^2$ and $n=\mu^3/3\pi^2$ can also be seen to be the expected $K(\hat{\mu})-L(\hat{\mu})=2\hat{\mu}+O(\hat{\mu}^2)$. Note that the earlier work [15] on staggered fermions employed the exact number density on the lattice which is not the case for the overlap fermions here. That one obtains still identical conditions in both the cases suggests that it is indeed the behaviour near the continuum limit which dictates these conditions.

4.3.2 Energy density at $T\neq 0$ and $\mu\neq 0$

In this sub-section, we outline the procedure to calculate the energy density on a finite lattice using the techniques of contour integration. For this calculation, we revert back to the choice $K(\hat{\mu})=\exp(\hat{\mu})$ and $L(\hat{\mu})=\exp(-\hat{\mu})$ which has $R=1$ and $\theta=\hat{\mu}$. The physical part of the energy density on the lattice is calculated by

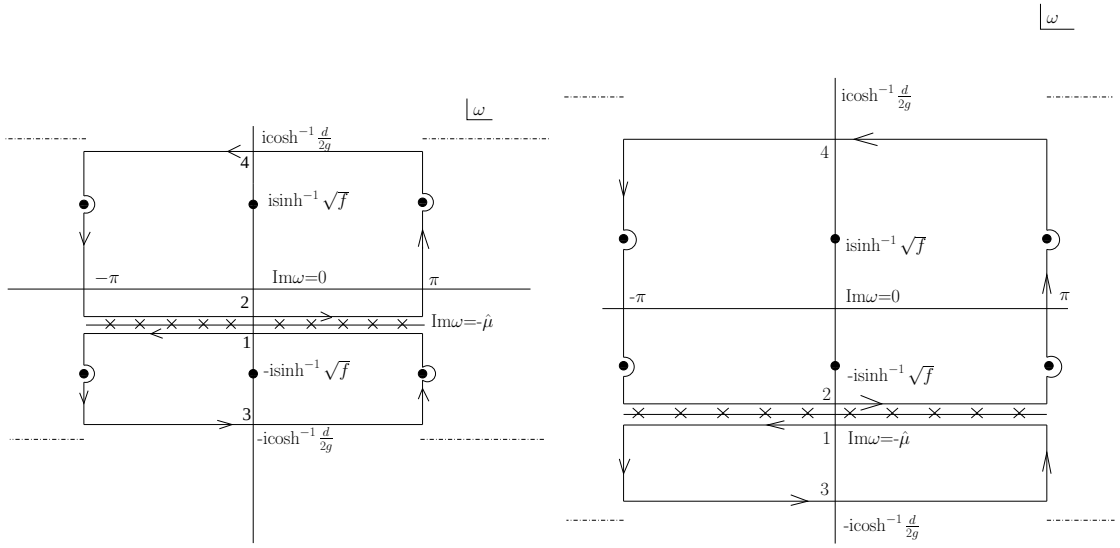

Figure 4.2: The contours chosen for evaluation of the $\omega-$ sum for $\hat{\mu} < \sinh^{-1}\sqrt{f}$ (left) and for $\hat{\mu} < \sinh^{-1}\sqrt{f}$ (right).

subtracting off the $\hat{\mu} = 0$, $T = 0$ contribution, and is given by:

$$\epsilon a^4 = \sum_{p_j} \frac{1}{N^3} \left[\frac{2}{N_T} \sum_n F(\omega_n - i\hat{\mu}) - \frac{1}{\pi} \int_{-\pi}^{\pi} F(\omega) d\omega \right]. \tag{4.20}$$

The further evaluation of the energy density using contour methods can be done, noting that compared to the Figure 4.1, there are two major differences. Due to the finiteness of the lattice, there are only N_T Matsubara frequencies, $(2n+1)\pi/N_T$. Moreover, they are displaced along the imaginary axis by $i\hat{\mu}$ in the lower half plane with the choice of the function $1/(\exp[i(\omega + i\hat{\mu})N_T] + 1)$. The frequency sum can be replaced by line integrals as,

$$\frac{2\pi}{N_T} \sum_n F(\omega_n - i\hat{\mu}) \;\; = \;\; \int_{\pi - i\epsilon - i\hat{\mu}}^{-\pi - i\epsilon - i\hat{\mu}} \frac{F(\omega) d\omega}{e^{i(\omega + i\hat{\mu})N_T} + 1} + \int_{-\pi + i\epsilon - i\hat{\mu}}^{\pi + i\epsilon - i\hat{\mu}} \frac{F(\omega) d\omega}{e^{i(\omega + i\hat{\mu})N_T} + 1} \tag{4.21}$$

Further, the choice of the contour will depend on whether the pole $\omega = -i \sinh^{-1}\sqrt{f}$ is above or below the Im$\omega = -\hat{\mu}$ line. The two cases are illustrated in fig 4.2.

Therefore the frequency sum can be split into two terms,

$$\sum_n F(\omega_n - i\hat{\mu}) = \sum_n \left[F_<(\omega_n - i\hat{\mu}) + F_>(\omega_n - i\hat{\mu}) \right], \tag{4.22}$$

where $F_>$ and $F_<$ are the functions with $\sinh^{-1}\sqrt{f} < \hat{\mu}$ ($\sinh^{-1}\sqrt{f} > \hat{\mu}$) respectively.

We have taken $\hat{\mu} < \cosh^{-1}\frac{d}{2g}$ because we expect that in the continuum limit the $\hat{\mu}$ to scale as the lattice spacing whereas the second term to tend to infinity. The second integral in eq.(4.21) can be written in terms of other line integrals:

$$\frac{2\pi}{N_T}\sum_n F_<(\omega_n - i\hat{\mu}) = \Theta(\sinh^{-1}\sqrt{f} - \hat{\mu}) \times \left(-2\pi i \sum_{\mathrm{Im}\omega>0} \frac{\mathrm{Res}\ F(\omega)}{\mathrm{e}^{-i(\omega+i\hat{\mu})N_T}+1} \right.$$
$$\left. + \ 2\pi i \sum_{\mathrm{Im}\omega<0} \frac{\mathrm{Res}\ F(\omega)}{\mathrm{e}^{i(\omega+i\hat{\mu})N_T}+1} - \int_3 \frac{F(\omega)}{\mathrm{e}^{i(\omega+i\hat{\mu})N_T}+1}d\omega + \int_4 \frac{F(\omega)}{\mathrm{e}^{-i(\omega+i\hat{\mu})N_T}+1}d\omega + \int_{-\pi}^{\pi} F(\omega)d\omega \right). \tag{4.23}$$

The expression can be evaluated by substituting the value of the residue of the function $F(\omega)$ at the poles $\omega = \pm i\sinh^{-1}\sqrt{f}$, which is denoted as R_1 (and $R_1 = \frac{\sqrt{f}}{2\sqrt{1+f}}$). The integrals 3 and 4 are along the lines Im $\omega = \mp(\sinh^{-1}\sqrt{f} + \eta)$. Representing them as $\epsilon_{3\mu,4\mu}$ respectively, we get

$$\frac{2\pi}{N_T}\sum_n F_<(\omega_n - i\hat{\mu}) = \Theta(\sinh^{-1}\sqrt{f} - \hat{\mu}) \times \left(\frac{4\pi\ R_1}{\mathrm{e}^{(\sinh^{-1}\sqrt{f}+\hat{\mu})N_T}+1} + \frac{4\pi\ R_1}{\mathrm{e}^{(\sinh^{-1}\sqrt{f}-\hat{\mu})N_T}+1} \right.$$
$$\left. + \int_{-\pi}^{\pi} F(\omega)d\omega + \epsilon_{3\mu} + \epsilon_{4\mu} \right). \tag{4.24}$$

Similarly for $\hat{\mu} > \sinh^{-1}\sqrt{f}$ the frequency sum is replaced by integrals along the contour as shown in the right panel of Figure 4.2. There are no poles below the Im $\omega = -\hat{\mu}$ line, so the first integral in eq.(4.21) can be replaced by a line integral along the line 3. Following the same steps as discussed for the above case, the frequency sum reduces to

$$\frac{2\pi}{N_T}\sum_n F_>(\omega_n - i\hat{\mu}) = \Theta(\hat{\mu} - \sinh^{-1}\sqrt{f}) \times \left(\frac{4\pi\ R_1}{\mathrm{e}^{(\sinh^{-1}\sqrt{f}-\hat{\mu})N_T}+1} + \frac{4\pi\ R_1}{\mathrm{e}^{(\sinh^{-1}\sqrt{f}+\hat{\mu})N_T}+1} \right.$$
$$\left. + \int_{-\pi}^{\pi} F(\omega)d\omega + \epsilon_{3\mu} + \epsilon_{4\mu} \right) . \tag{4.25}$$

Finally, the energy density on the lattice is obtained from eq.(4.20) by substituting in the eq.(4.22) the frequency sums calculated above:

$$\epsilon a^4 = \frac{2}{N^3}\sum_{p_j}\left[\frac{\sqrt{f}}{\sqrt{1+f}}\frac{1}{\mathrm{e}^{(\sinh^{-1}\sqrt{f}-\hat{\mu})N_T}+1} + \frac{\sqrt{f}}{\sqrt{1+f}}\frac{1}{\mathrm{e}^{(\sinh^{-1}\sqrt{f}+\hat{\mu})N_T}+1} + \epsilon_{3\mu} + \epsilon_{4\mu} \right]. \tag{4.26}$$

In the continuum limit the terms $\epsilon_{3\mu,4\mu}$ vanish leaving only the contribution due to

the residues of the poles. It can be shown explicitly that the expression for the lattice energy density reduces to the well known [19] result in the continuum.

$$\epsilon = \frac{2}{(2\pi)^3}\int \frac{E\ \prod_{j=1}^{3} dp_j}{1+\mathrm{e}^{\frac{E+\mu}{T}}} + \frac{2}{(2\pi)^3}\int \frac{E\ \prod_{j=1}^{3} dp_j}{1+\mathrm{e}^{\frac{E-\mu}{T}}}. \tag{4.27}$$

This procedure can be straightforwardly repeated for the calculation of the number density for the overlap fermions and consequently show that the standard continuum is obtained.

4.4 Discussion and Summary

Investigating the thermodynamics of QCD on lattice with fermions which possess both the chiral symmetry and the flavour symmetry relevant to our world has important consequences for both the experimental aspects of the heavy ion collisions and the theoretical aspects of the $\mu - T$ phase diagram. Staggered fermions used in the bulk of the work so far are not adequate to resolve some of these issues. Overlap fermions, while computationally more expensive, may prove better in such studies in near future. In this chapter, we have demonstrated that a generalized version of the action proposed for non-zero μ [7], avoids a^{-2} divergences in thermodynamic quantities provided that certain conditions are met, and gives the correct expressions for the thermodynamic quantities on the finite lattice, as well as in the continuum limit.

References

[1] M. Golterman Applications of chiral perturbation theory to lattice QCD Lectures delivered at the Ecole de Physique des Houches "Modern perspectives in lattice QCD" arXiv: 0912.4042

[2] R. Narayanan and H. Neuberger *Phys. Rev. Lett.* 71 3251(1993)

[3] R. V. Gavai and S. Gupta *Phys.Rev.* D67 (2003) 034501

[4] D. Banerjee, R. V. Gavai and S. Gupta *Phys. Rev.* D83, 074510 (2011)

[5] E. Laermann and P. Schmidt *Eur. Phys. J.* C20 (2001) 541

[6] R. V. Gavai, S. Gupta and R. Lacaze *Phys. Rev.* D78, 014502,2008

[7] J. Bloch and T. Wettig *Phys. Rev. Lett.* 97, 012003 (2006)

[8] P. H. Ginsparg and K. G. Wilson *Phys. Rev.* D 25, 2649 (1982)

[9] M. Lüscher *Phys. Lett.* B 428 342 (1998)

[10] C. Gattringer and L. Liptak *Phys. Rev.* D76, 054502 (2007)

[11] Y. Kikukawa and A. Yamada arXiv : hep-lat/9810024;
P. Hasenfratz et al. *Nucl. Phys.* B643, 280 (2002)

[12] J. E. Mandula arXiv: 0712.0651

[13] P. Hasenfratz and F. Karsch *Phys. Lett.* 125B, 308 (1983)

[14] N. Bilic and Rajiv V. Gavai *Z. Phys.* C23, 77 (1984)

[15] R. V. Gavai *Phys. Rev.* D32, 519 (1985)

[16] D. Banerjee, R. V. Gavai and S. Sharma *Phys. Rev.* D 78, 014506 (2008)

[17] Sayantan Sharma Ph.D. thesis

[18] D. Banerjee, R. V. Gavai and S. Sharma **PoS LATTICE** 2008:177,2008

[19] H. J. Rothe *Lattice Gauge Theories: An introduction* World Scientific, Second edition(1998)

Chapter 5

XY model with a finite chemical potential

5.1 Introduction

Understanding the phase diagram of quantum chromodynamics (QCD) as a function of temperature T and baryon chemical potential μ is an active area of research. Although much is known about the physics at $\mu = 0$ from lattice QCD calculations [1, 2], there are various proposals of what might occur at non-zero μ and small values of T [3, 4, 5]. Due to the sign problem, which arises in all current formulations of lattice QCD at non-zero μ, it is impossible to perform first principles calculations of the system. Most of our knowledge of the (T, μ) phase diagram of QCD is based on models that are motivated from universality and solved using mean field theory. In certain regions of the phase diagram it should be possible to construct bosonic effective field theory models that share the same symmetries, low energy physics and possibly the phase transitions as QCD. It would be interesting to study these models from first principles. Unfortunately, sign problems also arise in bosonic field theories in the presence of a chemical potential when formulated in the conventional approach. For this reason not many first principles studies of field theories with a chemical potential exist. However, some of these sign problems are solvable today and thus allow us to explore the physics of a chemical potential from first principles. It may be useful to study these simpler field theories before attempting to study QCD.

One of the simplest examples of a relativistic bosonic field theory is the classical non-linear $O(2)$ sigma model on a cubic lattice which has been studied extensively in the context of superfluid transitions using the efficient Wolff cluster algorithm [6]. The phase transition is between two phases: an $O(2)$ symmetric phase and a phase

where the symmetry is spontaneously broken. Close to the phase transition, the low energy physics is described by an interacting quantum field theory of massive charged bosons in the symmetric phase and of massless Goldstone bosons in the broken phase. At the critical point the low energy physics is scale invariant and the critical behavior belongs to the three dimensional XY universality class.

Since the model contains an exact $O(2)$ global symmetry, one can also introduce a chemical potential μ that couples to the corresponding conserved charge. This chemical potential helps one study the "condensed matter" composed of the fundamental boson present in the theory. When $\mu \neq 0$, the action in the conventional formulation becomes complex and Monte Carlo algorithms suffer from a sign problem exactly like in QCD. Not surprisingly, the phase diagram of the condensed matter arising in the $O(2)$ non-linear sigma model has not been studied from first principles. On the other hand non-relativistic bosonic lattice models, especially in the Hamiltonian formulation have been studied for many years by the condensed matter community. Here one naturally constructs the field theory with bosonic world lines and there is no sign problem when one introduces a chemical potential. Thus, it is natural that a world-line approach could solve the corresponding sign problem even for a relativistic field theory. This was shown explicitly for both the linear sigma model [7] and the $O(2)$ non-linear sigma model [8].

In this chapter, we will present the first non-perturbative calculation of the phase diagram of the non-linear $O(2)$-sigma model in three dimensions at low temperatures in the $\beta - \mu$ plane, where β is the coupling and μ is the chemical potential. In order to simulate the constrained system formulated as a world-line of bosonic particles, we have adapted the *worm algorithm* for our model. The introduction of this highly efficient Monte Carlo algorithm [9] has drastically improved our ability to simulate constrained systems. Variants of this algorithm in the name of *directed loop algorithm* [10, 11] have been used to solve a variety of models that arise in the strong coupling limit of lattice gauge theories [12, 13, 14, 15]. The worm algorithm has also been found to be an efficient approach to study a wider class of fermionic field theories in the loop representation in two dimensions where fermion sign problems are absent [16, 17, 18, 19] and weak coupling Abelian lattice gauge theory [20].

5.2 Model and Observables

The action of the $O(2)$ non-linear sigma model on a lattice with a finite chemical potential that we study here is given by

$$S = -\beta \sum_{x,\alpha} \Big\{ \cos(\theta_x - \theta_{x+\alpha} - i\mu\delta_{\alpha,t}) \Big\}, \tag{5.1}$$

where x is the lattice site on a three dimensional cubic lattice, $\alpha = 1, 2$ represent the spatial directions and $\alpha = t$ represents the temporal direction. We will use L to represent the spatial size and L_t the temporal size and assume periodic boundary conditions. The constant β plays the role of the coupling. The chemical potential μ is introduced in the standard way and couples to the conserved charge of the global $O(2)$ symmetry [21]. When $\mu \neq 0$ the action becomes complex and Monte Carlo algorithms to generate configurations $[\theta]$ that contribute to the partition function

$$Z = \int [d\theta_x] \mathrm{e}^{-S}, \tag{5.2}$$

suffer from a sign problem. In particular the Wolff cluster algorithm [6] is no longer useful at non-zero chemical potential. Hence the phase diagram of the model in the (β, μ) plane remains unexplored.

It is possible to avoid the sign problem if we rewrite the partition function in the world-line representation [8]. Using the identity

$$\exp\{\beta \cos\theta\} = \sum_{k=-\infty}^{\infty} I_k(\beta) e^{ik\theta}, \tag{5.3}$$

where I_k is the modified Bessel function of the first kind, on each bond (x, α), and performing the angular integration over θ_x the partition function can be rewritten as

$$Z = \sum_{[k]} \prod_{x} \Big\{ I_{k_{x,\alpha}}(\beta) e^{\mu\delta_{\alpha,t} k_{x,\alpha}} \Big\} \; \delta\Big(\sum_{\alpha} (k_{x,\alpha} - k_{x-\alpha,\alpha}) \Big), \tag{5.4}$$

where the bond variables $k_{x,\alpha}$ describe "world-lines" or "current" of particles moving from lattice site x to the site $x + \hat{\alpha}$ and take integer values. A configuration of these bond variables, denoted by $[k]$, is thus a world-line configuration. The global $U(1)$ symmetry of the model is manifest in the local current conservation relation represented by the delta function. In other words any particle that comes into the site must leave the site due to current conservation. In this world-line formulation the partition function is a sum over explicitly positive terms even in the presence of

μ. Details of the "worm algorithm" that we have developed to update the world-line configuration $[k]$ is described in appendix A.

We focus on four observables in this work:

1. The average particle density ρ:

$$\rho = \frac{1}{L^2}\langle \sum_{x\in\text{timeslice}} k_{x,t}\rangle. \tag{5.5}$$

   The average particle number is then given by $\langle N\rangle = \rho L^2$.

2. The particle number susceptibility κ:

$$\kappa = \frac{1}{L^2 L_t}\langle \left(\sum_x k_{x,t}\right)^2 \rangle. \tag{5.6}$$

   Note that $\kappa = L_t/L^2\langle N^2\rangle$.

3. The superfluid density (or particle current susceptibility) ρ_s:

$$\rho_s = \frac{1}{2L^2 L_t}\langle \sum_{\alpha=1,2} \left(\sum_x k_{x,\alpha}\right)^2 \rangle. \tag{5.7}$$

   The superfluid density is known to be $\rho_s = 1/L_t\langle W^2\rangle$ where W is the spatial winding number of particles [22]. We define $\langle N_s\rangle = L^2\rho_s$ as the number of particles that are in the superfluid phase in a finite system.

4. The condensate susceptibility χ:

$$\chi = \sum_y \langle \mathrm{e}^{i\theta_x}\mathrm{e}^{-i\theta_y}\rangle. \tag{5.8}$$

The first three observables are "diagonal" observables and can be measured on each world-line configuration and then averaged. The condensate susceptibility χ on the other hand is a "non-diagonal" observable, but it can be related to the size of each worm update as discussed in appendix A. We discuss some tests of the algorithm in appendix A.

At $\mu = 0$, the model has a second order phase transition at $\beta_c = 0.45421$. For $\beta > \beta_c$ the $O(2)$ symmetry is spontaneously broken, while for $\beta < \beta_c$ the model is in the symmetric phase.

5.3 Finite Size Effects

A good understanding of finite size effects is important for extracting thermodynamic results from numerical computations. This is particularly true close to a second order critical point where correlation lengths diverge. While developing a theory of finite size effects, one usually assumes $L_t = L^z$ where z is called the dynamical critical exponent of the problem. Such a choice makes calculations natural. In a relativistic theory since $z = 1$, it is natural to choose $L_t = L$. Most studies of the critical behavior at $\beta = \beta_c$ and $\mu = 0$ make use of this choice. On the other hand, in the presence of a chemical potential, since the low energy effective theory is non-relativistic, one expects $z = 2$ and $L_t = L^2$ is a more natural choice. However, in our work we have found that even with this choice the finite size effects close to the critical point are non-trivial in the presence of a chemical potential. In fact observables always show clear "wiggles" and cannot be fit to a simple power law that one expects near the critical point. In order to demonstrate this feature, in Fig. 5.1 we plot the behavior of the average particle density ρ as a function of μ for $L = 12$ and $L_t = 144$ at $\beta = 0.43$. From mean field theory we expect

$$\rho \approx \begin{cases} c(\mu - \mu_c) & \mu > \mu_c \\ 0 & \mu < \mu_c \end{cases} \tag{5.9}$$

close to $\mu = \mu_c$ in the thermodynamic limit. In Fig. 5.1 we observe that ρ is indeed zero for $\mu < 0.27$ and begins to increase for $\mu \gtrsim 0.27$. But the increase, although roughly linear close to μ_c as expected, shows clear "wiggles" when $0.27 < \mu < 0.38$ and only for $\mu > 0.38$ the "wiggles" disappear. The region between $0.27 < \mu < 0.38$ has been enlarged in the left inset in order to enhance the observed "wiggles". In the right inset we fix $\mu = 0.32$ and plot ρ as a function of L assuming $L_t = L^2$. Again the data shows clear oscillations whose origin may seem a bit mysterious. In order to avoid these oscillations one has to go to much larger L at a fixed value of μ. However, since L_t scales like L^2 going to larger lattice sizes is more difficult than in a relativistic theory. For this reason, we believe it may be useful to develop a different type of finite size analysis.

As we will argue below, the strange finite size behavior is the result of energy levels crossing each other due to the chemical potential. Since the particle number is a conserved quantum number, energy levels with different particle numbers can cross each other at critical values of the chemical potential. Similarly at a fixed chemical potential, the changes in spatial size can also cause these energy levels to cross each other. These level crossings lead to singularities at low temperatures (large L_t) in a

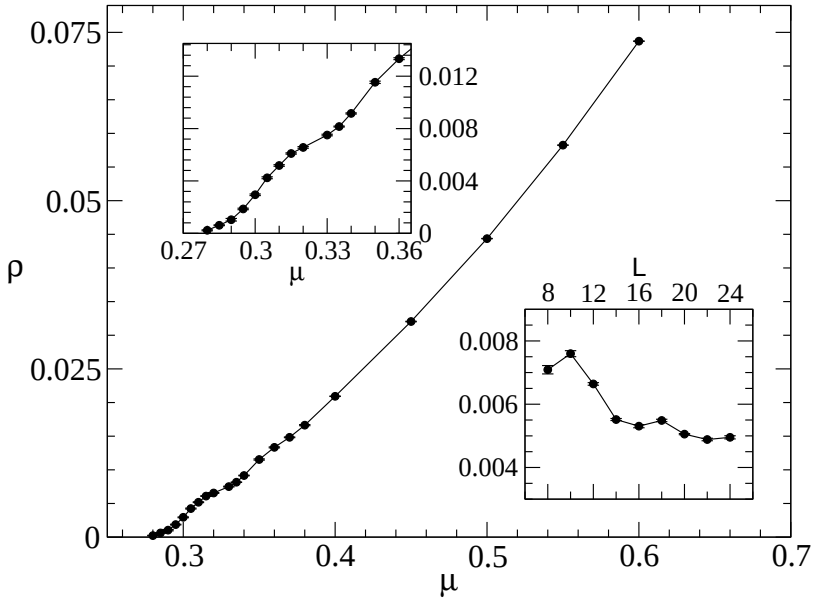

Figure 5.1: Plot of ρ as a function of μ for $\beta = 0.43$, $L = 12$ and $L_t = 144$. The data shows clear "wiggles" at small values of ρ which disappears for larger values. The left inset magnifies the region of the "wiggles". The right inset shows the plot of ρ as function of L at $\mu = 0.32$ assuming $L_t = L^2$ which also shows clear non-monotonic behavior.

finite spatial volume (fixed L). While these singularities are smoothed out at finite L_t, they leave behind non-trivial finite size effects observed above. While it may still be possible to develop practically useful finite size scaling relations using $L_t = L^2$, we find it natural to consider a finite size scaling theory for quantities as a function of L_t and μ for a fixed value of L close to the critical values of μ where energy levels cross each other. As we discuss below this leads to an effective quantum mechanics problem. The finite size effects studied here have been observed earlier in the context of quantum spin-systems in a magnetic field [10], but they were not analyzed using the techniques we introduce below.

5.4 Effective Quantum Mechanics

At a fixed value of L for sufficiently large L_t, it must be possible to map the lattice field theory problem to an effective quantum mechanics problem where only a few low energy levels play an important role. Let us label these energy levels by $|N, k\rangle$ and the energy eigenvalues by $E_k^{(N)}$, where $N = 0, 1, 2, ...$ represents the particle number

sector of the energy level and k represents "other" quantum numbers. The levels and the energies depend on L and β. The partition function of the problem may be written as

$$Z = \sum_{k,N} \mathrm{e}^{-(E_k^N - \mu N)L_t}. \tag{5.10}$$

Using this effective quantum mechanical description we can in principle find the L_t and μ dependence of various quantities. However, for the analysis to be practically useful we need to assume that only a few energy levels are important. If we assume that μ is close to a critical value μ_c where level crossing phenomena occurs, then for large enough L_t one might expect the physics to be dominated by just two levels. In this approximation we will derive the L_t and μ dependence of all our observables.

In a given particle number sector, we can assume $E_0^{(N)} < E_1^{(N)} < E_2^{(N)} < ...$ without loss of generality. However, in this work we will also assume that $E_0^{(0)} < E_0^{(1)} < E_0^{(2)}...$ which means that it always costs energy to add a particle into the system. While this is not necessary it is precisely the situation we encounter in this work and simplifies our analysis. With these assumptions it is easy to argue that close to the critical chemical potential where the particle number changes from N to $N+1$ we can approximate the partition function to be

$$Z \approx \mathrm{e}^{-(E_0^{(N)} - \mu N)L_t} + \mathrm{e}^{-(E_0^{(N+1)} - \mu(N+1))L_t}. \tag{5.11}$$

Here we have assumed all higher energy states will be suppressed exponentially at large L_t. It is easy to verify that $\mu_c^{(N)} \equiv E_0^{(N+1)} - E_0^{(N)}$ is the critical chemical potential where the average particle number changes from N to $N+1$. Below we discuss the L_t and μ dependence of each observable when $\mu \approx \mu_c^{(N)}$.

Particle Number

We first consider the average particle number $\langle N \rangle$. When $\Delta_\mu^{(N)} = \mu - \mu_c^{(N)}$ is small and L_t is large we can write

$$\langle N \rangle = \frac{N + (N+1)\mathrm{e}^{\Delta_\mu^{(N)} L_t}}{1 + \mathrm{e}^{\Delta_\mu^{(N)} L_t}}. \tag{5.12}$$

We will demonstrate later that our data fits very well to this simple one parameter fit and we are able to extract $\mu_c^{(N)}$ very accurately for all $L \leq 20$ for a variety of values of β.

Number Susceptibility

Next we discuss the number susceptibility $\kappa = L_t/L^2\langle N^2\rangle$. We now obtain

$$\langle N^2\rangle = \frac{N^2 + (N+1)^2 e^{\Delta_\mu^{(N)} L_t}}{1 + e^{\Delta_\mu^{(N)} L_t}}. \tag{5.13}$$

The value of $\mu_c^{(N)}$ is the same as obtained from the average particle number. So this observable has no new free parameters.

Superfluid Density

In the effective quantum mechanical description the superfluid density is given by

$$\rho_s \;=\; \frac{1}{Z}\int_0^{L_t} dt\ \mathrm{Tr}\left(\mathrm{e}^{-(L_t-t)\ H} O^\dagger \mathrm{e}^{-t\ H} O\right), \tag{5.14}$$

where

$$O = \frac{1}{L}\sum_{x_2} J_1(x_1, x_2) \tag{5.15}$$

is an operator in the Hilbert space made up of the conserved current operator $J_i(x_1, x_2)$ in the direction i at the site with coordinates (x_1, x_2). Note the sum is over the surface perpendicular to the direction of the current. Since it is a conserved current it does not matter which surface one chooses. Now if we introduce a complete set of energy eigenstates we get

$$\rho_s = \frac{1}{Z}\ \sum_{n,k} \mathrm{e}^{-(E_k^{(n)} - n\mu)L_t} \sum_{n'k'} |\langle n,k|O|n'k'\rangle|^2 \frac{\left(1 - \mathrm{e}^{-(E_{k'}^{(n')} - E_k^{(n)} - (n'-n)\mu)L_t}\right)}{(E_{k'}^{(n')} - E_k^{(n)} - (n'-n)\mu)}. \tag{5.16}$$

First we note that $\langle n,k|O|n'k'\rangle \propto \delta_{nn'}$, since the current operator commutes with the particle number operator and hence does not change the particle number. Further, as before we assume only two low lying energy levels are important in the partition function when $\mu \approx \mu_c^{(N)}$. Then the $[k,n]$ sum is replaced by $k = 0$ and $n = N, N+1$. Hence we obtain

$$\rho_s = \frac{\rho_0 + \rho_1 \mathrm{e}^{\Delta_\mu^{(N)} L_t}}{(1 + \mathrm{e}^{\Delta_\mu^{(N)} L_t})}, \tag{5.17}$$

where

$$\rho_0 = \sum_{k' \neq 0} |\langle N,0|O|Nk'\rangle|^2 \frac{\left(1 - \mathrm{e}^{-\Delta E^{(N)}_{k'} L_t}\right)}{\Delta E^{(N)}_{k'}}, \quad \text{with } \Delta E^{(N)}_{k'} \equiv E^{(N)}_{k'} - E^{(N)}_0. \tag{5.18}$$

and ρ_1 is obtained by replacing N with $N+1$ in the above expression. Note that the sum over k' does not contain the $k' = 0$ sum because $\langle N,0|O|N0\rangle = 0$ since O is a current operator and the ground state is rotationally invariant. Thus, the expression for ρ_s contains two new parameters since $\mu_c^{(N)}$ has already been encountered before.

Condensate Susceptibility

The expression for the condensate susceptibility can also be obtained using eq.(5.16) if the operator O is replaced by

$$O = \frac{2}{L} \sum_x cos(\theta_{x,t}). \tag{5.19}$$

The matrix element $\langle n,k|O|n'k'\rangle$ is non-zero only when $n' = n+1$ or $n' = n-1$. When $\mu \approx \mu_c^{(N)}$, the $[k,n]$ sum is again dominated by $E_0^{(N)}$ and $E_0^{(N+1)}$. However, in the present case the μ dependence also enters the k' sum. In the limit as $\Delta_\mu^{(N)} \to 0$ and $L_t \to \infty$ the $k' = 0$ term is singular while the other terms are not. Separating the singular term from others we find

$$\begin{aligned}
\chi &= 2|\langle N,0|O|N+1,0\rangle|^2 \frac{(\mathrm{e}^{\Delta_\mu^{(N)} L_t} - 1)}{\Delta_\mu^{(N)}(1 + \mathrm{e}^{\Delta_\mu^{(N)} L_t})} \\
&+ \frac{1}{(1 + \mathrm{e}^{\Delta_\mu^{(N)} L_t})} \sum_{k' \neq 0} |\langle N,0|O|N+1,k'\rangle|^2 \frac{(1 - \mathrm{e}^{-(\Delta E^{(N+1)}_{k'} - \Delta_\mu^{(N)}) L_t})}{(\Delta E^{(N+1)}_{k'} - \Delta_\mu^{(N)})} \\
&+ \frac{\mathrm{e}^{\Delta_\mu^{(N)} L_t}}{(1 + \mathrm{e}^{\Delta_\mu^{(N)} L_t})} \sum_{k' \neq 0} |\langle N+1,0|O|N,k'\rangle|^2 \frac{(1 - \mathrm{e}^{-(\Delta E^{(N)}_{k'} + \Delta_\mu^{(N)}) L_t})}{(\Delta E^{(N)}_{k'} + \Delta_\mu^{(N)})}.
\end{aligned} \tag{5.20}$$

Since $|\Delta_\mu^{(N)}|$ is assumed to be much smaller than all $\Delta E^{(N)}_{k'}$ and $\Delta E^{(N+1)}_{k'}$, at large L_t the exponentials in the k' sum can be dropped. If the remaining terms are expanded in powers of $\Delta_\mu^{(N)}$ we find

$$\chi = \frac{\chi_0(\mathrm{e}^{\Delta_\mu^{(N)} L_t} - 1)/\Delta_\mu^{(N)} + (\chi_1 + \chi_2 \Delta_\mu^{(N)} + ...) + (\chi_1' + \chi_2' \Delta_\mu^{(N)} + ...)\mathrm{e}^{\Delta_\mu^{(N)} L_t}}{(1 + \mathrm{e}^{\Delta_\mu^{(N)} L_t})}. \tag{5.21}$$

We find that our data fits well to this expression truncated at the quadratic order in $\Delta_\mu^{(N)}$, which means we have seven new parameters in our fit. However, most of these parameters are not determined reliably and contain large systematic errors. The only parameter that can be determined reliably is χ_0 and this is what we quote as a result from our analysis.

5.5 Results

We have performed extensive calculations at $\beta = 0.43, 0.50$ and 0.20. These values of β are chosen so that two of them are close to the critical coupling $\beta_c = 0.45421$ on either side and one is far from it in the massive (disordered) phase. In this section we present fits of our results to the effective quantum mechanics description discussed above. As mentioned earlier, the effective description becomes useful only in the limit of small temperatures where excitations to higher energy levels can be neglected. Since the spacing between energy levels decreases with increase in volume, our approach works best on small spatial volumes. However, thanks to the efficient worm algorithm, we have been able to extract parameters of the effective quantum mechanics up to $L = 16$ at $\beta = 0.43$ and $\beta = 0.5$. Although this lattice size is small compared to normal studies of bosonic lattice field theories, it still allows us to perform a useful study of the L dependence of the physics and draw quantitative conclusions about the thermodynamic limit. At $\beta = 0.2$ we observe that the energy levels are more densely packed and we are able to compute quantities only up to $L = 8$.

We first consider $L = 2$ and vary L_t in the range $40 \leq L_t \leq 200$ which is easy due to the small lattice size. In Fig. 5.2 we plot the behavior of our four observables as a function of the chemical potential at $L_t = 100$ and $\beta = 0.43$. Note that the particle number increases in steps of one at critical values of μ. This means energy per particle of the ground state in every particle number sector increases with the number of particles. In other words the particles repel each other. Thus, small systems containing particles of the non-linear sigma model will show the phenomena similar to *Coulomb Blockade* observed in nanoscale systems [23]. By fitting the data at $L = 2$ and $\beta = 0.43, 0.50$ and 0.20 we have extracted the parameters $\mu_c^{(N)}$, ρ_0, ρ_1 and χ_0 for $N = 0, 1, 2$ and 3. These are tabulated in Tab. 5.1. In order to show the goodness of our fits, in Fig. 5.3 we plot the behavior of $\langle N \rangle$ and χ for values of μ close to the transition between the $N = 0$ and $N = 1$ sector for different values of L_t at $\beta = 0.43$. The solid lines represent the fit functions using the parameter values given in table 5.1. Note that all the computed values of $\langle N \rangle$ shown in the left plot of

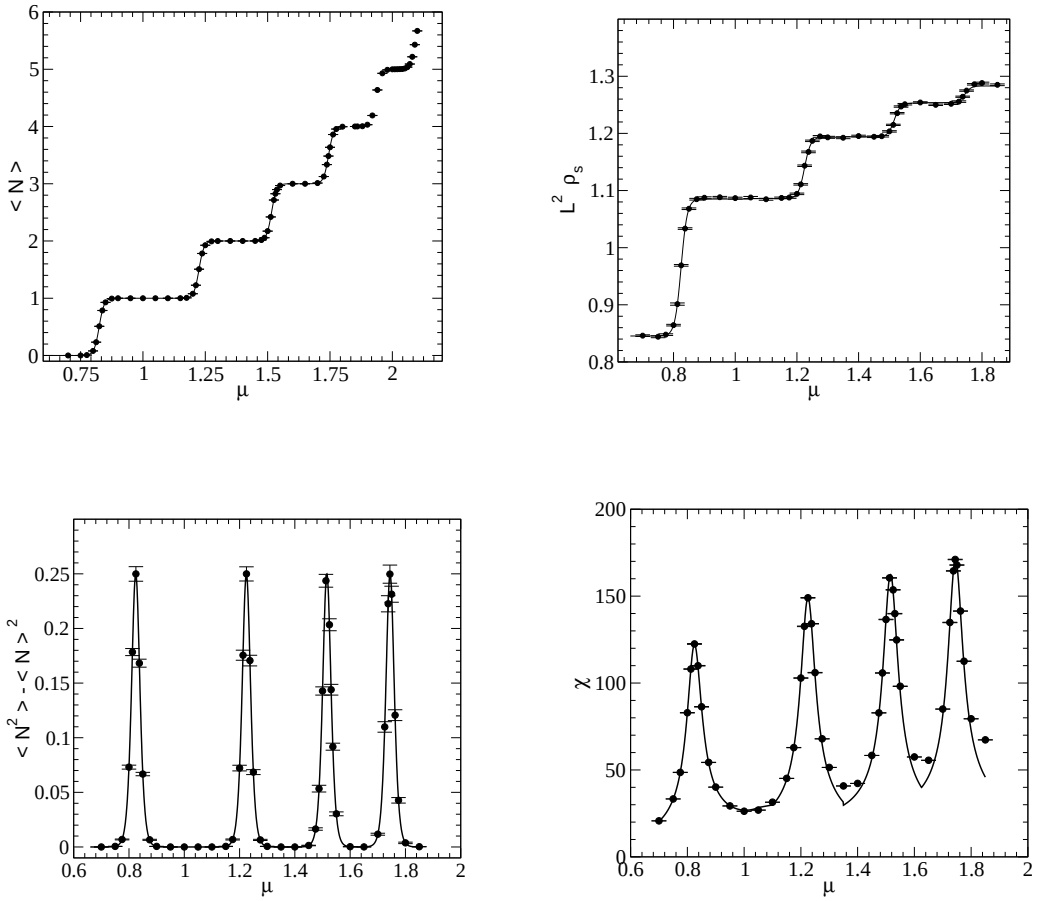

Figure 5.2: The four observables as a function of μ up to four particle excitation. The data shown is for $L = 2$, $L_t = 100$ and $\beta = 0.43$. The solid lines are fits to the effective quantum mechanical description.

Fig. 5.3 can be fit with just one parameter namely $\mu_c^{(N)}$.

We have repeated the above analysis at larger values of L. We find the physics remains qualitatively similar to the $L = 2$ case. In particular the average particle number jumps by one at critical values of μ. In Fig. 5.4 we show the average particle number as a function of μ at different values of L at $\beta = 0.43$ and $\beta = 0.50$. The effective quantum mechanics description continues to fit all our data well as long as μ is close to the critical values and L_t is sufficiently large. We plot our four observables near $\mu_c^{(0)}$ at $L = 16$ and $\beta = 0.43$ in Fig. 5.5 to support the statement. We note that as β becomes smaller, $\mu_c^{(0)}$ becomes larger while $\mu_c^{(1)} - \mu_c^{(0)}$ becomes smaller. This is the reason it becomes difficult to match the data to an effective quantum mechanics description at small β without going to very large L_t.

N	$\mu_c^{(N)}$	ρ_0	ρ_1	χ_0	χ^2/DOF			
$\beta = 0.43$								
0	0.82444(3)	0.2114(2)	0.2713(2)	2.349(4)	1.23	1.43	0.70	0.58
1	1.22462(2)	0.2715(2)	0.2983(2)	2.817(4)	0.52	0.50	1.04	0.81
2	1.51567(2)	0.298(1)	0.312(1)	3.013(4)	0.73	0.70	1.20	1.28
3	1.74436(2)	0.313(1)	0.321(1)	3.121(4)	1.02	1.02	0.78	1.14
$\beta = 0.50$								
0	0.63275(3)	0.288(1)	0.336(1)	2.63(1)	0.58	0.56	1.33	0.68
1	1.05865(2)	0.339(1)	0.362(1)	2.957(9)	0.72	0.69	0.71	1.47
2	1.35787(2)	0.364(1)	0.376(1)	3.116(8)	0.89	0.85	1.37	0.94
3	1.58951(2)	0.377(1)	0.386(1)	3.212(8)	0.57	0.54	1.07	1.00
$\beta = 0.20$								
0	1.9141(1)	0.0414(2)	0.0884(2)	1.458(9)	0.55	0.52	0.47	0.81
1	2.12263(9)	0.0884(2)	0.1106(3)	2.14(1)	0.41	0.40	1.38	0.98
2	2.33075(8)	0.1109(2)	0.1178(3)	2.40(1)	0.43	0.34	1.02	1.67
3	2.52196(8)	0.1186(3)	0.1150(2)	2.48(1)	0.56	0.52	1.36	1.17

Table 5.1: Parameters of effective quantum mechanics that describes the data for the

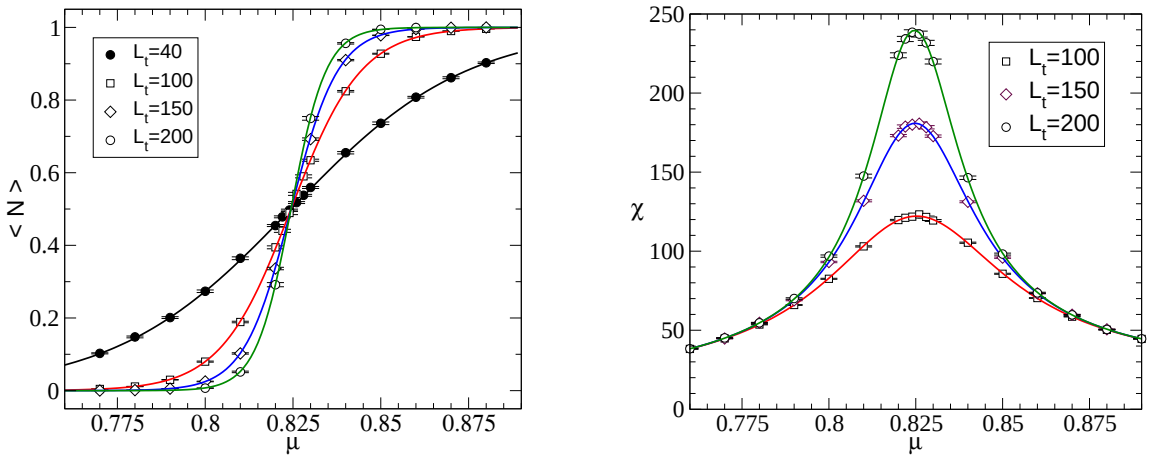

Figure 5.3: The average particle number and the condensate susceptibility as a function of μ near the transition between $N = 0$ and $N = 1$ at $L = 2$ and $\beta = 0.43$ for different values of L_t. The solid lines show the fit of data to the effective quantum mechanics description discussed in the text.

5.6 Thermodynamic Limit

Using the results of the previous section it is tempting to extrapolate to the thermodynamic limit. However, in order to accomplish this task it is important to know how the effective quantum mechanical parameters depend on L. This dependence is non-universal in general and close to a critical point will depend on the nature of the phase transition. Assuming the phase transition is second order, close to the

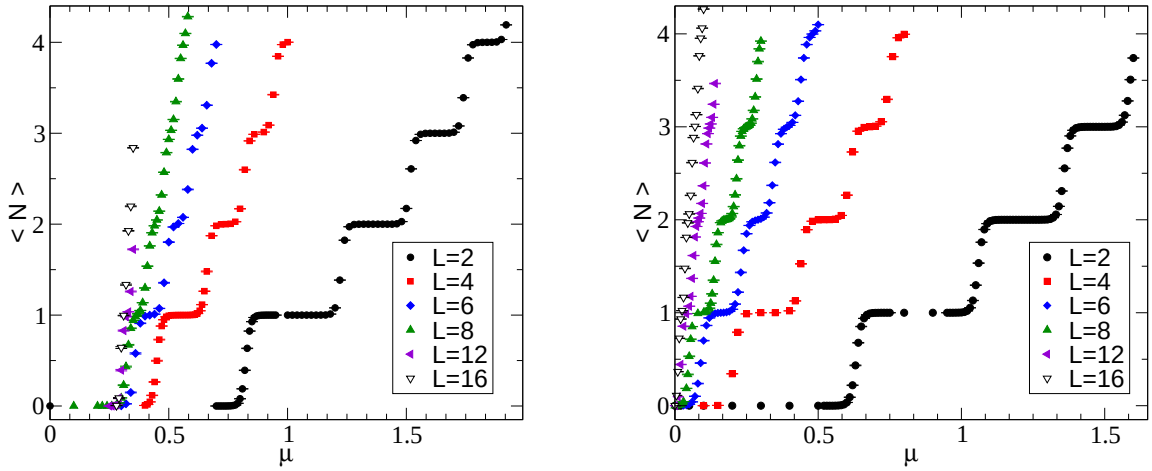

Figure 5.4: The average particle number as a function of μ for at $\beta = 0.43$ (left) $\beta = 0.50$ (right) for different values of L. When $\beta = 0.43$ the data shown is for $L_t = 100$ at $L = 2 - -8$, $L_t = 200$ at $L = 12$ and $L_t = 300$ at $L = 16$. When $\beta = 0.50$ the data shown is for $L_t = 100$ at $L = 2 - -6$, $L_t = 160$ at $L = 8$, $L_t = 200$ at $L = 12$ and $L_t = 300$ at $L = 16$.

critical chemical potential where the density can be made arbitrarily small, we expect universal features to emerge. For example, when the particles have a purely repulsive interaction, the ground state energy of N particles is always less than the corresponding energy of $N + 1$ particles [24]. Based on the results of the previous section this scenario seems to be valid in the current model. Indeed the particle number always increases by one as we increase μ at every fixed value of L. The superfluid density ρ_s also behaves like ρ. Thus, we conclude that at $\mu = \mu_c^{(0)}$ in the thermodynamic limit, there is a second order transition to a superfluid phase. Based on this, below we discuss the extrapolations to the thermodynamic limit.

First we consider $\beta = 0.43$ where the low energy physics contains massive bosons with repulsive interactions. Then, the quantity $\mu_c^{(0)}$ is simply the mass of the particle $M(L)$ at a finite L. This mass can be obtained by fitting the the temporal two-point correlation function

$$G(t) = \sum_{x_\perp, y_\perp} \left\langle \mathrm{e}^{i\theta_{x_\perp}} \mathrm{e}^{-i\theta_{y_\perp}} \right\rangle, \tag{5.22}$$

computed at $\mu = 0$, to the form $G(t) \sim \exp(-M(L)t)$ for values of $t \ll L_t/2$. In the definition of $G(t)$, $y_\perp$ and $x_\perp$ represent lattice sites at temporal slices 0 and t respectively. We have computed $M(L)$ using this method and indeed we find excellent agreement with $\mu_c^{(0)}$ at all the three values of β. This means the true mass of the particle must be

$$M = \lim_{L\to\infty} \mu_c^{(0)}. \tag{5.23}$$

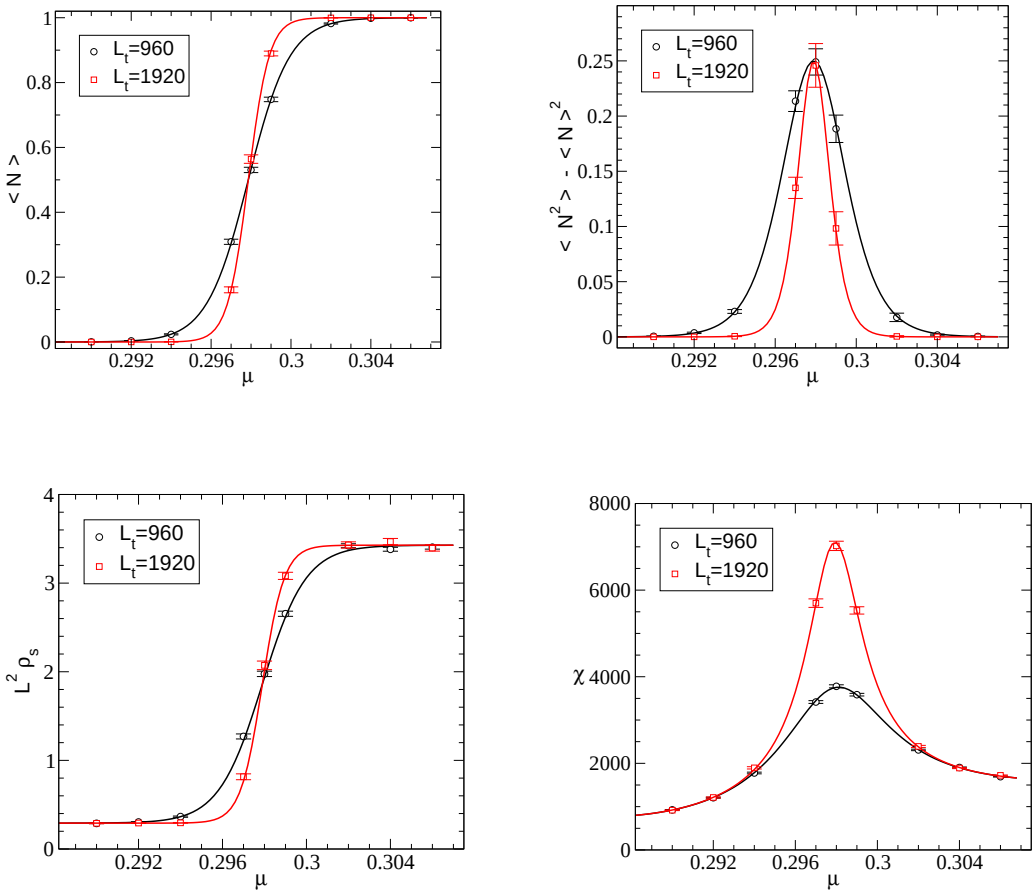

Figure 5.5: The four observables as a function of μ near the transition between $N = 0$ and $N = 1$ at $L = 16$ and $\beta = 0.43$ at two different values of L_t. The solid lines show the fit of data to the effective quantum mechanics description discussed in the text.

We can reverse this argument and obtain $\mu_c^{(0)}$ in the thermodynamic limit by simply measuring the mass of the particle at $\mu = 0$. Of course this result is not general and is valid only in the present study where there is clear evidence that the particles repel each other. In order to extract M in the massive phase ($\beta < \beta_c$) we can use Lüscher's formula [25] extended to two spatial dimensions,

$$\mu_c^0 \approx M + M_1 \mathrm{e}^{-\tilde{m}L}. \tag{5.24}$$

At $\beta = 0.43$ we find that $\mu_c^{(0)}$ fits well to this form and gives $M = 0.29680(4)$, $M_1 = 0.59(2)$ and $\tilde{m} = 0.393(4)$ with a small χ^2/DOF. The data and the fit are shown in the left plot of Fig. 5.6.

The spatial size dependence of the energy of N particles in three spatial dimensions

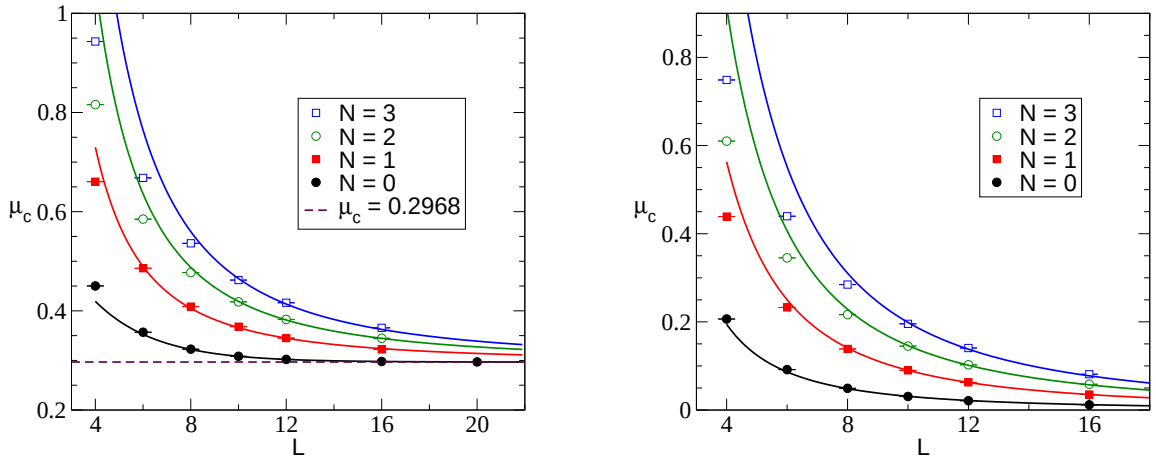

Figure 5.6: The finite size scaling of the N-particle energy levels as a function of the spatial lattice size L at $\beta = 0.43$ (left, massive phase) and $\beta = 0.50$ (right,superfluid phase).

has been calculated using models of quantum mechanics [26, 27]. Recently, this dependence was also computed using effective field theory [28]. In the special case of two particles the problem was also solved in a general massive quantum field theory in three spatial dimensions [29]. All these studies indicate that the ground state energy of N particles satisfies the relation $E_0^{(N)} - E_0^{(0)} \propto N(N+1)/L^3$. For $N \geq 1$, remember that $\mu_c^{(N)}$ is the difference in the ground state energies of $N+1$ particles and N particles. Extending the known results to two spatial dimensions and making the assumption that the particle density in the thermodynamic limit close to the critical point is of the form $\rho \sim c(\mu - \mu_c^{(0)})$ at leading order in the superfluid phase, we expect

$$\mu_c^{(N)}(L) = \mu_c^{(0)} + \frac{(N+1)}{cL^2} \tag{5.25}$$

for sufficiently large L and N. Figure 5.6 shows that our data is described reasonably well by this equation. In the left plot of Fig. 5.6 we show the values of $\mu_c^{(N)}(L)$ obtained from the fits. The solid lines show the dependence of $\mu_c^{(N)}(L)$ on L as described by eq. (5.25) with $c \approx 0.18, 0.16$ and 0.15 at $N = 1, 2$ and 3 respectively. Clearly, for large values of L the solid lines pass through the data. The value of c changes slightly since N is small. Unfortunately a fit of our data to eq. (5.25) yields a large χ^2/DOF. We believe this is due to the fact that our data has very small errors and hence is sensitive to higher order corrections which we do not know analytically at the moment in two spatial dimensions.

When $\beta = 0.5$ we are in the superfluid phase and the $U(1)$ particle number

symmetry is spontaneously broken. One then expects the low energy spectrum at finite volumes to be governed by $O(2)$ chiral perturbation theory. Based on this we again expect $\mu_c^{(N)}(L)$ to be described by eq. (5.25) but with $\mu_c^{(0)} = 0$. While our data is again consistent with these expectations (see right plot of Fig. 5.6), without keeping higher order $1/L$ corrections, the fits again give a large χ^2/DOF. The solid lines in Fig. 5.6 describe eq. (5.25) with $c = 0.33, 0.22, 0.2, 0.2$ for $N = 0, 1, 2, 3$.

5.7 Phase Diagram

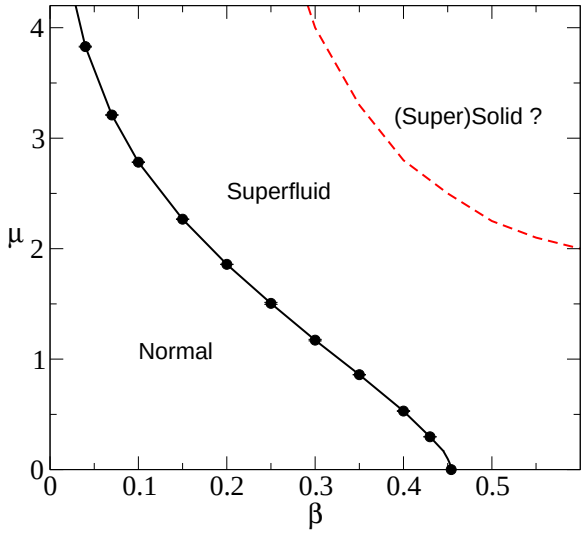

Figure 5.7: The phase diagram in the β vs. μ plane. The circles show the value of $\mu_c^{(0)}$ as a function of β given in table 5.2. The solid line that connects these points forms the phase boundary between the normal phase and the superfluid phase. This transition is second order. Since the particles repel each other we speculate that at higher densities a first order transition (dashed line) may separate the superfluid phase from a solid or a super-solid phase.

The phase diagram of the $O(2)$ non-linear sigma model is an interesting research topic in itself. While the complete phase diagram requires more work, our results above allow us to compute the location of the transition line between the normal phase and the superfluid phase. In particular the value of $\mu_c^{(0)}$ as a function of β determines this line. Based on the evidence at $\beta = 0.43$ and 0.20 we predict that $\mu_c^{(0)} = M$ for all values of $\beta < \beta_c$. The coordinates of the transition line are tabulated in Tab. 5.2 and shown on the phase diagram in Fig. 5.7. We expect this transition to be second order in the mean field universality class with logarithmic corrections

except at $\mu = 0$ where it is governed by the $3d$ XY universality class. Thus, when $\beta < \beta_c$ and $(\beta_c - \beta)/\beta_c \ll 1$ we must have $\mu_c^0 \propto [(\beta_c - \beta)/\beta_c]^\nu$ where $\nu \approx 0.671$ [30].

β	0.43	0.40	0.35	0.30	0.25	0.2	0.15	0.10	0.07	0.04
$\mu_c^{(0)}$	0.29678(3)	0.530(4)	0.859(2)	1.172(7)	1.505(9)	1.85801(3)	2.267(3)	2.783(3)	3.210(3)	3.829(4)

Table 5.2: The values of $\mu_c^{(0)}$ obtained by assuming that it is equal to the $L \to \infty$ limit of $M(L)$ at $\mu = 0$ as discussed in the text.

In principle there could be other interesting phases at larger values of μ which we cannot rule out based on the current work. Since we have seen the particles have a repulsive interaction, an interesting possibility is the existence of a solid phase or a super-solid phase [31]. However, there are stringent constraints for super-solids to arise [32, 33] and we do not know if these rule out such a phase in the current model. In any case if a transition to a solid phase exists, it will most likely be first order similar to the solid-liquid phase transitions in materials and will occur at densities where the lattice structure may become important. These transitions can also be studied efficiently with the worm algorithm. We postpone these studies for the future, but have speculated the possibility of a solid phase in Fig. 5.7.

5.8 Summary and Discussion

In this chapter, we have explored the $O(2)$ non-linear sigma model in the presence of a chemical potential and showed that interesting finite size effects naturally arise due to the level crossing phenomena. Understanding these effects was shown to be important to extract the thermodynamic limit and thus uncover the (β, μ) phase diagram. Our studies should be useful for future studies since the finite size effects we uncover is a universal feature. In fact, a very similar structure in the number density of quarks was obtained in 2-colour QCD at very low temperatures and for finite quark chemical potential [34]. Since 2-colour QCD does not have a sign problem it can be readily simulated using the standard methods.

Our work also provides accurate results that can be used to compare with results from other methods that try to address the sign problem. The most encouraging of these methods is commonly known in literature as the complex Langevin method. This method [35, 36], based on the techniques of stochastic quantization [37] does not require importance sampling. The configurations that dominantly contribute to the partition function are obtained by integrating complex Langevin equation. This method is being explored as a general solution to the sign problem. However this method often suffers from instabilities and convergence problems. While the

instabilities can be corrected [38], it might converge to the wrong result as has been demonstrated for the XY model at finite μ [39].

References

[1] A. Bazavov et al *Phys. Rev.* D 80 014504,2009

[2] C. DeTar and U. M. Heller *Eur. Phys. J.* A41, 405(2009)

[3] T. Hatsuda and K. Maeda in *Developments in Quantum Phase Transitions* ed. L. D. Carr (Taylor and Francis, 2010); arXiv: 0912:1437

[4] M. G. Alford et. al *Rev. Mod. Phys.* 80, 1455 (2008)

[5] L. McLerran and R. D. Pisarski *Nucl. Phys.* A 796, 83 (2007)

[6] U. Wolff *Nucl. Phys.* B 322, 759 (1989)

[7] M. G. Endres *Phys. Rev.* D75, 065012 (2007)

[8] S. Chandrasekharan **PoS LATTICE** 2008, 003 (2008)

[9] N. Prokofév and B. Svistunov *Phys. Rev. Lett.* 87, 160601 (2001)

[10] O. F. Syljuasen and A. W. Sandvik *Phys. Rev.* E 66, 046701 (2002)

[11] D. H. Adams and S. Chandrasekharan *Nucl. Phys.* B 662, 220 (2003)

[12] F. Karsch and K. H. Mutter *Nucl. Phys.* B 313, 541 (1989)

[13] S. Chandrasekharan and F.-J. Jiang *Phys. Rev.* D 74, 014506 (2006)

[14] S. Chandrasekharan and A. Mehta *Phys. Rev. Lett.*, 99, 142004 (2007)

[15] P. de Forcrand and M. Fromm *Phys. Rev. Lett.* 104, 112005 (2010)

[16] U. Wolff *Nucl. Phys.* B 810, 491 (2009)

[17] U. Wenger *Phys. Rev.* D 80, 071503 (2009)

[18] U. Wolff *Nucl. Phys.* B814, 549 (2009)

[19] U. Wolff *Nucl. Phys.* B824, 254 (2010); B843, 395(E) (2010)

[20] V. Azcoiti et. al. *JHEP* 08 (2009) 008

[21] P. Hasenfratz and F. Karsch *Phys. Lett.* B 125, 308 (1983)

[22] D. M. Ceperley and E. L. Pollock *Phys. Rev.* B 39, 2084 (1989)

[23] F. H. Julien and A. Alexandrou *Science* 282, 1429 (1998)

[24] K. Sawada *Phys. Rev.* 116, 1344 (1959)

[25] M. Luscher *Commun. Math. Phys.* 104, 177 (1986)

[26] N. N. Bogolyubov *J. Phys. USSR* 11,23 (1947)

[27] K. Huang and C. N. Yang *Phys. Rev.* 105, 767 (1957)

[28] S. R. Beane, W. Detmold and M. J. Savage *Phys. Rev.* D 76, 074507 (2007)

[29] M. Luscher *Commun. Math. Phys.* 105, 153 (1986)

[30] M. Campostrini et. al. *Phys. Rev.* B 63, 214503 (2001)

[31] E. Kim and M. H. W. Chan *Nature* (London) 427, 225 (2004)

[32] A. J. Leggett *Phys. Rev. Lett.* 25, 1543 (1970)

[33] N. Prokofév and B. Svistunov *Phys. Rev. Lett.* 94, 155302 (2005)

[34] S. Hands, T. Hollowood, J. C. Myers *JHEP* 1012:057,2010

[35] G. Aarts *Phys. Rev. Lett.* 102:131601,2009; **PoS LAT** 2009:024, 2009

[36] G. Aarts and I. O. Stamatescu **PoS LATTICE** 2008:176,2008

[37] G. Parisi and Y. S. Wu *Sci. Sin.* 24 (1981) 483

[38] G. Aarts, F. James and E. Seiler *Phys. Lett.* B687 (2010) 154-159

[39] G. Aarts and F. James *JHEP* 1008 (2010) 020

Chapter 6

Conclusion and Summary

Recent experimental results from RHIC indicate the formation of a thermalized medium with large collective flow and very low viscosity. These findings are indicative of the strongly interacting nature of the QGP at temperatures close to the quark-hadron transition temperature. At these temperatures, the QCD coupling is rather large, and perturbative studies are not suitable for studying the strongly coupled QGP, and non-perturbative studies are called for. At present, lattice QCD is the only viable and successful non-perturbative technique for studying such a system. Moreover, numerical simulations of LQCD have the advantage that almost parameter free predictions for the theory can be obtained from first principles. This approach has been very successful in obtaining detailed information about the nature, composition and thermodynamics of QCD. In this thesis, we have used Monte-Carlo techniques to obtain non-perturbative information about strongly interacting matter at finite temperature and density.

Spatial correlation functions are used to study the screening of a static charge by the medium. The long distance behaviour of these correlation functions give information about the large scale composition of the medium. The structure of the correlation functions related by symmetry transformations indicate the breaking or the restoration the corresponding symmetry of the medium as the temperature is varied. In this thesis, I have used the screening correlators of various mesons to study the pattern of chiral symmetry restoration in 2-flavour QCD as the temperature is raised across the quark-hadron transition. The zero temperature pion mass was kept fixed at $m_\pi \sim 230$ MeV, while the lattice spacing was $a = 1/6T$ and the temperature was varied from 0.89 T_c in the hadronic phase to 1.92 T_c in the plasma phase.

Our results demonstrate that the screening masses, obtained as the inverse of the correlation lengths in the various quantum number channels become identical by T_c in the Vector (V) and the Axial-Vector (AV) channels. In the Pseudo-Scalar and the

Scalar channels such a symmetry restoration is seen only at temperatures of around 1.33 T_c. The late restoration of chiral symmetry in the PS/S channels was further investigated by changing the valence quark mass. The correlation functions and the screening masses are sensitive to this change in the PS/S channel, whereas the V/AV channel remain unaffected. Moreover the V and the AV screening masses become consistent with the free-field value at temperatures above T_c. In contrast, we find that even at the highest temperatures of our study, at $\sim 2\ T_c$, the S and the PS screening masses are about $\sim 20\%$ away from their free field values. An investigation of the finite volume effects in the hadronic phase shows the stability of the mesonic states.

Using linear response theory to relate quantities calculated using lattice QCD, certain transport coefficients can be computed and compared against experimental estimates. One such quantity is the thermalization of heavy quarks, which have been recently inferred for the charm quark by the PHENIX experiment at RHIC. The prevailing puzzle regarding the results is that both the heavy and the light quarks appear to thermalize at similar rates. This is quite in contrast to the wisdom from perturbation theory which states that the thermalization time of heavy quarks should be suppressed by a factor $\sim T/M$ with respect to that of light quarks, where T is the temperature of the medium and M is the mass of the heavy quark. For charm quarks at RHIC experiment, this factor is about 4.5. The strongly interacting nature of the plasma might be responsible for this disagreement. This thesis investigates a formulation of the problem where the heavy quark is treated as a Brownian particle undergoing random walk because of being constantly subjected to collisions by the quasi-particles of the plasma. It has been shown that the diffusion coefficient can be obtained from the long distance behaviour of the chromo-electric-field correlation functions in Euclidean time. We have calculated these correlation functions non-perturbatively for the quenched theory for infinitely massive quarks. We have used the multilevel algorithm to obtain an estimation of the correlation function to within errors of a few percent. With our parameterization the large-τ part of the correlation functions, we conclude that lattices of at least $a \sim 1/20T$ are needed to identify the diffusive part. An estimation of the diffusion constant from our largest lattices ($N_t = 20, 24$) is roughly in the right ballpark of the values inferred from the experimental results at RHIC for charm quarks.

An important issue in the study of finite temperature symmetry restoration is the use of fermions with the right flavour symmetry group as in continuum QCD. The latter is believed to exhibit the restoration of $SU(2) \times SU(2)$ flavour symmetry in the limit of vanishing quark mass. The staggered quarks dominantly used in these

studies only have $U(1) \times U(1)$ chiral symmetry. Moreover the search for the critical end point (CEP) in real world QCD with two light quarks and one moderately heavy quark crucially depends on the use of fermions having the correct flavour symmetry in the action. These reasons favour the use of fermions with exact chiral symmetry on the lattice, such as the overlap fermions. However, the use of overlap fermions in numerical simulations is very expensive due to their non-local nature. In this thesis, we have analytically studied the thermodynamics of free overlap quarks at finite quark chemical potential.

Typically the chemical potential is introduced as the Lagrange multiplier of some conserved charge. This is non-trivial for the case of the overlap fermions due to it's non-locality. Instead, an inspired guess was used to motivate the inclusion of the chemical potential in the overlap operator. This form has the correct continuum limit. We studied this approach analytically and showed that this does indeed yield the correct continuum form of the expressions for the thermodynamic quantities provided certain conditions are imposed on the functions which encode the dependence of the chemical potential in the overlap operator. These conditions are identical to those worked out more than two decades back for the local Wilson and Staggered fermions to avoid spurious μ dependent divergences in the continuum limit in the expressions for thermodynamic quantities. For the overlap fermions, these conditions serve the same purpose and are essential for recovering the proper Fermi surface on the lattice. This indicates that it is the behaviour of the Dirac operator in the continuum limit that governs these conditions.

A major hindrance in the numerical computation of physical quantities from first principles at finite chemical potential is the sign problem. At finite values of the quark chemical potential, the fermion determinant which is a part of the Boltzmann weight for doing Monte-Carlo integration, becomes complex. The Monte-Carlo calculations can then no longer be performed and the theory is said to have a sign problem. Several methods are in use to circumvent the sign problem in QCD. One approach to solve this problem aims at reformulating the theory having a sign problem in terms of other degrees of freedom. If the new degrees of freedom are cleverly chosen, the sign problem can be eliminated in the reformulated theory. However, since this choice is highly non-trivial, this method is rather restrictive. This procedure is demonstrated here for the non-linear O(2)-sigma model, commonly known as the XY model in the literature.

The XY model has a similar sign problem as that of QCD when finite quark chemical potential is included. Employing the global U(1) symmetry of the model, the action can be formulated in terms of the corresponding Noether currents. In

terms of these current variables, the action is explicitly positive definite and the sign problem is successfully eliminated.

The reformulated model can be efficiently simulated using the Worm algorithm. In this thesis, we have investigated the phase diagram for the model at finite μ and at low temperatures. Our studies reveal the existence of non-trivial finite size effects in the number density and susceptibility as a function of μ. We have been able to account for these effects by taking into account the phenomenon of level-crossing of the low-lying eigenvalues as the chemical potential is tuned. Our results give evidence of a repulsive interaction between the particles. Accounting for these finite size effects was essential to obtain the phase boundary between the symmetric and the broken phase.

Appendix A

Algorithmic details for the XY model

A.1 The worm algorithm

The worm algorithm for the partition function described by eq. 5.4 can easily be constructed using ideas from [1, 2, 3]. Here we outline the essential steps of the update for completeness. Each worm update is as follows

1. We pick a random point x on the lattice. We will also call this site x_{first}. We set a counter $c = 0$.

2. We pick at random one of $2d$ neighbors $x + \hat{\alpha}, \alpha = \pm 1, \pm 2, ..., \pm d$ of the site x.

3. Let k be the current on the bond connecting x and $x + \alpha$. If α is positive then with probability
$$\frac{I_{k+1}(\beta)\mathrm{e}^{\mu\delta_{\alpha,t}}}{I_k(\beta)}$$
we change k to $k + 1$ and move to the neighboring site $x + \hat{\alpha}$. If α is negative then with probability
$$\frac{I_{k-1}(\beta)\mathrm{e}^{-\mu\delta_{\alpha,t}}}{I_k(\beta)}$$
we change k to $k - 1$ and move to the neighboring site $x + \hat{\alpha}$. Otherwise we stay at site x.

4. We set $c = c+1$. If $x = x_{\text{first}}$ we stop and complete one worm update. Otherwise we go to step 2 and repeat the above steps.

It turns out that χ is given by the average of c after many worm updates. The other observables are measured on each world-line configuration and averaged over

β	χ	χ^{MC}	ρ	ρ^{MC}	κ	κ^{MC}	ρ_s	ρ_s^{MC}
$\mu = 0.0$								
0.1	1.2207	1.2206(1)	0	$2(2) \times 10^{-5}$	0.01005	0.01001(4)	0.01005	0.01008(4)
0.2	1.4831	1.4830(2)	0	$-5(4) \times 10^{-5}$	0.04064	0.04063(8)	0.04064	0.04076(8)
0.5	2.3838	2.3835(4)	0	$1(9) \times 10^{-5}$	0.2526	0.2527(2)	0.2526	0.2526(2)
1.0	3.2730	3.2733(4)	0	$2(2) \times 10^{-4}$	0.7796	0.7796(4)	0.7796	0.7794(4)
5.0	3.8728	3.8733(3)	0	$1(1) \times 10^{-3}$	4.809	4.806(4)	4.809	4.813(4)
$\mu = 0.5$								
0.1	1.2362	1.2361(1)	0.00590	0.00592(2)	0.01559	0.01560(5)	0.01007	0.01013(4)
0.2	1.5188	1.5188(2)	0.02374	0.02378(5)	0.0640	0.0640(1)	0.04100	0.04105(7)
0.5	2.4692	2.4693(4)	0.1429	0.1430(1)	0.4341	0.4344(3)	0.2581	0.2581(2)
1.0	3.3245	3.3247(4)	0.4190	0.4193(2)	1.6553	1.6564(10)	0.7867	0.7861(4)
$\mu = 1.0$								
0.1	1.2861	1.2861(2)	0.01809	0.01812(4)	0.03851	0.03857(8)	0.01018	0.01024(4)
0.2	1.6316	1.6317(2)	0.07160	0.07162(8)	0.1637	0.1638(2)	0.04241	0.04242(8)
0.5	2.6899	2.6900(4)	0.3865	0.3868(2)	1.2530	1.2539(8)	0.2747	0.2748(2)
1.0	3.4317	3.4317(4)	1.0053	1.0055(3)	5.487	5.488(3)	0.8032	0.8033(4)

Table A.1: Checks of the observables with exact solution on 2×2 lattices.

the ensemble generated by the worm algorithm.

A.2 Tests of the Algorithm

We have verified our algorithm and code by both solving the model exactly on a 2×2 lattice as well as comparing with the available results in the literature for $\mu = 0$ in three dimensions. In this section we describe some of these tests. First, we compare the results of the various observables computed using the directed path algorithm with the exact results on a 2×2 lattice. The comparison is shown in Table A.1. Since space and time are symmetric we expect $\rho_s = \kappa$ at $\mu = 0$. Our results reflect this fact.

Extending the code from two dimensions to three dimensions is trivial and the chance for mistakes is rather small. However, we have tested the code at least at $\mu = 0$ using the results from previous work. Here we compare results for χ obtained using the worm algorithm with that obtained using the microcanonical improved Metropolis (MM) algorithm and the available results in the literature using the cluster method [4]. The comparison is shown in Table A.2. The reason for us to choose $\beta = 0.45421$ is because this is known to be the critical value of the coupling where the theory undergoes a phase transition from a normal phase to a superfluid phase. At the critical coupling we expect $\chi \propto L^{\gamma/\nu}$. A fit of our data to this form yields the value of $\gamma/\nu = 1.99$ as expected from [4], and is shown in figure A.1.

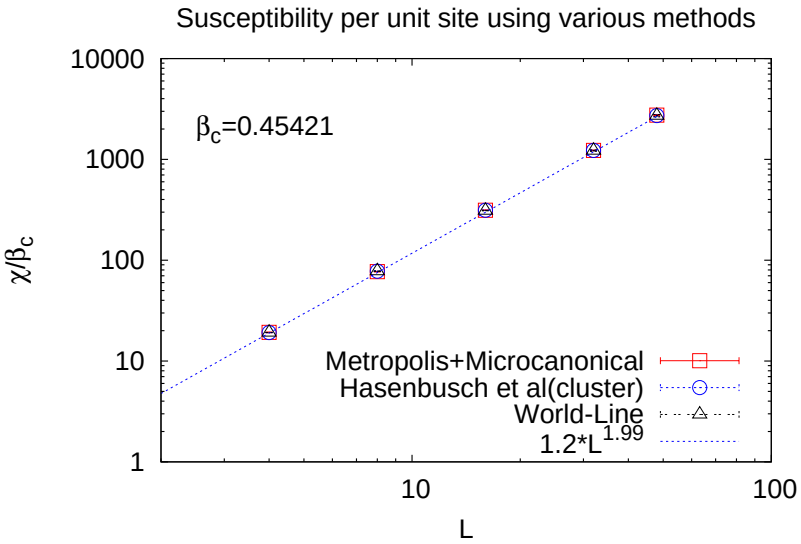

Figure A.1: Plot of χ vs L at $\beta = \beta_c$.

β	L	Worm	MM	Cluster
0.45421	4	19.17(3)	19.24(13)	19.15(5)
0.45421	8	77.8(2)	76.9(5)	77.9(3)
0.45421	16	310(1)	313(2)	313(2)
0.45421	32	1221(18)	1228(7)	1226(13)
0.45421	48	2713(67)	2750(27)	2719(68)
0.01	8	1.0304(2)	1.03(46)	-
0.1	8	1.3976(9)	1.40(6)	-
1.0	8	387.2(3)	387.12(3)	-

Table A.2: Comparison of the condensate susceptibility χ with results from the worm algorithm, the Metropolis+Microcanonical(MM) update and Wolff Cluster update on L^3 lattices at different values of L and β.

References

[1] N. Prokofév and B. Svistunov Phys. Rev. Lett. 87, 160601 (2001)

[2] S. Chandrasekharan and F.-J. Jiang Phys. Rev. D 74, 014506 (2006)

[3] U. Wolff Nucl. Phys. B824, 254 (2010); B843, 395(E) (2010)

[4] M. Hasenbusch and S. Meyer Phys. Lett. B 241, 238 (1990)